Aspects of Ship Design; Optimization of Aft Hull with Inverse Geometry Design

Vidar Tregde

Dr.ing.-thesis 2003:107

Faculty of Engineering Science and Technology
Department of Marine Technology

Abstract

The main contribution of this thesis is on the study of optimization methods in aft hull design. The optimization methods are inverse geometry design methods to find an aft hull with the flow velocities we specify. The analytic foundation for the flow is given by Stratford in [31], and gives a prescibed velocity distribution on the aft body. With the parameter β we have adjusted this flow to have a certain margin to separation along the pressure recovery region.

This principle and optimization method are successfully applied to design of ships with pram-type aft hull. The 2D optimized profiles corresponds to centerline buttock, and 3D hull sections are extended from this centerline buttock with a bilge radius.

Stratfords original pressure distribution for pressure recovery region were meant for Reynolds numbers up to 10^7. We have extended Stratfords formula to yield for ship full scale Reynolds numbers of 10^9.

Different optimization methods were programmed and tested. The best routine for our optimization of aft hull with Stratford flow, was when the offset y-value were the optimization parameter to be changed. When we tried to optimize a complete 2D profile with a given pressure distribution, it worked best to use the variables in a B-spline as the optimization parameter.

Extensive windtunnel tests and towing tank tests are carried out. The tests verified the hydrodynamic properties of the hulls.

Towing tests indicates that the optimized hull lines have lower total resistance than conventional ships with the same main dimensions. Both the frictional, viscous pressure resistance and wave making resistance are significantly lower. Further we can increase cargo capacity with the same power consumption, and achieve a more favourable distribution of the displacement in the aft hull.

This study has shown us that the slant angle for the bottom of the aft hull should not exceed 15° with horizontal plane due to danger of separation over the bilge, and longitudinal vortices forming.

II

Acknowledgements

This study has been carried out by supervision from Professor Odd M. Faltinsen, Professor Knut J. Minsaas and Dr.Ing Sverre Steen. Their guidance and support has been a great encouragement.

I also wish to express my sincere gratitude to Umoe Mandal, and especially Dr.Ing Nere Skomedal and Anders Hjelmseth, for their patience and support in all ways during the study.

The staff in the towing tank at Marintek were allways there to help during the manufacturing of the models and towing tests. Their help and sense of humour were deeply appreciated.

I profoundly thank Professor Per Å. Krogstad and the staff at the wind tunnel (Institutt for mekanikk, termo- og fluiddynamikk) for their hospitality and valuable support during the wind tunnel tests.

In February 2000 I visited PhD C.W.B Grigson at Agder Ingeniør- og Distriktshøgskole in Grimstad. I am deeply thankful for his creative contributions to my thesis.

A deep gratitude is expressed to colleagues and friends at the Department of marine hydrodynamics for all the help and advice they have extended over the last years.

Last but not least, a deep thank to Mussie Debesai and Andreas Lier in Trondheim for their warm friendship and great encouragement when the going got tough.

This work has received financial support by the Research Council of Norway (NFR), and it has been a part of SKIPRO, a research project run by Marintek.

IV

Contents

Nomenclature

Symbols

Most of the symbols used in this thesis are defined below. Some symbols that only have a local meaning are only defined close to where they are used. The symbols are mainly based on ITTC.

B	Breadth, moulded
C_{AA}	$= D_{AA}/(\frac{1}{2}\rho U_\infty^2)$ Air resistance coefficient
C_B	Block coefficient, ship
C_{BD}	$= D_B/(\frac{1}{2}\rho U_\infty^2)$ Transom stern resistance coefficient
C_{Dp}	$= D_p/(\frac{1}{2}\rho U_\infty^2)$ Viscous pressure resistance coefficient
C_F	$= D_F/(\frac{1}{2}\rho U_\infty^2 S)$ Total skin friction coefficient
C_f	$= \tau_w/(\frac{1}{2}\rho U_\infty^2)$ Local skin friction coefficient
C_p	$= (p_S - p_0)/(\frac{1}{2}\rho U_\infty^2)$ Pressure coefficient
C_V	$= D_V/(\frac{1}{2}\rho U_\infty^2 S)$ Viscous resistance coefficient
C_W	$= D_W/(\frac{1}{2}\rho U_\infty^2 S)$ Wave making resistance coefficient
D_B	Transom stern resistance
D_F	Total skin friction resistance
D_p	Pressure resistance
D_T	Total resistance
D_V	Viscous resistance
D_W	Wave making resistance
Fn	$= U/\sqrt{g\,L_{pp}}$ Froude number

g	Acceleration due to gravity
k	Form factor
L	Length scale
L_{wl}	Length measured along waterline
L_{pp}	Length measured between perpendiculars
p_0	Reference static pressure
p_S	Static pressure
Rn	$= U_\infty L/\nu$ Reynolds number
Rn_{δ_2}	$= U_\infty \delta_2/\nu$ Reynolds number based on momentum thickness
S	Surface area
s	Distance along body surface
s_0	Equivalent flat plate length
T	Draft
$\overline{U}$	Mean velocity
U_0	Peak velocity in Stratford flow
U_e	Local freestream velocity at the edge of BL
U, U_s	Local freestream velocity, potential flow
U_∞	Freestream velocity immediately upstream of body
u	Velocity in the boundary layer at a distance y from the surface
u^+	$= u/v^*$ Dimensionless BL velocity
$\sqrt{\overline{u'^2}}/\overline{U}$	Turbulence intensity
v^*	$= \sqrt{\tau_w/\rho}$ Shear (or friction) velocity
x, y, z	Distance along respectively x-, y- and z-axis.
y^+	$= yv^*/\nu$ Dimensionless wall distance
β	Optimization parameter in Stratford flow
β_n	Angle with horizontal for vector along element nr n
$\gamma(s)$	Vortex at position s on body surface
δ	99-percent thickness of boundary layer
δ_1	Displacement thickness

δ_2	Momentum thickness
ν	Kinematic viscosity
ρ	Mass density
σ	Error of a varible
τ_w	Wall shear stress

Abbreviations

2D, 3D	Two- and three-dimensional
AP	Aft perpendicular
AVD	Actual velocity distribution
CL	Centerline
BL	Boundary layer
FEM	Finite element method
FP	Forward perpendicular
Lo-Lo	Lift on lift off vessel
PVD	Prescribed velocity distribution
Ro-Pax	Roll on passenger vessel
Ro-Ro	Roll on roll off vessel
SAC	Sectional area curve

Chapter 1

Introduction

1.1 Background and motivation

In the last years there have been a growing demand for fast-going Ro-Ro (Roll on Roll off) vessels. These ships are designed so that cars, trucks, train etc can drive on and off the ships via ramps. The loading and unloading is effective as opposed to traditional Lo-Lo (Lift on Lift off) where the cargo is being loaded by cranes. The obvious advantage is that the cargo can be transported on board as it comes to the harbour, without being reloaded. The drawback is that the weight per volume of the cargo on a Ro-Ro ship is relatively low.

The Ro-Ro ships have large decks, and are fitted with doors in the bow and stern, or only a door at the stern. These ships normally have a wide transom stern.

Ro-Ro vessels may be carrying only trucks/cars or a combination of trucks, cars and passengers, sometimes called Ro-Pax. The Ro-Ro and Ro-Pax ships range from a few hundred tons up to 50-60000 gross tons. The world's fleet is now about 1200 vessels, and the fleet is growing steadily.

The average speed of Ro-Ro vessels has increased through the years for the largest vessels, up to 30 knots. This means the Froude number for the largest vessels has increased, thanks to more efficient hull lines, propellers, engines etc. For the smaller vessels the speed has been more or less the same. Typical service speed for most of the vessels are 18-22 knots.

The speed requirements for the largest vessels are often up to Fn=0.35. The traditional cruiser stern is not an effective stern design of such high speed

vessels, and therefore these vessels normally have a pram-type aft body. This type of aft body introduces difficulties in ship design, but also advantages. It is often easier and cheaper to build than the traditional cruiser stern. Another and as important factor is that the pram-type often gives more useful volume onboard. In [11] Hämäläinen et al has done considerable work on the design of pram-type ships, and find that this aft body has relatively low power curve, good manoeuvring ability and the "wave damping aftbody" of the pram-type was effective in reducing wavemaking resistance.

The number of ships propelled by azimuthing pods are increasing. A pram-type hull is a good platform for azipod propulsion, and with this type of propulsion we are more free in the design of the hull lines.

One of the first things to do in the design spiral of a new ship is to determine the optimum main dimensions of the ship. After this we can fine tune the hull form to have acceptable hydrodynamic performance. At this stage CFD tools have proved to be of great help, and their applicability is improving very fast. A further step at this stage of the design of hull forms is the use of optimization methods linked to CFD tools . They have still not proved to be a practical tool in ship design, but as research increases and the optimization tools are improved, it probably will be a practical tool in some areas of ship design in the future.

Most of the optimization methods to this date either optimizes a ships bow due to wavemaking resistance or a ships stern with respect to viscous resistance. In [5] Cheng-Hung Huang et al optimizes the shape of a ships bow with the aid of an inverse design method coupled to a non-viscous free surface procedure. Tahara et al optimize the stern of a ship in [32] with respect to minimization of delivered power to propeller. They use a CFD-based optimization method with a Reynolds-averaged Navier-Stokes equation solver. In [7] Nagamatsu et. al. minimize viscous resistance of 2D bodies and 3D full forms under certain design constraints. These methods will be dealt with further in chapter 3.

Optimization methods are well suited to be used in detail design of Ro-Ro vessels, because of the pram-type aft body they often have. In a simple way, we can say that this type of aft body is a slanted flat surface ranging from the aft shoulder at the bottom of the ship to the transom stern. A bilge radius is fitted between the ship side and the slanted surface. Fig. 1.1 shows a ship of this kind. A skeg would be fitted at the centerline for longitudinal stability.

In this thesis we have focused on inverse geometry design of the slanted surface on this kind of hulls, and how this influences the vessels hydrodynamic performance.

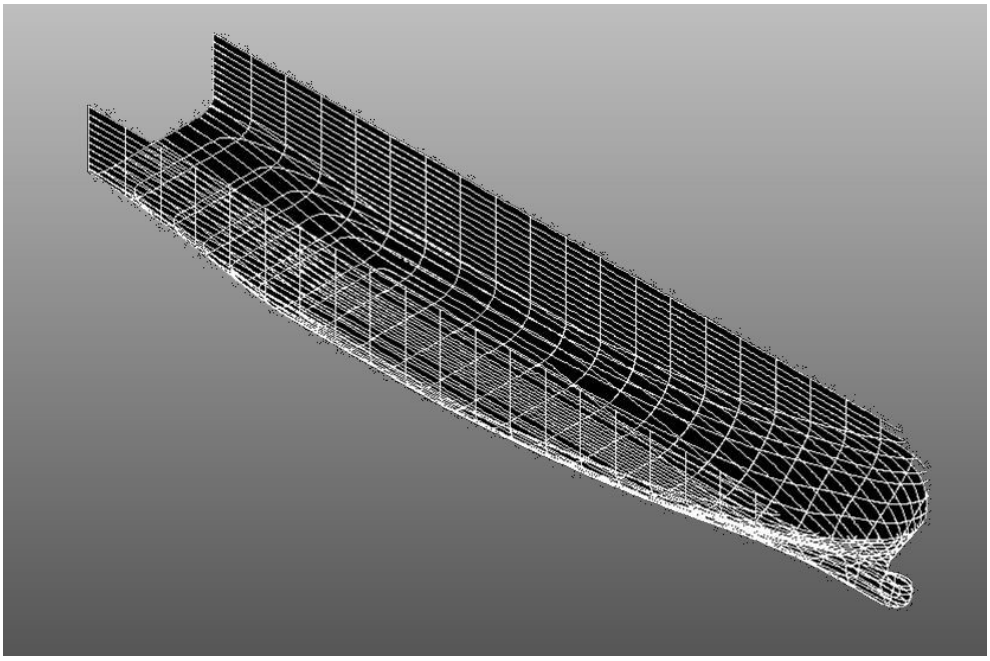

Figure 1.1: *A hull designed with the inverse geometry design routine.*

1.2 Contributions of the thesis

The main contribution of this thesis is on the design and analysis of optimization methods in aft hull design of for instance a Ro-Ro vessel. The optimization methods are inverse geometry design methods to find an aft hull with the flow velocities we specify. The specified flow velocities is given so that the flow has a certain margin for separation all along the pressure recovery on the aft hull. This margin for separation can be varied with a parameter or by changing the design Reynolds number.

An optimization procedure based on inverse geometry design has been made, and hull forms have been designed with this procedure. Models of the hulls have been tested in wind tunnel and towing tank to verify the flow over the aft hull, and the overall performance of the designed hulls.

The optimization procedure is 2D, and the hull form is made by using the inverse designed 2D profile as a keel line for the aft hull, and extending the section with fitted bilge radius to form a pram-type hull form, see fig. 1.1. A skeg is added at the centerline.

The 2D design optimization method uses a socalled Stratford flow principle. In [30] and [31] Stratford presents a method to calculate the separation point for 2D bodies. He then extends the method and gives an analytic formula for a pressure distribution which will have almost separation all along the aft part of the body. A boundary layer flow which is almost separating, means that we have small flow velocity close to the wall. By modifying a parameter in the formula, we can have a flow over the pressure recovery on the aft body with a certain margin for separation.

In this thesis the largest effort has been to find an effective optimization method which can be used for inverse design with the Stratford formula as input pressure distribution. Several methods were tested, and finally we found a method that worked. Two hulls were designed, one with relatively short run from aft shoulder to transom stern, and one with slightly longer run. Both models were tested in a wind tunnel, and static pressure distribution and boundary layer velocity were measured to verify the longitudinal velocity distribution and the local skin friction. One of the hulls were selected for towing tank tests. In the towing tank we measured static pressure distribution, resistance and sinkage. The ship model were not tested in waves, only flat water.

The main contributions of the thesis are found in the following chapters.

Chapter 2.2 contains a derivation of Stratfords formula from $Rn \approx 10^7$ to $Rn \approx 10^9$ with the aid of the boundary layer power formula linked to the boundary layer logarithmic law.

Chapter 3.3 contains the inverse design method which is developed for inverse geometry design of pram-type hull forms. The direct flow calculations are done with a vortex distribution on the body surface, and this direct flow code is linked to an optimization procedure.

Chapters 3.4 - 3.5 contain inverse designed 2D profiles with Stratford velocity distribution. The design procedure from 2D profiles to 3D hulls are described.

Chapters 4.1.3 - 4.1.6 contain experimental results from the wind tunnel of the hull forms designed. We measured static pressure on the hull surface and boundary layer velocity on different locations on the hulls. At the end we measured wake velocity in the propeller plane.

Chapters 4.2.2 - 4.2.3 contain towing tank results of one of the models. We measured wave resistance, trim and sinkage to verify the calm water behaviour of the vessel. We also measured static pressure on the ship hull to compare with the wind tunnel tests.

Chapter 5.1 presents the hull forms which were developed by the inverse design method in a commercial ship development project.

Chapter 2

Theory

This chapter deals with the theoretical foundation for the rest of the thesis. In section 2.1 we have a short treatment of ship model experiments and its scaling from model to full scale. The experiments will be dealt with in chapter 4.

In section 2.2.1 the flow over a flat plate is briefly discussed, comparing logarithmic and power law description of boundary layer velocity profiles. This is done because the Stratford flow velocity distribution which is outlined in section 2.2.2 is founded on the power law velocity profile, and we want to show how the power law boundary layer description in general can be extended to the large full scale ship Reynolds numbers.

2.1 Ship model experiments

When we performed the ship model experiments, the models were towed by the carriage, total towing force R_{Tm} was measured at different speeds. The towing point was at the midship section on the main deck. The sinkage at FP and AP were also logged to find the speed dependent trim of the vessel.

We follow ITTC recommendations, and divide the total resistance into a frictional part and a rest part, called the residuary resistance, C_{Rm}. In coefficient form we can write this

$$C_{Tm} = \frac{R_{Tm}}{\frac{\rho_m}{2} V_m^2 S_m} = C_{Fm}(1+k) + C_{Rm} + C_{AAm} + C_{BDm} \tag{2.1}$$

where C_{Fm} is the frictional resistance coefficient. This is called the "1978 ITTC performance prediction method" Where C_{AAm} is the air resistance coefficient and C_{BDm} is base drag. The International Towing Tank Conference (ITTC) recommends to use the following formula to estimate skin friction correlation line

$$C_{Fm} = \frac{0.075}{(\log Rn_m - 2)^2} \tag{2.2}$$

Where Rn_m is Reynolds number based on model length

$$Rn_m = \frac{V_m L_m}{\nu_m} \tag{2.3}$$

It exists many of these correlation lines, all of which builds on empirical data for 2D flow. Eq. (2.2) is based on an extensive and thorough series of flat plane tests by Hughes [15] and [16]. In [34] the authors take a look at the ITTC line and its genesis. They also present other skin friction lines, and they give credit to the existing ITTC line.

Prandtl was the first to propose this form of a convienient interpolation formula.

$$C_F = a(b + \log Rn)^c \tag{2.4}$$

This has ever since been the governing formula for flat plate skin friction, only with different parameters a, b and c. Granville gives an outstanding outline of different methods to estimate skin friction on surface vessels in [9].

Further we have from eq. (2.1) the form factor k. This is a non-dimensional scalar which contains the three-dimensionality of the flow around the model hull. This factor is assumed to be independent of Reynolds number and Froude number. That means it has the same value for model and ship at all velocities.

Tanaka [33] however divides the form factor into two parts. First a frictional part which is independent of Rn, and second a pressure part which is proportional to ($C_F^{-1} \sim C_F^{-1/2}$). This method has not been widely used, probably because it is far more complex than the ITTC 1978 method.

The last cofficient in eq. (2.1) is the residuary coeffiecient C_{Rm} which is mainly the resistance coefficient due to free-surface wave formation. From here on we assume that the residuary resistance is equal to the wave resistance.

Froude came up with a hypothesis that the residuary resistance is the same for model and ship if we scale the velocity in a certain way

$$Fn = \frac{V_m}{\sqrt{gL_m}} = \frac{V_s}{\sqrt{gL_s}} \tag{2.5}$$

This is the Froude number. Subscripts m means model, and s means ship. This gives us

$$C_{Rm} = C_{Rs} = C_R = C_W \tag{2.6}$$

And from eq. (2.1) we have

$$C_W = C_{Tm} - C_{Fm}(1+k) - C_{AAm} - C_{BDm} \tag{2.7}$$

Where C_{AAm} is aerodynamic drag coefficient and C_{BD} is transom stern drag due to dry transom stern. The model test results for the towing force is presented in terms of the wave resistance coefficient.

Prohaska/Inuis method This is a method to find the form factor k by the use of experiments. For low Fn the wavemaking resistance is small compared to viscous resistance. C_W is then assumed to be

$$C_W = const\, Fn^n \tag{2.8}$$

with $3 \leq n \leq 6$, and *const* is a constant. From eq. (2.1) we then have

$$\frac{C_{Tm}}{C_{Fm}} = (1+k) + const\, \frac{Fn^n}{C_{Fm}} \tag{2.9}$$

When C_{Tm}/C_{Fm} is plotted as a function of Fn^n/C_{Fm} we get a straight line with slope *const*, and the intersection with the ordinate axis gives the value of $(1+k)$ which we seek, see fig. 4.39 in sec. 4.2.2.

The obvious problem with this method is that we measure the towing force at low model velocity. This means the towing force is small, and the experimental setup is designed to handle much larger forces. The force fluctuations are often the double of the mean force value. This gives large relative errors for the towing force values. As we can see from fig. 4.39 it is difficult to uniquely find a value for $(1+k)$.

Another major problem with this method is that the ship model is towed at relatively low Rn, typically around $5 * 10^6$. Even though there is sandstrip for turbulence trigging in the bow of the ship, the laminar flow may survive this trigging, and extend further downstream towards midship of the model. This gives a lower resistance than with all turbulent flow, and introduces error in the estimate of the form factor, because we assume all turbulent flow.

A last moment with the method is that even at very low vessel speeds, there could be waves generated by the bulb. These waves have an effect on the total resistance, and since we assume no waves generated by this method, there will be an error in k due to these waves.

The ship we are testing has a transom stern. This gives another embarrassing problem when we estimate the form factor at low velocities (typically $Fn < 0.2$), and use this factor to estimate ship resistance at higher velocities ($Fn > 0.3$). For low velocities the transom stern is wet, while for higher velocities the transom stern is dry. A dry transom stern gives a loss of hydrostatic pressure from the transom, and an increase in drag. For the vessel with dry transom stern, this transom stern drag resistance can be calculated by

$$D_B = \rho g \int_0^h (h - z) B(z)\, dz \tag{2.10}$$

where h is maximum submergence of transom, z is distance from lowest point on transom and $B(z)$ is breath of transom at submergence z. The transom stern drag coefficient is given by

$$C_{DB} = D_B / (1/2 \rho U_\infty^2) \tag{2.11}$$

The ship model tested in chapter 4 has a transom stern, but it has no submerged area for zero sinkage and trim. When the ship is moving it has both sinkage and trim. The transom stern drag is estimated in chapter 4.2.2.

2.2 Theoretical development of "Optimized velocity distribution"

2.2.1 Boundary layer analysis for 2D turbulent flow

Boundary layer profiles for turbulent flow

In this study we assume turbulent flow for the flow on the body surfaces. In a boundary layer (BL) there is zero velocity at the wall. Further out from the wall, the flow velocity will asymptotically approach the free stream velocity. For turbulent flow we have to describe this BL velocity distribution with empirical formulas.

Kàrmàn and Prandtl was the first to describe this BL mathematically. He introduced the $1/n$-th power law in the early 1920s. The disadvantage with this description is that the exponent n is Rn-dependent. The fluid dynamicists of that time, with the aid of Prandtls mixing length theory soon came up with a new BL theory, the logarithmic velocity-distribution law. The advantage with this theory is that it can be used for arbitrarily large Rn-numbers.

There also exists other ways of describing the boundary layer in turbulent flow. Van Driest came up with his BL theory in 1956, [37]. He describes the velocity profile with an integral expression.

P.Å. Krogstad has also done considerable work on this topic, especially for rough walls, as for instance in [18].

BL profiles for turbulent flow on flat plate

Logarithmic law According to the logarithmic law the velocity profile in the overlap layer of the boundary layer for a flat plate can be written, see [40]

$$u^+ = \frac{u}{v^*} \approx \frac{1}{\kappa} \ln(y^+) + B \tag{2.12}$$

where $y^+ = y\, v^*/\nu$ and $v^* = \sqrt{\tau_w/\rho}$. Further are κ and B near-universal constants for turbulent flow past smooth walls. An outline of this boundary layer theory can be found in [25] or [40]. In this thesis we use the values

$$\kappa = 0.41 \qquad B = 5.3 \tag{2.13}$$

Local friction coefficient C_f is related to wall shear stress τ_w by

$$C_f = \frac{\tau_w}{1/2\rho U_\infty^2} \tag{2.14}$$

In [40] on page 433-434 White gives a relation between Rn_x and local friction cofficient C_f. This is a result of the logarithmic law, eq. (2.12) substituted into the boundary layer momentum equation for flat plate.

The relation for Rn_x and C_f becomes

$$Rn_x \approx 1.73\, e^Z \left[Z^2 - 4Z + 6\right] \tag{2.15}$$

where

$$Z = \kappa\sqrt{\frac{2}{C_f}} \tag{2.16}$$

This is a relation with C_f implicitly defined, and can be solved with an iterative procedure. Matlab has an excellent function for this, and C_f from the logarithmic law is plotted in fig. 2.1. With C_f found, we can find momentum thickness from flat plate momentum-integral equation

$$\frac{d\delta_2}{dx} = \frac{C_f}{2} \tag{2.17}$$

Boundary layer thickness is defined as the distance from the wall where the flow velocity is 99% of free stream velocity. Displacement thickness and momentum thickness is given by

$$\delta_1 = \int_0^\infty \left(1 - \frac{u}{U_e}\right) dy \tag{2.18}$$

$$\delta_2 = \int_0^\infty \frac{u}{U_e}\left(1 - \frac{u}{U_e}\right) dy \tag{2.19}$$

Power law The power law BL formula can be written

$$\frac{u}{U_\infty} = \left(\frac{y}{\delta}\right)^{\frac{1}{n}} \tag{2.20}$$

where u is flow velocity at distance y from the wall, U_∞ is freestream velocity at the edge of BL and δ is BL thickness.

In [42] Wieghardt treats the power law formula for large Rn. He also has a comparison between the power law formula and the logarithmic formula. The power law formula with inner variables can be written

$$\frac{u}{v^*} = C(n)\left(\frac{yv^*}{\nu}\right)^{\frac{1}{n}} \tag{2.21}$$

where

$$C(n) = \frac{n}{\kappa}e^{-(1-\kappa B/n)} \tag{2.22}$$

From the momentum equation for flat plate, eq. (2.17) we have

$$\left(\frac{v^*}{U_\infty}\right)^2 = \frac{\tau_w}{\rho U_\infty^2} = \frac{d\delta_2}{dx} \tag{2.23}$$

From eq. (2.18) toghether with eq. (2.20) we can calculate momentum thickness δ_2 as a function of BL thickness δ

$$\delta_2 = \frac{n}{(1+n)(2+n)}\delta \tag{2.24}$$

We can find a relation for δ by setting $u = U_\infty$ for $y = \delta$ in eq. (2.21), then we put this into eq. (2.23), together with eq. (2.24) for δ_2. Putting $u = U_\infty$ for $y = \delta$ requires a comment, since we should have set $u = 0.99 * U_\infty$ for $y = \delta$. Historically the power law formula was developed from pipe flow, and Nikuradse did considerable work on this, see [25]. In fully developed pipe flow, the pipe radius corresponds to the boundary layer thickness δ. Prandtl has a fundamental assumtion that the velocity distribution in the boundary layer on a flat plate is identical with that inside a circular pipe.

It turns out that the factor 0.99 would cancel out because using it means it appears also in eq. (2.20).

Now we solve for δ which gives

$$\delta = f_1(n)\, x\, Rn_x^{-\frac{2}{3+n}} \tag{2.25}$$

where x is distance from leading edge, and $Rn_x = xU_\infty/\nu$ is local Reynolds number. Further

$$f_1(n) = \left[\frac{(2+n)(3+n)}{n}\right]^{\frac{1+n}{3+n}} C(n)^{-\frac{2n}{3+n}} \tag{2.26}$$

The local friction coefficient is given by eq. (2.17), and becomes

$$C_f = 2\,\frac{n}{(1+n)(2+n)}\frac{d\delta}{dx} = f_2(n)\,Rn_x^{-\frac{2}{3+n}} \tag{2.27}$$

where

$$f_2(n) = 2\,\frac{1+n}{3+n}\,\frac{n}{(1+n)(2+n)}\,f_1(n) \tag{2.28}$$

Stratfords velocity distribution which we shall outline in the next section is founded on the power law velocity distribution with Reynolds numbers in the vicinity of $10^6 \sim 10^7$. Our ship flows have a Reynolds number beyond 10^9. We therefore have to extent Stratfords theory to our Reynolds numbers. The first step in this extention is to consider the velocity profiles used and their Reynolds number dependency.

On a typical pram-type ship which we consider in this study, the aft shoulder is typically between section 4 and 6, see figs. 3.20, 3.21 and 3.22. This means that the local Reynolds number at the aft shoulder would be typically 10^9, which is the Reynolds number of the velocity profile plotted in fig. 2.1. The ship flow will not be a flat plate flow, but we use flat plate flow here as an example of Reynolds number dependecy of boundary layer flow and its connection to Stratford flow. The properties of the boundary layer flow at the aft shoulder is input to Stratford flow.

It must be emphasized that in the optimization calculations in section 3.4 we have accounted for the varying pressure distribution in the fore part of the ship.

To make a comparison between the logarithmic velocity profile description and the power law velocity profile description of the boundary layer, we have plotted a typical BL velocity profile for both profiles in plot (a) in fig. 2.1. The Reynolds number for this profile is $9.578 * 10^8$, and is a typical full scale Rn for aft shoulder of our ship.

In plot (b) and (d) in fig. 2.1 momentum thickness δ_2 and local friction coefficient C_f is shown. All calculations are for flat plate flow, and come from the formulae above.

Plot (c) in fig. 2.1 shows the number n as a function of Rn_x for the plate flow. The dots are taken from data in [41], and the full line is a spline interpolation for other Reynolds numbers.

These figures show that if we make the exponent n in the power law dependent on Reynolds number along the plate flow, this power law corresponds quite well

with the logarithmic law. The point is that the power law with the exponent $n = 7$ only holds for $5 * 10^5 < Rn_L < 10^7$, while the logarithmic law holds for arbitrary Rn. When we extend the power law with the given Rn dependency for n, we see that it gives a fair description of boundary layer also for Rn up to 10^9.

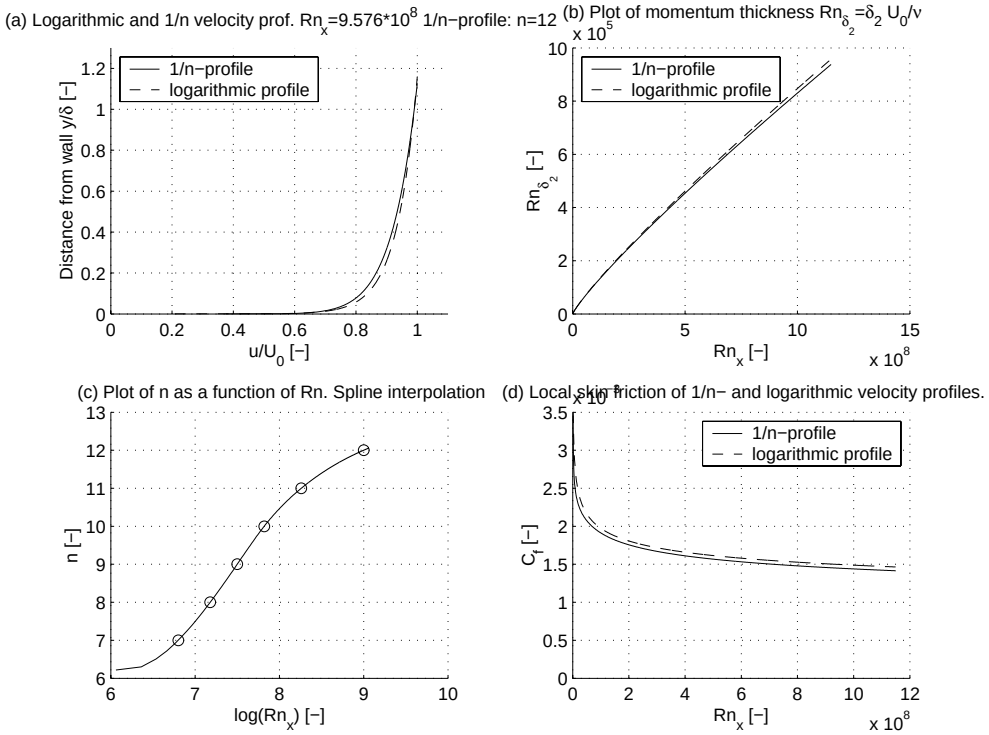

Figure 2.1: *(a) Comparison of* $1/n$ *and logarithmic velocity profile along a flat plate with a typical ship length and speed. (b) Plot of momentum thickness Reynolds number for the velocity profiles in plot (a). (c) Plot of exponent in* $1/n$ *profile. (d) Plot of local skin friction,* C_f*.*

2.2.2 Stratford velocity distribution

Derivation

In the derivation of the Stratford velocity distribution we follow Stratford's notation, and this section is a short summary of his paper [31] with application to our problem.

We examine a turbulent incompressible flow on a 2D profile. The flow over the profile begins to decelerate at point $s = s_0$. The length s_0 is not the physical length along the 2D profile, but is an equivalent length with boundary layer thicknesses for flat plate and flow along profile involved. This is outlined at the end of this section.

The thickness y_0 of the profile is the draft T of the hull. The profile is mirrored over the sea surface, and the transom draft is zero. That means we examine the centerline of a pram-type ship hull.

The velocity U_0 is the maximum velocity in the aft part of the profile, and will in most cases occur at the point $s = s_0$, but not necessarily. See fig. 2.2 for illustration of the flow and body we analyze.

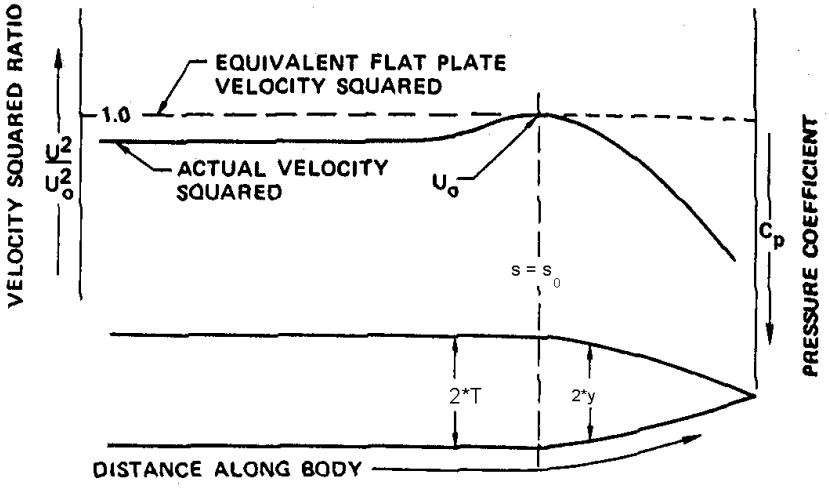

Figure 2.2: *Schematic illustration of the flow pressure coefficient over the aft body with peak velocity U_0 at point $s = s_0$. From [28].*

Outer layer The shear forces are supposed zero downstream of s_0. In [31] Stratford derives Bernoullis equation for a streamline downstream of s_0

$$\frac{1}{2}\rho u^2(s,\psi) = \frac{1}{2}\rho u'^2(s,\psi) - (p - p_0), \qquad (\psi \geq \psi_i) \tag{2.29}$$

and he further shows that

$$\left[\frac{\partial u}{\partial y}\right]_{(s,\psi)} = \left[\frac{\partial u'}{\partial y'}\right]_{(s,\psi)}, \qquad (\psi \geq \psi_i) \tag{2.30}$$

This is valid only for streamlines in the outer layer of the velocity profile, $\psi \geq \psi_i$. The dash denotes the comparison profile just downstream of s_0, while the values on the left side represents any point downstream of the comparison profile.

Stratford points out that "the effect of the pressure rise in the outer part of the boundary layer in this region is to cause a general lowering of the velocity profile rather than a change in shape". We can therefore keep the same shape of the velocity profile in the outer layer all the way downstream on the body profile.

From the definition of a stream function we can write

$$\psi = \int_0^y u\, dy \tag{2.31}$$

We have assumed the forward flow to be along a constant thickness profile. We can then use the comparison profile of Stratford in the boundary layer without pressure rise, eq. (2.20)

$$\frac{u'}{U_0} = \left(\frac{y'}{\delta'}\right)^{1/n} \tag{2.32}$$

where boundary layer thickness is for a generalized exponent $1/n$, eq. (2.25)

$$\delta' = \left[\frac{n}{(2+n)(3+n)}\right]^{-\frac{1+n}{3+n}} C(n)^{-\frac{2n}{3+n}}\, s \left(\frac{U_0 s}{\nu}\right)^{-\frac{2}{3+n}} \tag{2.33}$$

and momentum thickness, eq. (2.24)

$$\delta_2' = \frac{n}{(1+n)(2+n)}\delta' \tag{2.34}$$

our equation for boundary layer thickness is valid for Reynolds numbers from 10^6 to beyond 10^9. For full scale ships in this study we have typically Rn up to $1.2 * 10^9$.

In [31] Stratford uses $1/n = 1/7$ for his derivation of the "optimized velocity distribution".

As shown in sec. 2.2.1 we can generalize the 1/7 profile to be valid for larger Rn numbers than 10^7. Our derivation of the Stratford velocity distribution will proceed with this generalized $1/n$ velocity profile, but otherwise we stick to Stratfords derivation.

Inner layer The derivation of the inner layer formula is based on Prandtls mixing length formula, $l = \kappa y$. Here κ is Karmans constant equal to 0.41. After using Prandtls expression for the shear stress in the inner layer toghether with the fact that the pressure forces must be equal to the gradient of the shear stress, Stratford comes up with

$$\left(\frac{\partial u}{\partial y}\right) = \left(\frac{1}{\rho\kappa^2}\frac{\partial p}{\partial s}\right) y^{-\frac{1}{2}} \qquad (\tau_w = 0,\ y\ small) \tag{2.35}$$

Stratford integrates this equation with no slip at the wall , $u = 0$ at $y = 0$. He also introduces an empirical factor β which he says is used "due to that we have omitted higher terms in the profile expansion, the profile has been overidealized as regards its own shape".

Stratfords idealized profile in the inner layer can then be written

$$\frac{1}{2}\rho u^2 = \frac{2}{(\kappa\beta)^2}\frac{\partial p}{\partial s} y \qquad (\tau_w = 0,\ y < y_i) \tag{2.36}$$

Joining inner and outer layers Stratford uses continuity of the quantities ψ, u and $\frac{\partial u}{\partial y}$ between the inner and the outer layer. He uses the matching condition

$$\psi \left(\frac{\partial u}{\partial y}\right)^3 = \psi' \left(\frac{\partial u'}{\partial y'}\right)^3 \tag{2.37}$$

When we use eq. (2.31) toghether with eq. (2.36) in the matching condition eq. (2.37), Stratford came up with the following equation

$$\left(\frac{y'}{\delta'}\right)^{\frac{(2n-4)}{n}} = \frac{3(\kappa\beta)^4}{(1+n)\left(n\,\delta'\,\frac{d\bar{C}_p}{ds}\right)^2} \qquad (\psi = \psi_i) \tag{2.38}$$

introducing

$$\bar{C}_p = (p - p_0)/\frac{1}{2}\rho U_0^2 \tag{2.39}$$

Note that $\bar{C}_p$ is defined relative to peak velocity U_0, not free stream velocity U_∞. Eq. (2.38) is still valid for our generalized form of the velocity profile with $1/n$. Further Stratford matches $u^2/(\psi \frac{\partial u}{\partial y})$ in the same manner, achieving

$$\frac{u^2}{u'^2} = \frac{3}{(1+n)} \qquad (\psi = \psi_i) \tag{2.40}$$

When we use eq. (2.38) together with eq. (2.40) and substitute for δ' from eqs. (2.33) and (2.34) we get after some algebra

$$(2\bar{C}_p)^{\frac{(n-2)}{4}} \left(s\frac{d\bar{C}_p}{ds} \right)^{\frac{1}{2}} = K_1(n)\beta Rn^{\frac{1}{(3+n)}} \qquad \left(\bar{C}_p \leq \frac{n-2}{n+1} \right) \tag{2.41}$$

where $Rn = sU_0/\nu$ and

$$K_1(n) = \kappa\, 3^{\frac{1}{4}} \left(2\,\frac{n-2}{1+n} \right)^{\frac{(n-2)}{4}} \left[\frac{n}{(2+n)(3+n)} \right]^{\frac{1}{2}\left(\frac{1+n}{3+n}\right)} \frac{C(n)^{\frac{n}{3+n}}}{n^{\frac{1}{2}}(1+n)^{\frac{1}{2}}} \tag{2.42}$$

Separation will now occur when the left hand side equals right hand side of eq. (2.41) according to Stratford.

Stratford points out that the limitation in $\bar{C}_p$ in eq. (2.41) comes from the fact that the join of the inner and outer layer not should reach the edge of the boundary layer.

The value of s_0 The value of s_0 is the equivalent length for a flat plate to achieve the same boundary layer momentum thickness δ_{20} as our actual 2D profile will have, when the velocity at $s = s_0$ is u_0.

For our body profiles we have turbulent flow from the leading edge. The criterion is then

$$s_0 = \int_0^{s_1} \left(\frac{u}{U_0} \right)^3 ds \tag{2.43}$$

where s_1 is distance from bow where the pressure rise starts on the actual body. Further is s_0 the equivalent distance for the flat plate flow.

The parameter β In [30] Stratford designed a test wall in a wind tunnel where he achived a large region with almost separating flow, satisfying eq. (2.41) (for $1/n = 1/7$). In these experiments he is able to calculate a value for the parameter β. He finds that β is independent of $\bar{C}_p$, and has the value

$$\beta = 0.66 \qquad (\tau_w \equiv 0,\ \bar{C}_p \leq \frac{n-2}{n+1}) \tag{2.44}$$

The final form of Stratford's formula

Eq. (2.41) is a differential equation giving a separation criteria for a 2D pressure recovery flow. Stratford postulates this equation can be integrated to give a criteria for almost separating flow from point s_0 and downstream. We integrate this equation from point s_0 to the actual point s on the body surface. We then get a formula for $\bar{C}_p$

$$\bar{C}_p(s) = K_2(n)^{\frac{2}{n}} \left\{ \beta^2 Rn_0^{\frac{2}{3+n}} \left[\left(\frac{s}{s_0} \right)^{\frac{2}{3+n}} - 1 \right] \right\}^{\frac{2}{n}} \qquad (\tau_w \equiv 0,\ \bar{C}_p \leq \frac{n-2}{n+1}) \tag{2.45}$$

where $Rn_0 = s_0 U_0/\nu$ and

$$K_2(n) = \frac{n(3+n)}{4}\, 2^{-\frac{n-2}{2}}\, K_1(n)^2 \tag{2.46}$$

For $n = 7$ eq. (2.45) is the same as eq. (24) in [31] by Stratford.

2.2.3 Comments on the Stratford velocity distribution

In [21] Liebeck has some very interesting comments on the Stratford velocity distribution. A short summary of his comments are given here, because they are vital for an understanding for what this Stratford distribution can be used for, and how it should be used.

The Stratford distribution is the shortest possible pressure recovery region. A steeper curve will cause separation, and a milder curve will not cause separation in that region. The Stratford velocity distribution, eq. (2.45) is not strictly tied up to be an equation where we have separation everywhere on the region. It can also be considered as an equation describing a flow with a

certain "margin" to separation. The peculiar characteristic about this Stratford velocity distribution is that it has the same tendency for separation all along its length. That means the BL has the same margin to separation at the trailing edge as at the beginning of the pressure recovery. This margin is controlled with the parameter β. Liebeck points out that when this margin is used up, separation will occure simultaneously everywhere on the recovery region.

Liebeck also states that the term "margin" is difficult to define in terms of conventional BL theory.

Fig. 2.3 shows a comparison of two Stratford distributions (curve a and c) and a modified Stratford distribution (b) for flow with constant velocity for a given distance, and with Stratford flow at the aft part. This is typically flow velocity in a diverging channel. Stratford made his verification of his theory in a diverging channel with this kind of velocity profile, [30]. The Stratford distribution is given by eq. (2.45). By comparing curves (a) and (c) we see that the higher the Rn, the shorter is the recovery region. Both curves (a) and (c) have the shortest possible pressure recovery region for their respectively Reynolds numbers. Curve (b) is a modified Stratford distribution from curve (a). We have decreased the value of β, this gives a larger region with Stratford distribution, and an increased margin before separation. All three plots have the same pressure recovery.

Smith has some noteworthy statements in his article [28]: "The significant conclusion to be made from this [their] example is that tail shapes in fully turbulent flow are not appreciably affected over a wide range of Reynolds numbers. Thus, a tail that is optimally designed for the lower end of the anticipated Reynolds number range will be nearly optimum with increasing Reynolds number. Alternatively, if the design process has some built-in conservatism, e.g., a reduced value of the constant in [their] Eq. (2) [equivalently β here], then Reynolds number should not play an important role in tail design."

From a practical point of view this is an important statement, and shows that a tail design with a Stratford distribution can be applicable to a large speed range due to the only weak Reynolds number dependency. We will use this in our tail designs in the next chapter.

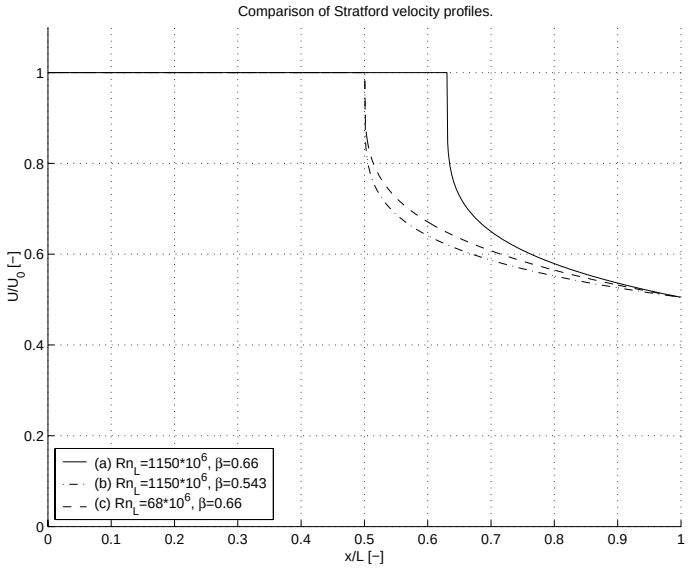

Figure 2.3: *The figure shows a comparison of Stratford velocity profiles with varying the parameter β and varying Rn based on length.*

Chapter 3

Numerical procedures and optimized ship hulls

This chapter deals with the numerical procedures used to calculate the optimized ship hulls. In the first section we look through what has formerly been done on optimization methods generally, and applied to ship hulls specially. In section 3.2 we have a look at the direct numerical procedure which is used in the inverse method outlined in section 3.3. In section 3.4 we present the optimized 2D profiles which we have calculated with the developed inverse method. In the last section of this chapter the design procedure concerning 3D hull form design from our 2D profiles are outlined. Drawings and technical data for the ship hulls are also given.

3.1 Introduction to inverse design methods in 2D and 3D

One of the first successful inverse methods for 2D and axisymmetric flow were developed by Bristow, and described in [4]. He uses the Douglas Neumann boundary element surface source singularity method for direct calculation of the velocity distribution. He then uses an iterative method which calculates the velocity distribution over the actual body, compares this actual velocity distribution (AVD) with the prescribed velocity distribution, PVD. The body geometry is changed until the AVD of the body corresponds to the PVD. He reports excellent results both for 2D and axisymmetric flows.

Also Lewis in [19] and [20] has a similar approach. For the direct calculations he uses a surface vorticity distribution. Also in this method he starts with an initial geometry, calculates the AVD and compares with the PVD. Each element of the body is changed with an incremental angle corresponding to the difference in AVD and PVD on the actual element position. This procedure is repeated until AVD corresponds to PVD. Lewis was kind to send us a copy of his software. We did not find it to work satisfactorily for our bodies and PVD.

The next method we tried out was extensively used for inverse design of turbomachinery, and is oulined in [36] and [35]. This method uses a direct flow solver, and starts with an initial geometry. The difference in AVD and PVD is calculated and used as an input to the modification algorithm. The geometry modification is in this method controlled by a transpiration model. It considers the old blade wall porous with a normal velocity going through it, proportional to the difference in AVD and PVD. At the same time it requires mass balance, and the actual change of each element normal to the surface is determined by this mass balance. This method was very sensitive to the flow in the nose section, and gave quite large errors further aft with only a small error in the nose section. This was because the iteration started in the nose section and went aftwards, and accumulated small errors all the way to the aft part. This method was also abandoned.

The areas of applications for inverse methods in fluid dynamics are extensive. Lee et. al. [28] uses Bristows method to design minimum tail shapes for bodies of revolution. They use Stratford flow for axisymmetric bodies as a PVD, and the tail shape is calculated. He finds extremely short tails for some fore geometries. He also concludes that the Bristow method is well suited to design these type of bodies.

Inverse design tools are also used in 3D applications the latest years as hardware power is increasing. In [5] Cheng-Hung Huang et al optimizes the shape of a ships bow with the aid of an inverse design method. They use the B-splines surface fitting and Levenberg-Marquardt method as inverse method. They report that the bow sections were successfully designed with the developed inverse method.

Tahara et. al. optimize the stern of a ship in [32] with respect to minimization of delivered power to propeller. They use a CFD-based optimization method with a Reynolds-averaged Navier-Stokes equation solver. The optimizations are done at typical model scale Reynolds numbers ($\approx 10^6$). They conclude that the method appeared to successfully optimize the given stern form.

In [7] Nagamatsu et. al. minimize viscous resistance of 2D bodies and 3D full forms under certain design constraints. The frictional and viscous pressure resistances are calculated by use of boundary layer calculations based on a higher order theory. A direct search method is used to obtain a solution of minimizing the viscous resistance. This is achieved by repeatedly changing the design variables systematically until it gets to the minimum value.

The 3D optimization methods are done with a relatively small number of control points, because the methods require much data power, or that they will not converge with large number of control points. They conclude that further investigations are necessary, and that inverse methods will be a useful tool in ship design in the future.

3.2 Direct flow calculation with vortex distribution

3.2.1 Surface vorticity model for plane 2D flow

The direct flow calculations were done by a surface vorticity model for plane 2D flow outlined in [19]. This book treats this method in full detail with programming examples. It also gives satisfactory results for 2D flow, and is a fairly easy method to program. It was therefore decided to use this method for the direct flow calculations which are input to the inverse method outlined in 3.3.

The basis for the surface vorticity model is Biot Savarts law. This law gives the velocity induced dq_{mn} at the observation point (x_m, y_m) from a small vortex element $\gamma(s_n)ds_n$ at the pivotal point (x_n, y_n), see fig. 3.1. The induced velocity is normal to the vector r_{mn} connecting the two points. Biot Savarts law then gives the result for the induced velocity dq_{mn} at observation point (x_m, y_m).

$$dq_{mn} = \frac{\gamma(s_n)ds_n}{2\pi r_{mn}} \tag{3.1}$$

The induced velocity is resolved into a component parallel to the body surface, and a component normal to the body surface.

To find the boundary condition to solve the problem, we take a quick look into the neatness of the surface vorticity model. The surface vorticity element induces velocities U_{so} just outside and U_{si} just inside the body surface. We

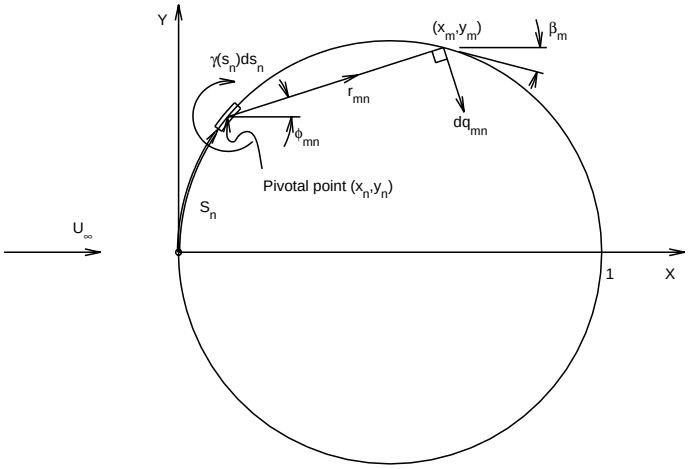

Figure 3.1: *Discrete surface vorticity model for a 2D body. Velocity induced by surface element at* s_n

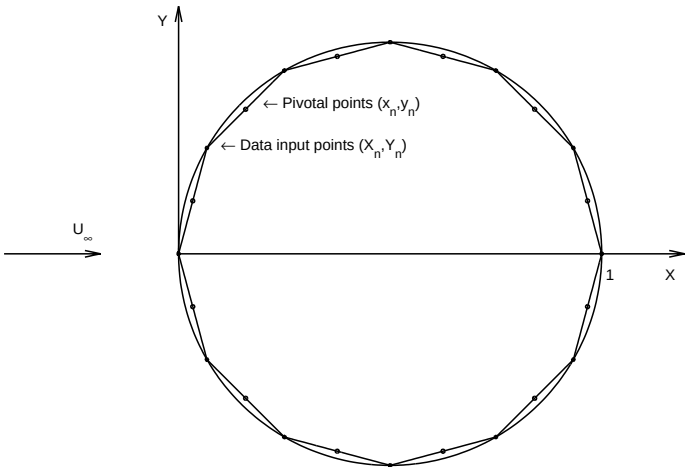

Figure 3.2: *Representation of body surface by straight line elements.*

put a rectangular contour around the vortex element, and due to cancellation of velocities normal to the surface, we are left with the following equation

$$(U_{so} - U_{si})ds_n = \gamma(s_n)ds_n \tag{3.2}$$

That is, the circulation around the rectangular contour defined clockwise positive is equal to the total amount of vorticity enclosed by the contour.

To satisfy the boundary condition at observation point (x_m, y_m) we have to specify zero velocity on the body surface just inside the vortex sheet.

$$U_{si} = 0 \tag{3.3}$$

we then have

$$U_{so} = U_s = \gamma(s_n) \tag{3.4}$$

Equation (3.4) gives us the necessary boundary condition at s_m

$$-\frac{1}{2}\gamma(s_m) + \oint k(s_m, s_n)\gamma(s_n)ds_n + U_\infty \cos\beta_m = 0 \tag{3.5}$$

The last term is the component of U_∞ resolved parallel to the body surface at m. The coupling coefficient is given by

$$k(s_m, s_n) = \frac{1}{2\pi}\left\{\frac{(y_m - y_n)\cos\beta_m - (x_m - x_n)\sin\beta_m}{(x_m - x_n)^2 + (y_m - y_n)^2}\right\} \tag{3.6}$$

Equation (3.5) is a result of summing the induced velocities on the observation point (x_m, y_m) from all vortex elements around the body surface. We also have to add the component of U_∞ resolved parallel to the body surface to these induced velocities. These sums equals the vorticity the vortex element induces on itself, which is $\frac{1}{2}\gamma(s_m)$.

We also take into account the self-induced velocity of the surface vorticity element on the observation point due to the curvature of the body at the actual location. The self-induced velocity on the observation point then becomes

$$\left(-\frac{1}{2} - \frac{\Delta\beta_m}{4\pi}\right)\gamma(s_m) \tag{3.7}$$

where $\Delta\beta_m$ is the change of profile slope from one end of the element to the other.

Use of sub-elements was also introduced and tested. Each vortex element were divided into N equal sub-elements. This method gave better results for very thin profiles, but for the profiles used in this study it had insignificant effect. It was although used 2 or 3 sub-elements for the profiles studied here.

The numerical implementation of this method is very simple. The data input points (X_n, Y_n) are specified with M+1 points, see fig. 3.2. Each pivotal point (x_n, y_n), profile slopes β_m and element lengths Δs_n are calculated.

The boundary condition equation (3.5), can formally be written

$$\boldsymbol{K\gamma} = -U_\infty cos\boldsymbol{\beta} \tag{3.8}$$

where

$$K_{mn} = K(s_m, s_n) = k(s_m, s_n)\Delta s_n \tag{3.9}$$

for $m \neq n$ and

$$K_{mm} = K(s_m, s_m) = -\frac{1}{2} - \frac{\Delta\beta_m}{4\pi} \tag{3.10}$$

We now solve eqn. (3.8) to find the vortex distribution on the body surface

$$\boldsymbol{\gamma} = -\boldsymbol{K^{-1}}\,(U_\infty cos\boldsymbol{\beta}) \tag{3.11}$$

From eqn. (3.4) the potential flow velocity close to the body surface $\boldsymbol{U_s}$ is immidiately known, being exactly equal to the surface vorticity $\boldsymbol{\gamma}$. The circulation around the entire body is zero due to symmetri.

3.2.2 Numerical check of the surface vorticity method

The numerical check of the calculation method is done on ellipses with different ratio between semi axis and major axis: b/a. We compare with the exact analytical solution. In fig. 3.4 is calculated RMS of error between numerical flow velocity and exact flow velocity

$$RMS = \sqrt{\sum_{i=1}^{N}(U(i) - U_{exact}(i))^2/N} \tag{3.12}$$

We see that the numerical solution converges rapidly with increasing number of elements. For ellipses with profile thickness ratio $b/a = 0.2$ and thicker, the error is very small. The profiles used further in this study have a profile thickness ratio of approximately 0.2. For these profiles we see that this numerical method gives satisfactory results.

In fig. 3.3 is calculated flow velocity over an ellipse with $b/a = 0.04$, wich corresponds to the thinnest profile tested in fig. 3.4.

Fig. 3.5 shows a log-plot of the flow velocity in the nose section of an ellipse. When we compare calculated results and analytical results we see that for the elements in the front of the nose the calculated results diverge from the analytical results. When approximating the very curved nose of an ellipse with straight line elements we introduce an error. With this method we calculate the velocity at the midpoint of the elements, which mean we in reality calculate the velocity a little bit inside the real surface. The curvature correction factor in eq. (3.7) should take care of this error to a certain extent, but we have not achieved a full correction of this curvature effect.

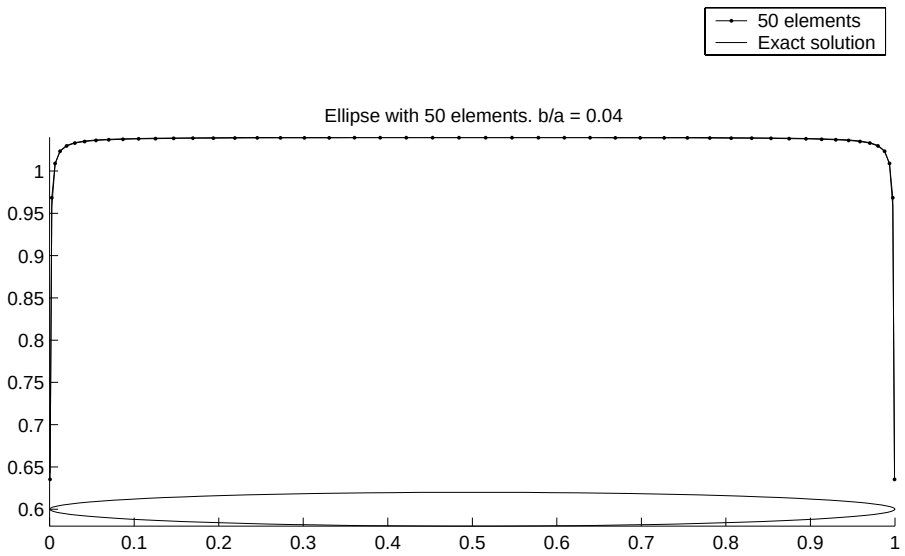

Figure 3.3: *Flow velocity over ellipse. Comparison between numerical calculation and exact calculation.*

3.3 Inverse design with vortex distribution

The problem of finding the body profile with a velocity distribution U_a, corresponding to the desired velocity distribution U_d, is outlined in fig. 3.6. For the inverse problem the hull form of the aft part of the ship is regarded as being unknown, and controlled by a set of control points.

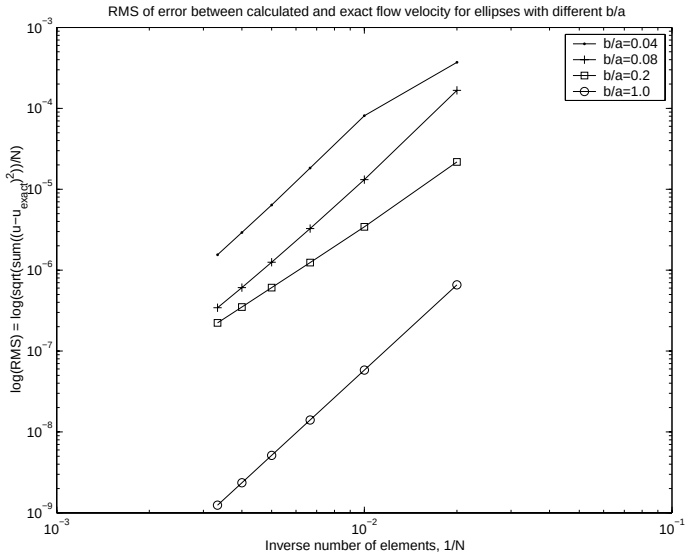

Figure 3.4: *Convergence study of numerical calculation of flow velocity over ellipses with different b/a*

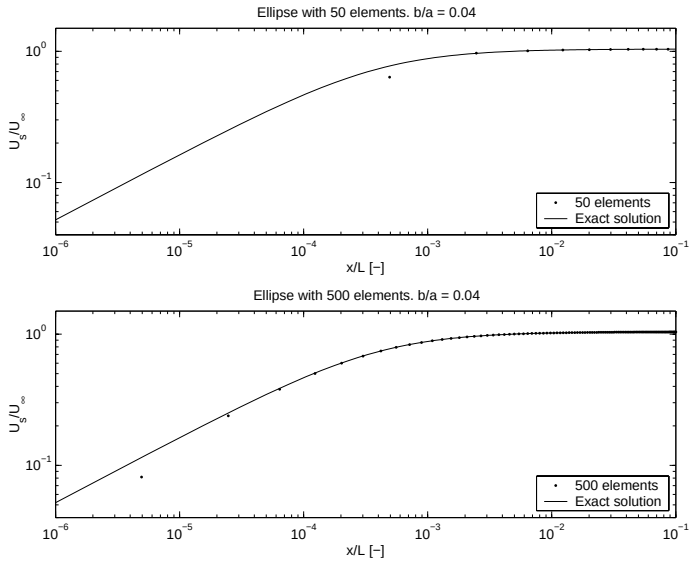

Figure 3.5: *Potential flow velocity over fore part of ellipse, $x/L < 0.1$. Calculated with surface vorticity method. Comparison between numerical calculation and exact calculation.*

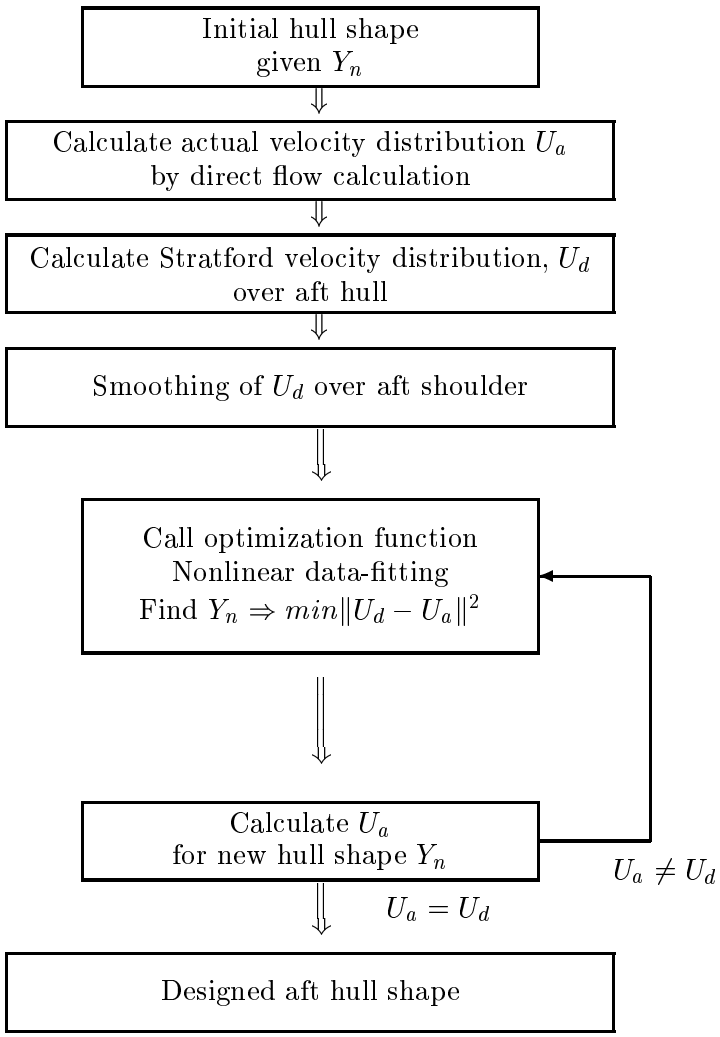

Figure 3.6: *The optimum shape design methology*

Consider a geometry of M elements (upper half of body) illustrated in fig. 3.2 and discussed in sec. 3.2. Input to calculations are number of elements M and xrange data input points X_n. The yrange data points Y_n are variables in the inverse process. That is find the set $Y_n\,(1 \leq n \leq M)$ such that the quantity

$$\min_Y \frac{1}{2}\|U_d - U_a\|^2 = \min_Y \frac{1}{2}\sum_{n=1}^{M}[U_d(n) - U_a(n)]^2 \tag{3.13}$$

is minimized, where U_d are prescribed velocity distribution along the surface of the body on the data points X_n. U_a is actual velocity distribution, and is a function of X_n, Y_n. In other words, we want to find a set of $Y_n\,(1 \leq n \leq M)$ which is a body geometry such that the actual velocity distribution U_a over the body as much as possible equals the desired velocity distribution U_d.

In the minimization process it was used a function from Optimization Toolbox in Matlab. The function is called lsqnonlin, and the input to the function is another function which calculates the velocity difference $U_d - U_a$, and an initial geometry $Y0_n$. The syntax is

$$Y = \text{lsqnonlin}(@\text{diffudua}, Y0) \tag{3.14}$$

diffudua is the function calculating the difference $U_d - U_a$, and Y is the final geomtry. The function lsqnonlin solves the problem with a nonlinear least squares algorithm. It is possible to choose betweeen a Gauss-Newton method and a Levenberg-Marquardt (LM) method in the optimization process. After a lot of trial and error, we found that the LM method gave the best results. A documentation of the method and its implementation into lsqnonlin is outlined in [6]. The method is found to work very well for finding an aft hull geomtry with Stratford flow velocity distribution. It did not work so well when we wanted to find a whole body, say an ellipse with a known velocity distribution.

Another method was also tested. Instead of directly varying the offset value Y_n in the optimization rutine, we made a B-spline of the initial body, and varied the coefficients in the B-spline. The coefficients in the B-spline describes a body geometry, and the actual velocity distribution were calculated and compared with the prescibed velocity distribution. This is equal to the method above, but the difference is that we describe the body with a B-spline, and varies the coefficients in the spline to find the wanted body geometry. This method did not work well when we wanted to find an aft hull geomtry with Stratford flow velocity distribution. It did not converge to the PVD. On the other side it worked much better than the former method when optimizing a whole body, for instance an ellipse as in fig. 3.7. The dotted lines are initial

geometry and velocity. The solid-drawn line are exact goemetry and velocity, and final geomety and velocity. The exact and final geometries correspond very well, in the figure they plot on top of each other. The geometry is divided into 100 elements, and the calculation converged after 9 iterations.

In fig. 3.8 we have designed a body with a large region of constant velocity with this inverse method. We see that the flow velocity for the final body corresponds very well to the desired flow velocity.

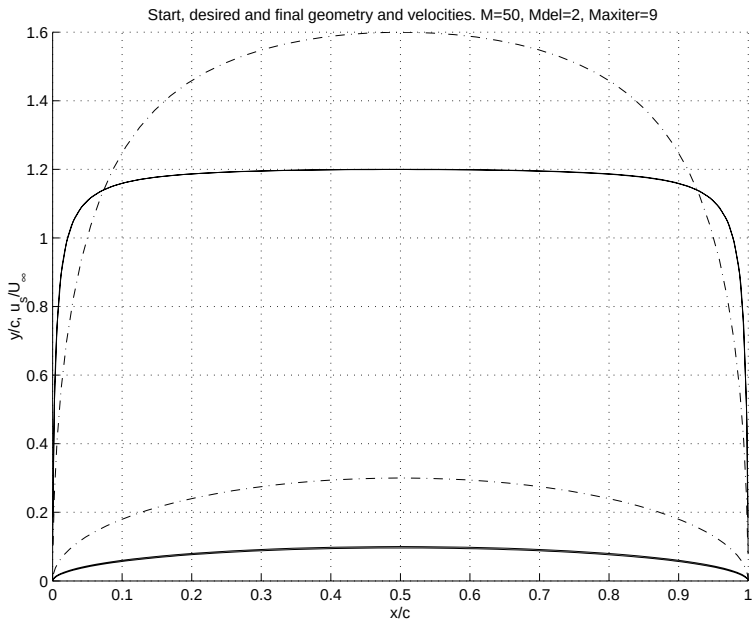

Figure 3.7: *Inverse design of ellipse. See text for details.*

3.3.1 Implementation of the Stratford distribution on 2D profiles

The fore part of the profiles are kept fixed, while we optimize the aft part to give us a region with Stratford velocity distribution. As an initial aft profile we use

$$\frac{y(x)}{T} = \frac{1 - \left(\frac{x-b}{L-b}\right)^m}{1 + \left(\frac{x-b}{L-b}\right)^m} \tag{3.15}$$

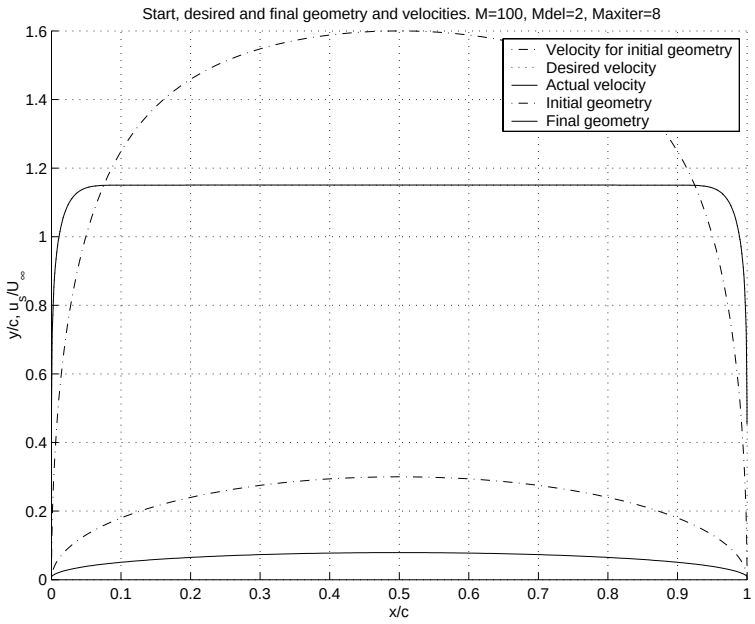

Figure 3.8: *Inverse design of a 2D body with a large region of constant velocity.*

Where T is half of maximum thickness of profile, x is length from bow, b is the starting point of Stratford distribution along the profile length, and n is a parameter controlling the curvature of the aft shoulder. Larger m increases the curvature, and thereby decreases the maximum velocity over the shoulder U_0, see fig. 3.10. The peak velocity U_0 from the calculations from the initial profile is input velocity in the Stratford distribution shown by dotted lines in the figure. The peak velocity U_0 for the initial profile will converge to a finite velocity for all values of m of practical interest for us. We have used $m = 1.25$ for both profiles. The calculations are done with decreasing element length around the aft shoulder, and the number of elements increased until the value of U_0 converged.

A profile with the shown Stratford distribution gives a very sharp peak velocity on the aft shoulder, see fig. 3.10. This peak velocity will in theory trigger the "almost separating" Stratford flow along the aft part of the profile. If this peak velocity is smoothed then the flow over the shoulder will be more conservative with respect to separation. There still will be a relatively large area with Stratford flow. This gives a smoother flow, and will not destroy the Stratford flow in the aft part radically. The smoothing of the flow is shown for the final geometries in fig. 3.14 and in figs. 3.15 and 3.17. In the inverse

design procedure we also set the exit angle of the profile in the transom. The region of optimization is then from a small distance in front of the aft shoulder until a small distance from the transom, for instance 5% from transom. The remaining profile was interpolated by a spline interpolation with the given exit angle at the transom. This spline interpolation was done for every iteration cycle.

In fig. 3.9 is a sketch of the design parameters in the optimization procedure. We set the exit angle for the profile and start of aft shoulder. The curvature of aft shoulder is given by the smoothing of the PVD over the shoulder, while the maximum slant angle is indirectly a result of the parameter β.

After the last iteration, the whole profile was smoothed with a smoothing function. In figs. 3.16 and 3.18 we see the final aft hull geometry in the upper plot. The slope of the profile is shown in the middle plot. In that plot we also see the range of optimization region, and the exit angle, $\arctan(dy/dx) = \arctan(-0.0524) = -3^\circ$ for Mod B.

The whole inverse design procedure was a fine tuning of values of m, b and Rn (or β) which gave a 2D profile which converged to the desired velocity distribution. This was a long and laborious process for each profile. Profile Mod A and Mod B is optimized with respectively $Rn = 7.28{*}10^6$ and $Rn = 40{*}10^6$. We also could have used β as the varying parameter in the optimization process instead of Rn.

As mentioned in sec. 2.2.3, the Stratford distribution is only a weak function of Rn, and the profiles will be conservative for larger Rn than the design Rn. The wind tunnel tests in the next chapter are done with $Rn = 4 * 10^6$ and $Rn = 6 * 10^6$. The towing tank tests are done with $Rn = 4 * 10^6 - 16 * 10^6$. That means for Mod A the design Rn is like the Rn in the model tests. For Mod B we have chosen a more radical design, and use a considerably larger Rn for design. This should give separation during model tests. But due to the fact that we have smoothed the aft shoulder for a more useful and practical design, the peak velocity is reduced, and the trigging of the separation after the shoulder is reduced. This means we can increase the design Rn and avoid separation for lower Rn. The greater region of the pressure recovery is still with Stratford velocity distribution.

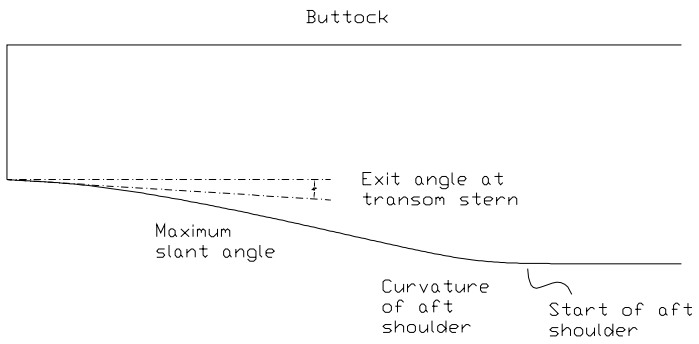

Figure 3.9: *Aft hull seen from starbord side. Design parameters of the hull: exit angle, slant angle, curvature and start of aft shoulder.*

3.3.2 Performance of the method

The numerical performance and accuracy of the inverse method is determined by iteration convergence and grid convergence. The iteration convergence is checked by comparing the AVD and the PVD from the iterated geometry.

To see if our inverse method is grid convergent, we doubled the number of grid points, and repeated the computation. Fig. 3.12 shows computed aft profile for Mod A with M=400, while figs. 3.15 and 3.16 shows the same, but with M=200. The calculations with M=200 is used as base for design of Mod A, and we see that by doubling the number of grid points, we still get the same profile. This shows that our inverse method converges both due to iteration and due to grid sensitivity.

Table 3.1 shows the iteration history of convergence of the profile shown in figs. 3.11 and 3.12. The residual is the RMS of the difference between AVD and PVD. The function count means that the funtion calculating the difference in AVD and PVD is called up this number of times for every iteration procedure in the optimization function.

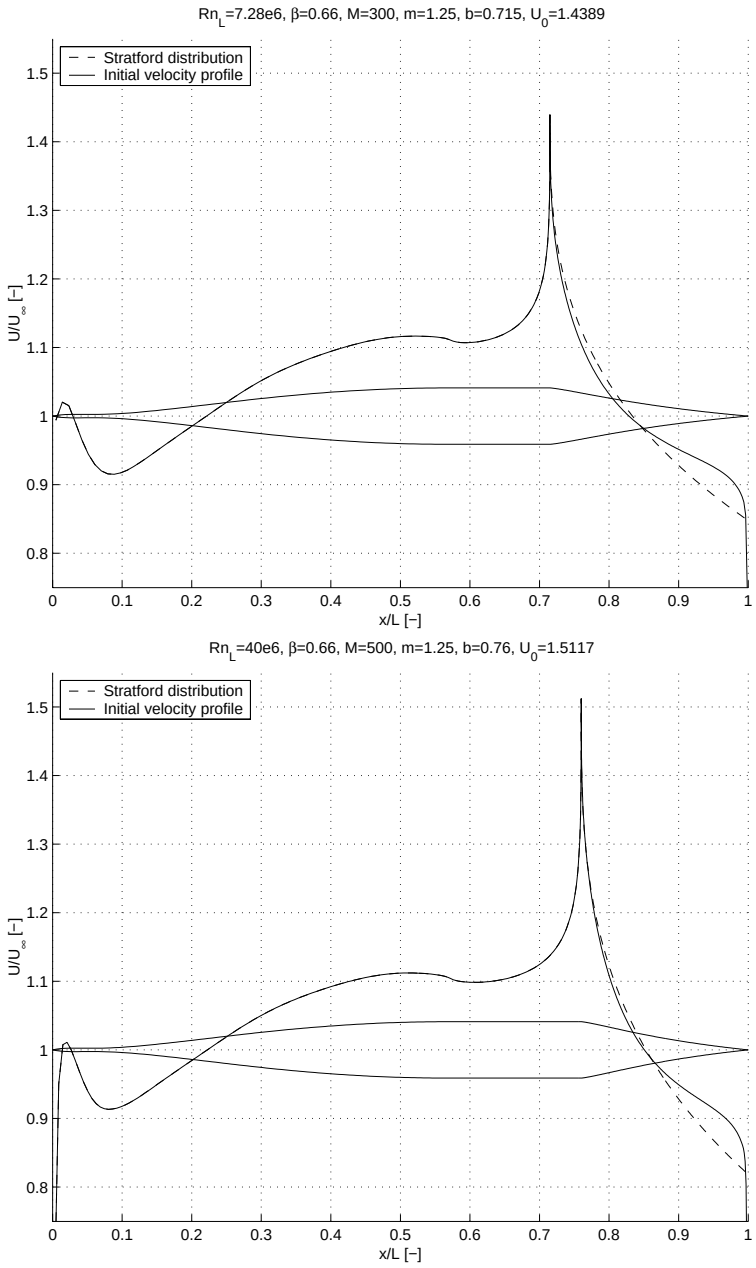

Figure 3.10: *Top: Mod A. Bottom: Mod B. Initial geometry and velocity for 2D profile together with Stratford distribution tailored for these initial profiles.*

	M=200		M=400	
Iter	Func-count	Residual	Func-count	Residual
1	61	0.0395	122	0.0724
2	126	0.009487	248	0.0669
3	191	$3.18*10^{-06}$	374	0.000475
4	256	$2.33*10^{-12}$	500	$2.75*10^{-07}$
5			626	$1.79*10^{-09}$
6			752	$5.91*10^{-13}$

Table 3.1: *Iteration history of convergence of profile shown in figs. 3.11 and 3.12.*

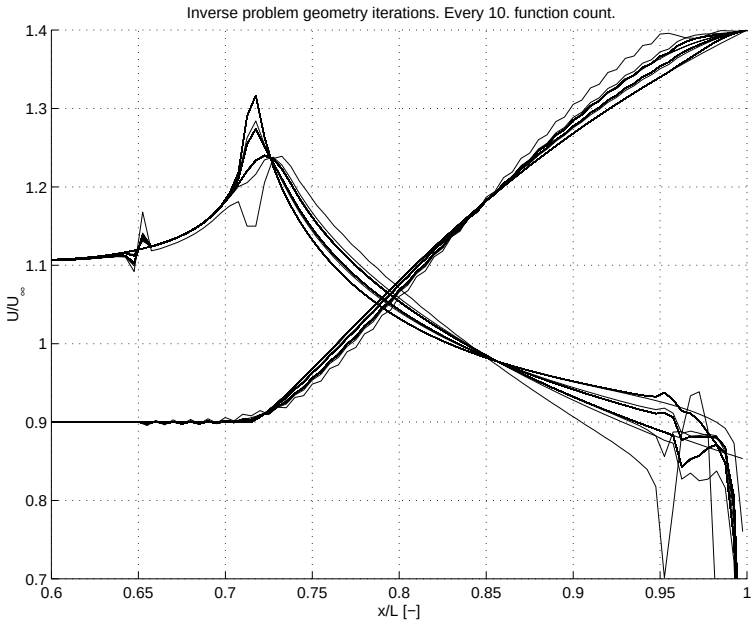

Figure 3.11: *Geometry iterations for profile Mod A. M=200. Residual for final difference in AVD and PVD* $< 10^{-10}$. *The extent of the iteration is from* $x/L = 0.65$ *to* $x/L = 0.95$.

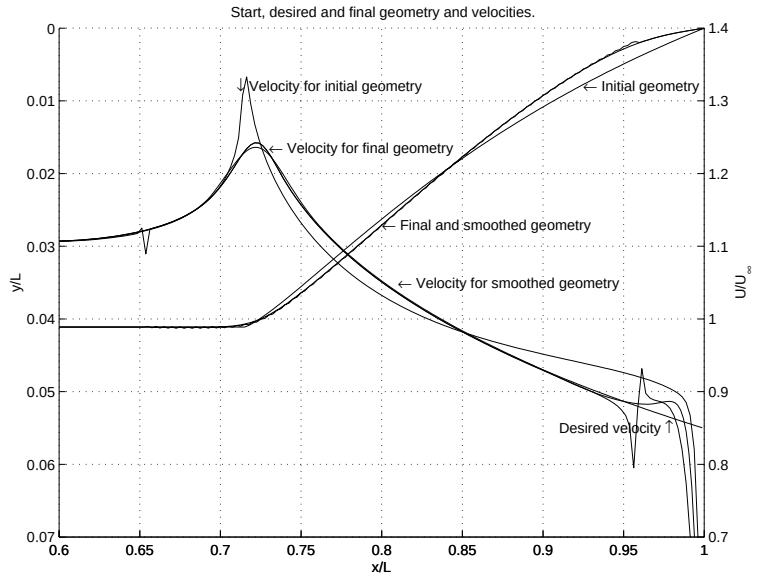

Figure 3.12: *Calculated aft hull design. M=400*

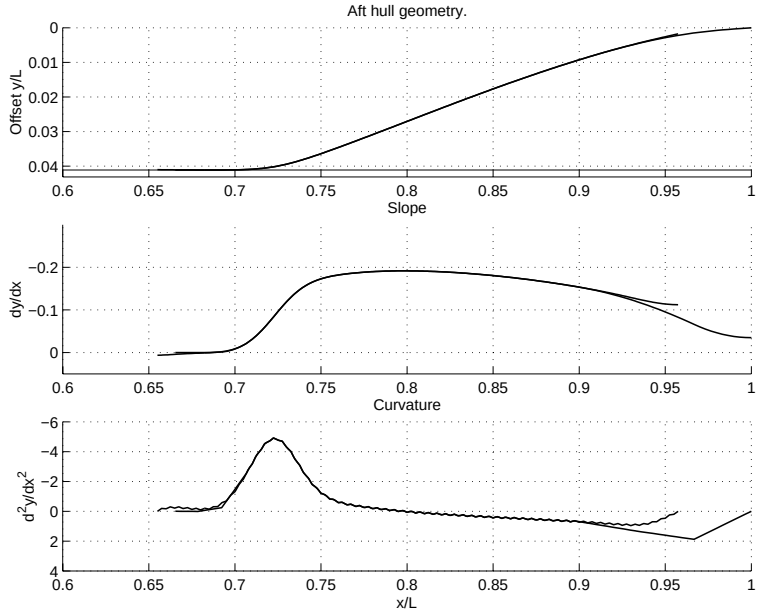

Figure 3.13: *Mod A. Offset values at the aft part of 2D profile, together with slope and curvature for 2D profile. M=400*

3.4 Calculated 2D profiles with Stratford velocity distribution

In this section we show the calculated 2D profiles, calculated from the inverse procedure presented in section 3.3. The detailed iteration history together with profile before and after smoothing is shown in fig. 3.15 for Mod A, and in fig. 3.17 for Mod B. The effect of smooting the profiles on slope and curvature on aft part of profile itself is shown in figs. 3.16 and 3.17. We see that the curvature of the inverse designed aft profile has a waviness. This calculation is done with 200 elements. With a higher number of elements, this waviness gets smaller and smaller, see fig. 3.13 which has 400 elements.

In fig. 3.14 the final smoothed geometry of Mod A and Mod B designed with a Stratford tail is shown. The bodies are designed with the inverse method from eqn. (3.14). The fore part of the body is corresponding to the sectional area curve (SAC) of the ship P-1211 which is the parent hull form used in this study, and only the aft part of the ship is changed on Mod A and Mod B.

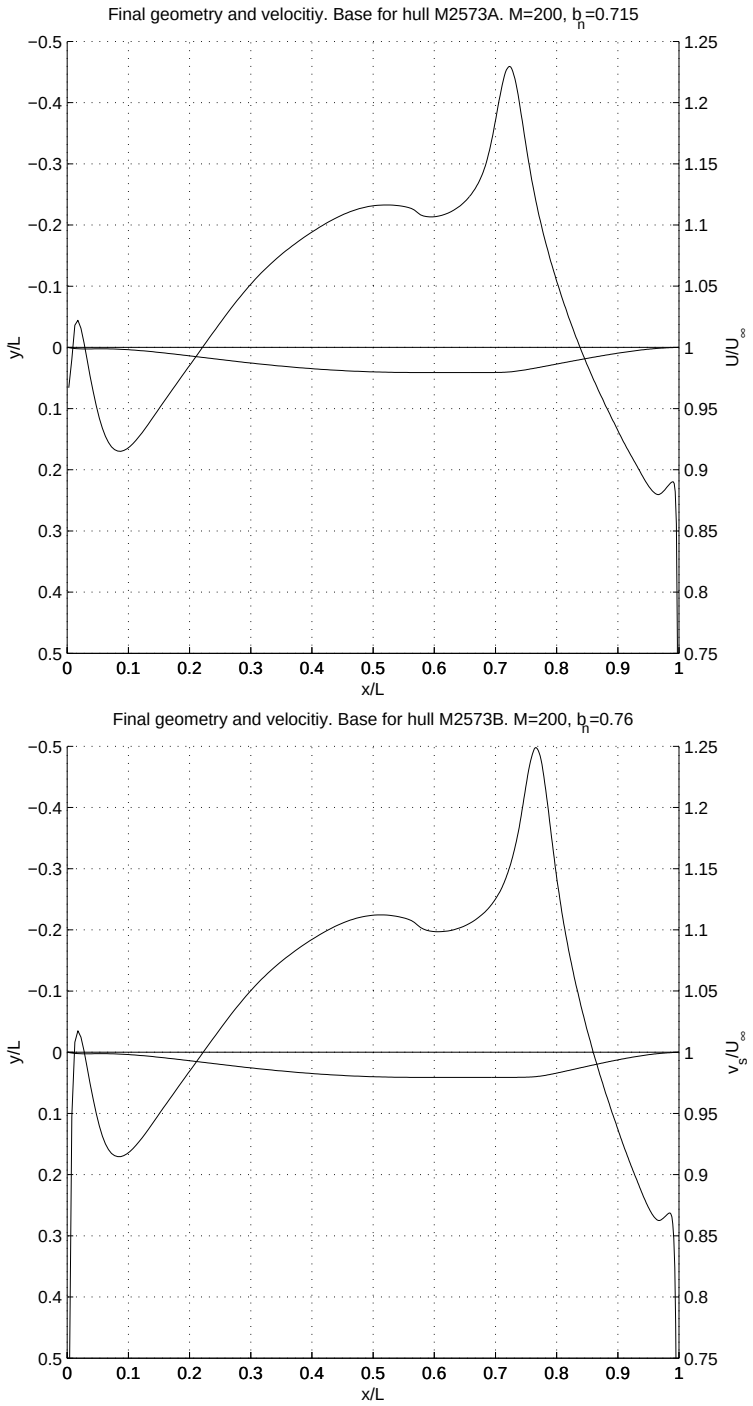

Figure 3.14: *2D tail design which is base for Mod A (top figure) and Mod B (bottom figure). Flow velocity for 2D profile shown. M=200.*

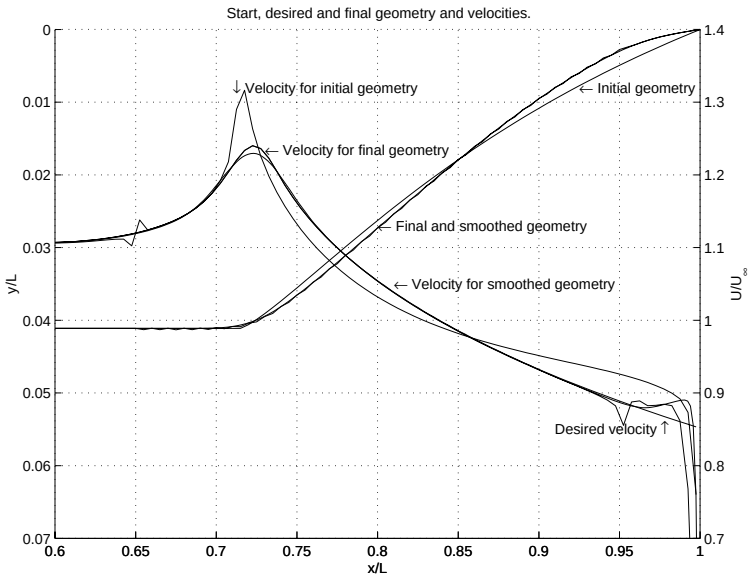

Figure 3.15: *Calculated aft hull design of Mod A from iteration procedure. M=200.*

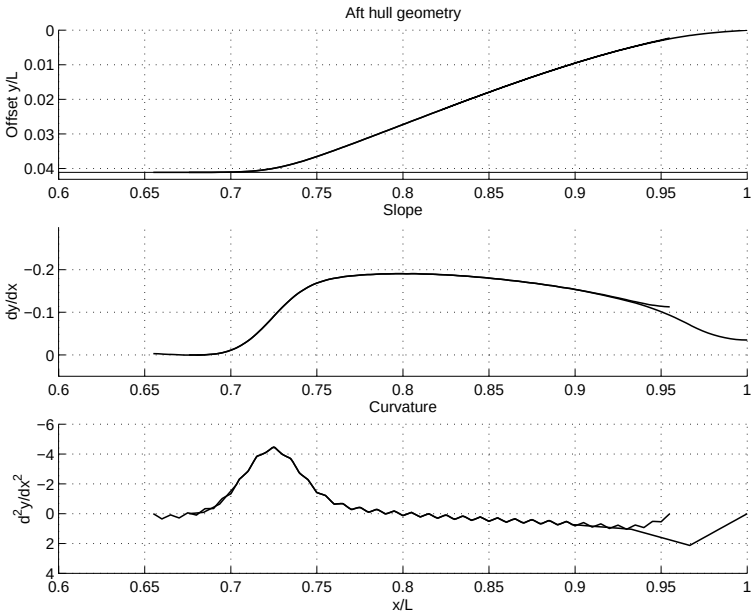

Figure 3.16: *2D tail design which is base for Mod A. Offset values at the aft part of 2D profile, together with slope and curvature for 2D profile. M=200.*

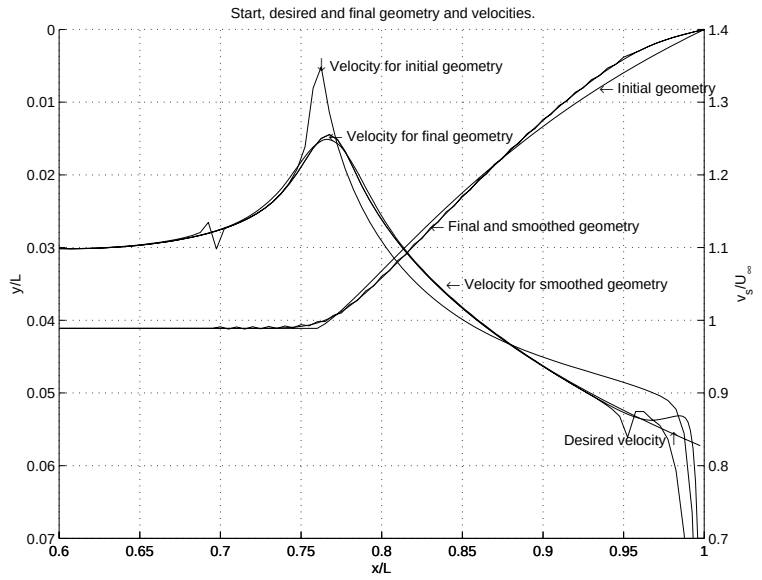

Figure 3.17: *Calculated aft hull design of Mod B from iteration procedure. M=200.*

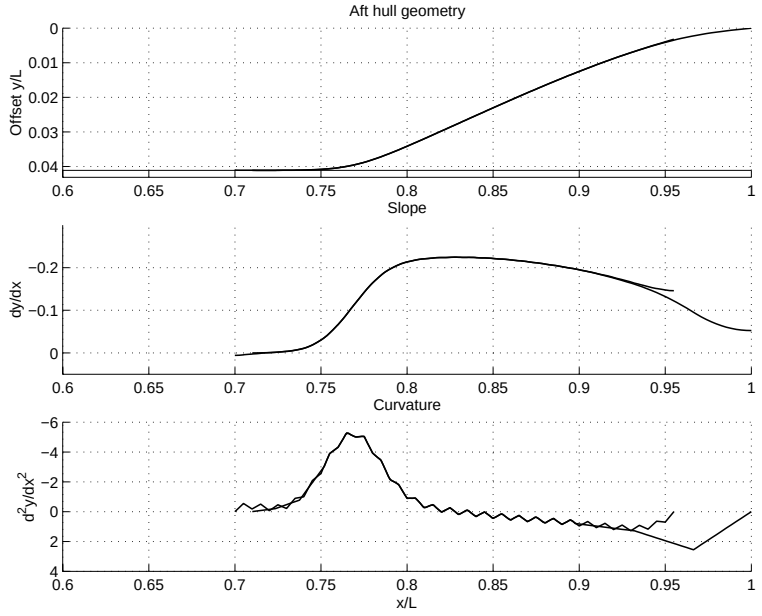

Figure 3.18: *2D tail design which is base for Mod B. Offset values at the aft part of 2D profile, together with slope and curvature for 2D profile. M=200.*

3.5 Design of 3D ship hulls from 2D profiles

In this section we will give a description of the design procedure from 2D profiles to 3D ship hulls.

3.5.1 Outline of design procedure

In sec. 3.3 we presented the inverse design method which is developed. This method is now used to optimize the aft part of a given ship hull. In sec. 3.4 we found the 2D profiles which make up the centerline of the new hulls. A schematic outline of the design procedure is given in fig. 3.19. We start with the parent hull form, calculate the sectional area curve (SAC) of the ship, and this SAC curve forms a 2D initial profile. The aft part of this initial profile is shaped with the inverse design procedure to match a given prescribed velocity distribution on the aft part of the hull. Further, this optimized aft part will form the centerline buttock of the new ship, as shown in fig. 3.19. The midship section is kept and a bilge radius formed for the new aft part of the hull.

Matheson and Joubert [22] and [23] measured local pressure coefficient and local skin friction around stations on ship forms in a wind tunnel. They found that the measured skin friction on the ship bottom in the midship range very much follows the Schoenherr skin friction for a flat plate. This indicates that the flow on the bottom of this kind of ships are more or less 2D. We have therefore used 2D profiles to optimize aft part of typically pram type ships. The hypothesis is that since the flow on the bottom of ships are close to 2D, we can use a 2D profile to build up the aft part of a pram type ship. This hypothesis is verified experimentally in the next section where we show the 2D profile of the flow around the ship hulls.

The best would of course be to have a full 3D flow calculation around the ship hull, and to do this optimization 3D. This requires a lot of data power and much more work on the optimization method. This would be the next step. This 2D method shows that an optimization method like this is easy to use and gives satisfactory results.

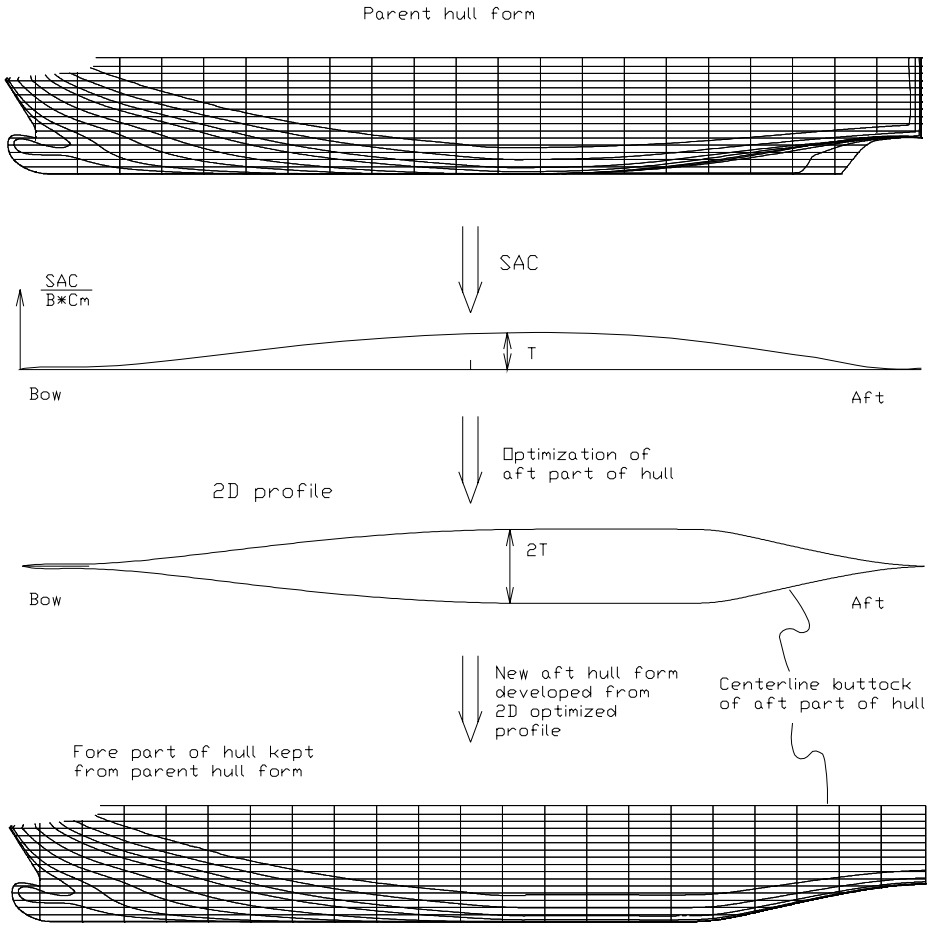

Figure 3.19: *Schematic flow diagram of design procedure.*

3.5.2 Drawings and data of ship hulls

Table 3.2 shows the ship data for Mod A, Mod B and parent hull P-1211. The three following figures show lines drawings of the designed ships Mod A and Mod B, and the parent ship P-1211.

	Symbol	Unit	P-1211 Parent	Mod A	Mod B
Length overall	LOA	[m]	127.76	127.76	127.76
Length betw. perp.	LPP	[m]	117.3	117.3	117.3
Breadth moulded	B	[m]	21	21	21
Depth to 1st deck	D	[m]	16.948	16.2	16.2
Draught at LPP/2	T	[m]	5.296	5.296	5.296
Draught at FP	TFP	[m]	5.296	5.296	5.296
Draught at AP	TAP	[m]	5.296	5.296	5.296
Trim (pos. aft)	t	[m]	0	0	0
Rake of keel		[m]	0	0	0
Rise of floor		[m]	0	0	0
Length on waterline	LWL	[m]	126.843	126.848	126.848
Breadth waterline	BWL	[m]	21	21	21
Volume displacement	∇	[m^3]	7860.9	8073.2	8409.2
Displacement	D	[t]	8097.7	8316.4	8662.6
Prismatic coefficient*	CP	[-]	0.6403	0.6577	0.685
Block coefficient*	CB	[-]	0.6026	0.6188	0.6446
Midship section coefficient	CM	[-]	0.941	0.941	0.941
Longit. C.B. from LPP/2	LCB	[m]	-3.637	-4.253	-5.784
Longit. C.B. from LPP/2*	LCB	[% LPP]	-3.101	-3.626	-4.931
Longit. C.B. from AP	LCB	[m]	55.013	54.397	52.866
Vertical C.B.	VCB	[m]	3.088	3.048	3.014
Wetted surface	S	[m2]	2944.08	2847.71	2882.78
Wetted surf. of trans. stern	AT	[m2]	0	0	0
Waterplane area	AW	[m2]	2213.87	2185.45	2192.97
Waterplane area coefficient	CW	[-]	0.831	0.82	0.823
Longit. C.F. from LPP/2	LCF	[m]	-10.506	-9.836	-9.998
Longit. C.F. from AP	LCF	[m]	48.144	48.814	48.652
Immersion	DP1	[t/cm]	22.692	22.401	22.478
Trim moment	MT1	[t·m/cm]	204.994	195.161	194.163
Transv. metac. above keel	KMT	[m]	12.306	11.851	11.586
Longit. metac. above keel	KML	[m]	298.432	276.645	264.232

Table 3.2: *Data for ships*

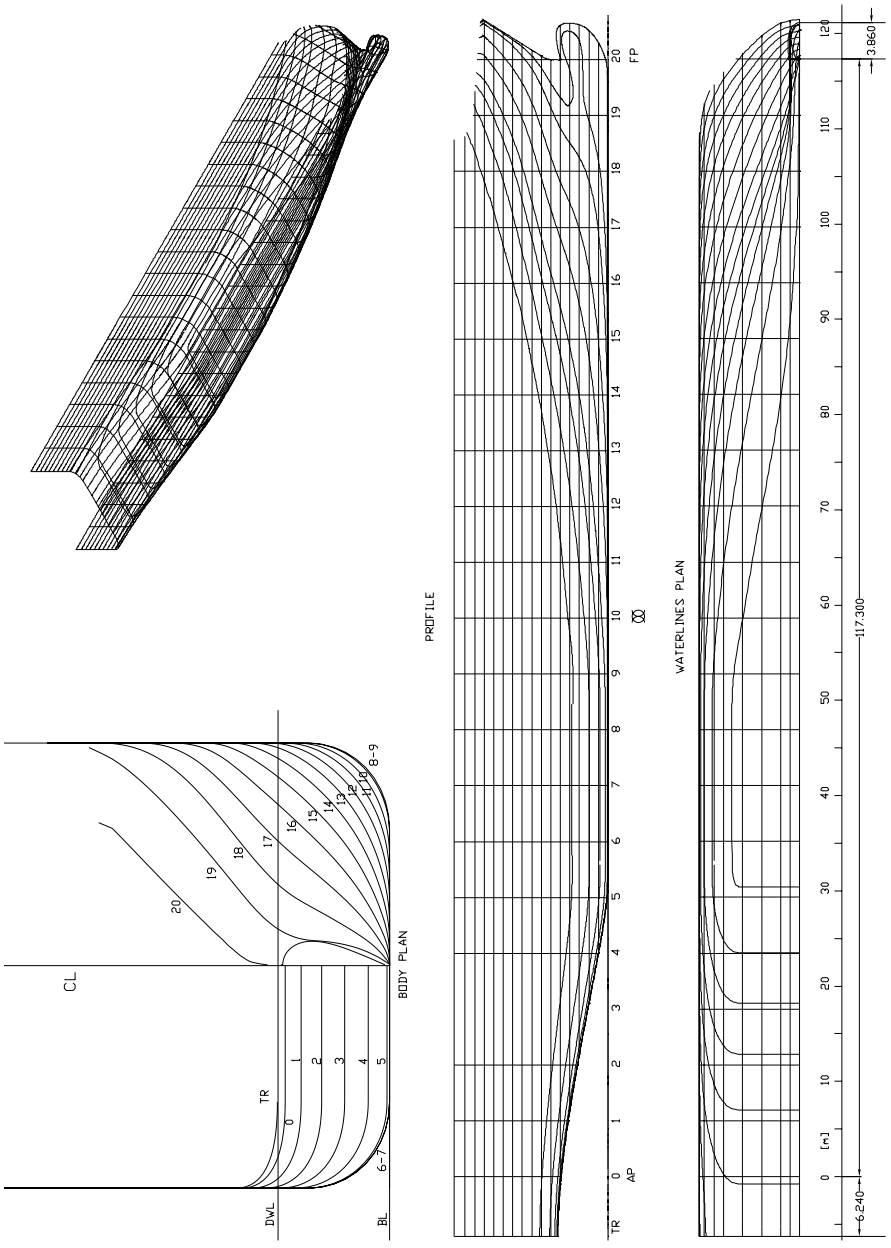

Figure 3.20: *Body, profile and plan of Mod A.*

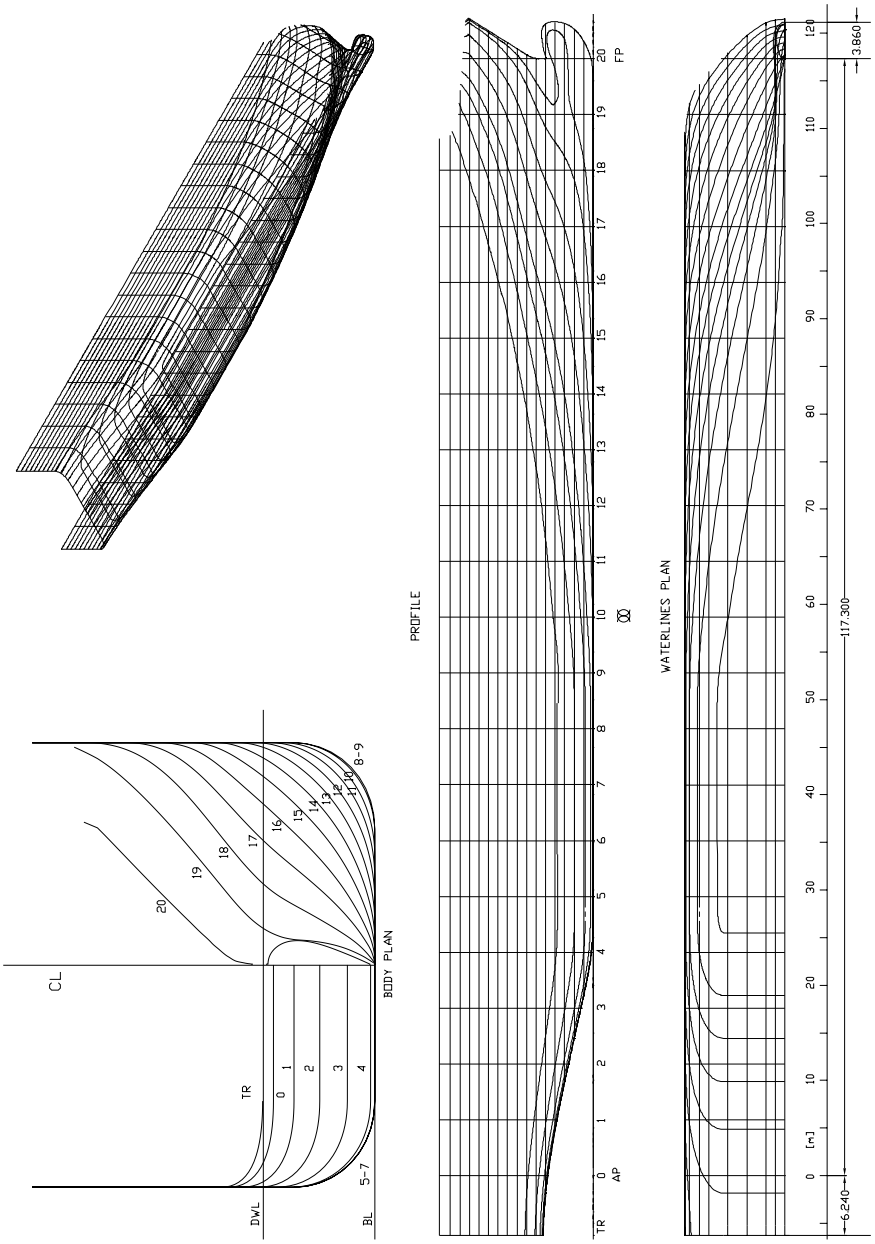

Figure 3.21: *Body, profile and plan of Mod B.*

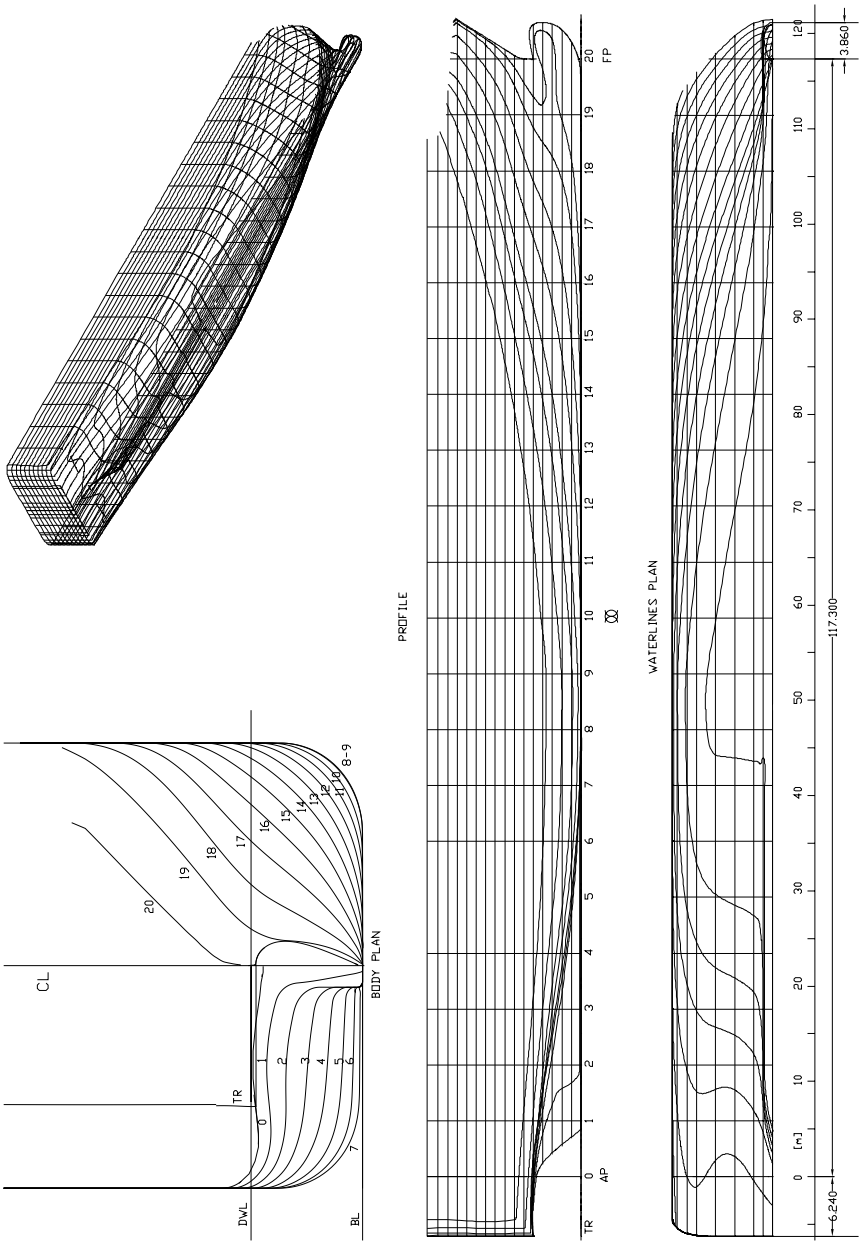

Figure 3.22: *Body, profile and plan of parent ship, P-1211.*

Chapter 4

Model test results

This chapter deals with the experimental verification of the calculated ship models in the former chapter. In section 4.1 we go into the detailed boundary layer flow of the ship models. The tests are performed in a wind tunnel. We measure the boundary layer profile, and calculate boundary layer properties from these measurements. In section 4.2 one of the two ship models (Mod B) are tested in a towing tank. These tests will show if our inverse designed ship models will perform in a basically sound way.

4.1 Results from wind tunnel

4.1.1 Experimental setup and measurement procedures

The models

A sketch of the body geometries used in this study is shown in figures 4.1 and 4.2. Both models are fastened upside-down to the floor in the wind tunnel. The models are made of divinycell foam plastics glued to a plywood plate. The models were machined to the desired shape in a CNC milling machine. Thereafter they were covered with polyester and sanded to the desired smoothness. The models were sprayed with black paint. When they were finished, the holes for pressure ports were drilled and copper tubes with an inner diameter of 1 mm were installed flush with the hull surface. Thin nylon tubes connected the ports on the hull with the pressure transducer.

The model scale is 1:47.2. The length of the models are 2.73m. The models are identical in the fore part of the ship up to mid ship. Mod A has a longer run from aft shoulder to transom stern than Mod B.

The models are fitted with a 10 mm broad strip of sand glued to the model for turbulence trigging. The sand has a grain size of approximately 700μm. The strip of sand is placed 5% of model length (137mm) downstream from the tip of the bow.

The error in the geometry of the finished models are shown in fig. 4.3. The models were put upside-down with the design waterline flush on an accurately flat lofting table. We then measured the draught at stations forwards of AP and until midship. The measuring equipment had an accuracy of less than 0.01mm, that means about 0.01% relative error when measuring midships, and about 0.1% when measuring at AP. From fig. 4.3 we see that the relative error in geometry is in the order of 0.5 to 1% at all the measured points, except the station at AP. The error from one point to the neighboring point is also about 0.5%.

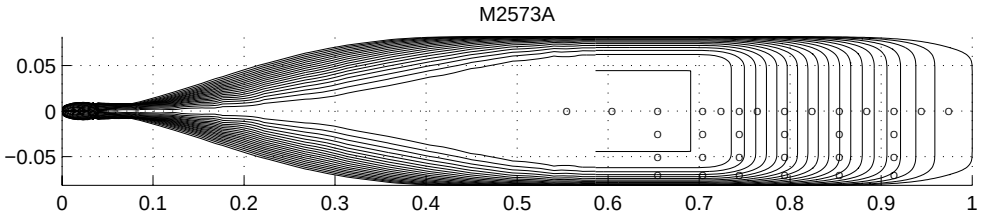

Figure 4.1: *Waterlines of model Mod A with ports for static pressure measurement indicated. The figure is dimensionless with respect to total length of model.*

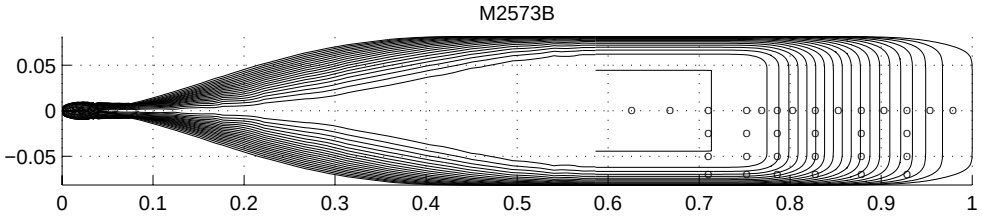

Figure 4.2: *Waterlines of model Mod B with ports for static pressure measurement indicated. The figure is dimensionless with respect to total length of model.*

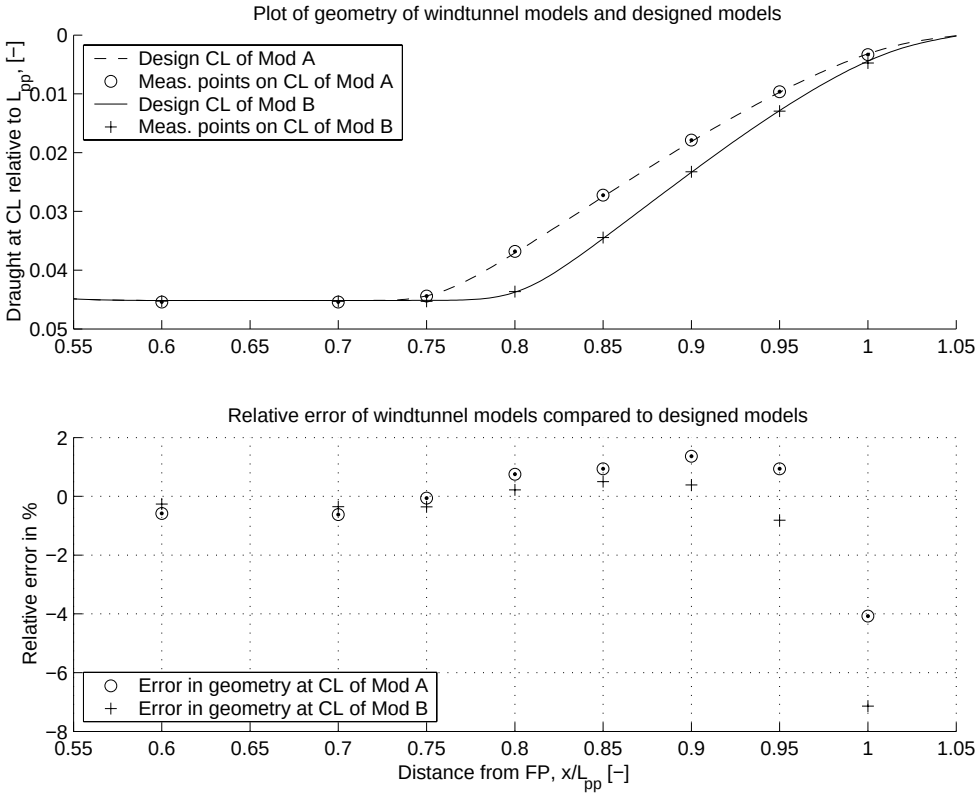

Figure 4.3: *The top figure shows design buttock lines together with measured draught on wind tunnel models. The bottom figure shows the relative error in geometry between design and real models.*

4.1.2 The flow facility and measurement techniques

Description of the wind tunnel The tunnel is located at Institutt for mekanikk, termo- og fluidmekanikk at NTNU in Trondheim. The tunnel is of the closed return type and the 1.0 x 0.5m test section extends 7m downstream of the contraction. The maximum free stream velocity in the test section is about 40m/s. With the ship models in the tunnel, we achieved a maximum velocity of about 32m/s which gave a Reynolds number of $6 * 10^6$ with respect to model length.

The tunnel is of the closed return type, and a sketch of the tunnel is shown i fig. 4.4. The air is propelled round the circuit by a power driven fan. The fan is turning with constant RPM, and the flow velocity in the tunnel is varied by pitching the fan vanes.

In every corner of the tunnel there are turning vanes which helps the air deflect at right angles. The tunnel also has a honeycomb whose function is to smooth the flow and break up large eddies.

The heat exchanger is located in the upstream corner of the entrance section as shown in fig. 4.4. During the tests it was possible to manually adjust the amount of water passing through the heat exchanger, to achieve a constant temperature in the tunnel.

The free stream turbulence level has been measured by Sætran, [29]. The longitudial normal stress component $\overline{u'^2}$ was measured with a single hot-wire at the centerline of the test section, 105mm above the bottom plate and 1570mm downstream of the inlet of the test section. Table 4.1 shows the longitudinal turbulence intensity as a function of test section velocity.

The turbulence level presented in table 4.1 fits in a classification which is regarded as "moderate stream turbulence level". This level of turbulence is acceptable for our measurements.

Mean velocity $\overline{U}$ m/s	15.7	22.5	25.1	28.3	32.5
Turbulence intensity $\sqrt{\overline{u'^2}}/\overline{U}$ %	0.38	0.32	0.33	0.31	0.34

Table 4.1: *Turbulence intensity in wind tunnel as function of freestream velocity.*

Most of the experiments were done at a free-stream velocity of about 22m/s, and the rest at 32m/s.

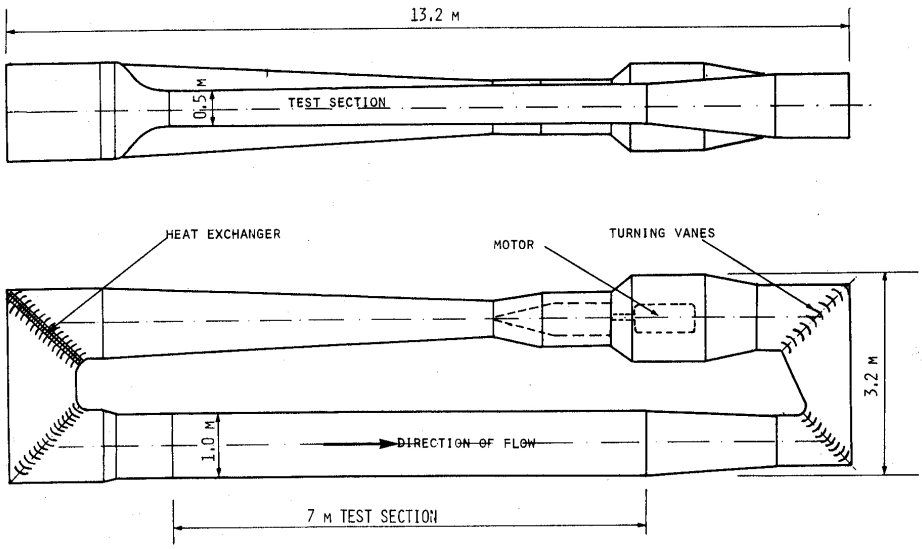

Figure 4.4: *General arrangement of wind tunnel.*

Measurement techniques and equipment The free stream velocity was measured with a pitot tube located at the start of the test section.

The pressure differences were measured with differential pressure transducer with a characteristic of 61.4 Pa/V, see fig. 4.6. The transducers were linear up to a pressure difference of approximately 600Pa, which is about 32m/s. For higher flow velocities a pressure transducer with a characteristic of 1647.8Pa/V were used. This transducer was linear far beyond the pressure differences obtained in this study.

The local static pressures on the ship hulls were measured as a pressure difference between the static pressure in the free stream pitot tube and a port in the ship hull on the actual location.

The boundary layer velocity were measured with pitot tubes measuring only dynamic pressure. The outer diameter of the tube was 1.0mm. The pressure tube was moved normal to the ship surface through the boundary layer, with a traversing unit. The unit could be traversed with an accuracy of less than 0.01mm, and was moved manually.

The static pressure in the boundary layer were measured using the pressure port on the ship hull surface on the actual location. This gave insignificant

error for measurements on locations with small or no curvature. On locations with curvature we measured static pressure in the boundary layer, and the results were compared, see the paragraph "Measurement errors" in the last part of this section.

A laptop PC with a self-made Labview data collecting program was used for logging the data and saving to files, see fig. 4.5.

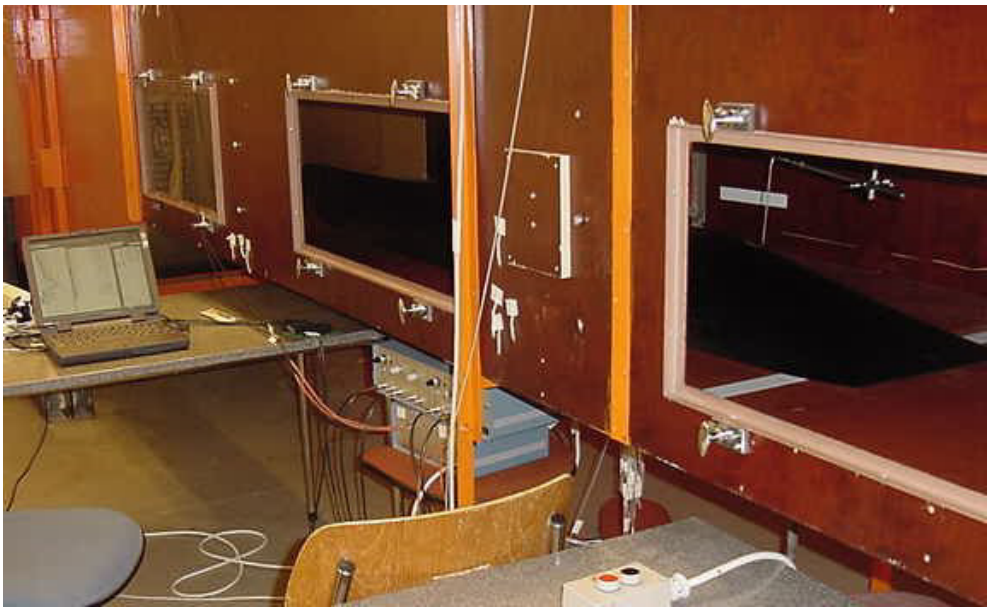

Figure 4.5: *A picture of the wind tunnel with a ship model on the floor inside the tunnel. Pressure transducers, amplifier and data logging equipment is seen by the table.*

4.1.3 Static pressure measurements

The measurements are done on both hulls, Mod A and Mod B. On model Mod A the measurements were done at $Rn = 4 * 10^6$, and for Mod B with both $Rn = 4 * 10^6$ and $Rn = 6 * 10^6$. The results with the two different Rn did not show any significant difference on the static pressures. It is obvious that the difference in Rn is too small to give any information about the Rn dependency of the flow. On the other hand, it is very convincing that the results for the two independent measurements are close to identical.

The static pressure measurements are done by measuring the pressure difference between the static free-stream pressure and local static pressure at the pressure ports. This pressure difference is divided with the pressure difference between stagnation and static pressure for the free-stream pitot tube to achieve the pressure coefficient for the given pressure port.

$$C_p = \frac{p_{local} - p_{stat}}{p_{stag} - p_{stat}} = \frac{\Delta V_{loc-stat} * C_2}{\Delta V_{stag-stat} * C_1} \tag{4.1}$$

where $\Delta V_{loc-stat}$ and $\Delta V_{stag-stat}$ is the measured voltage difference with pressure transducers. This voltage difference is measured between the given pressures with respectively pressure transducer nr. 2 and transducer nr. 1. These have calibration factors C_2 and C_1.

The ports for static pressure measurements are located on the ship models as given in the table below and in figs 4.1 and 4.2. There are one row of ports along centerline of the model. The pressure measurements here are used to compare with calculations and the results from the inverse program.

Further are the transverse ports used to see the 2D structure of the flow transversally on the hull, and if there are any longitudinal vortices forming. The transverse row of ports are located at port nr 110, 100, 80, 60, 40 and 20, see table 4.2.

	Mod A		Mod B	
Port	Distance	Distance	Distance	Distance
nr	from bulb	from FP	from bulb	from FP
	x/L_{tot}	x/L_{pp}	x/L_{tot}	x/L_{pp}
130	0.55	0.565	0.622	0.642
120	0.6	0.619	0.664	0.688
110	0.65	0.673	0.706	0.734
100	0.7	0.727	0.748	0.779
90	0.72	0.749	0.765	0.798
80	0.74	0.771	0.782	0.816
70	0.76	0.792	0.798	0.834
60	0.79	0.825	0.824	0.862
50	0.82	0.858	0.849	0.889
40	0.85	0.89	0.874	0.916
30	0.88	0.923	0.899	0.944
20	0.91	0.955	0.924	0.971
10	0.94	0.988	0.95	0.998

Table 4.2: *Location of pressure ports for static pressure measurements.*

In figure 4.7 we see the pressure distribution on centerline of Mod A. The

2D calculated pressure distribution is given to compare with the measured pressures.
The total pressure distribution on the hull with centerline and transversal pressures is shown in fig. 4.8. We see that for the first three row of ports, which is before and on the aft shoulder, the C_p values rise from centerline and to the side of ship. This means there is an acceleration of the flow over the shoulder. For the next three row of ports the C_p values drop from centerline to side of ship. This means the flow is retarding.
Figs. 4.8 and 4.9 show the same for Mod B. The transversal structure of the flow tells us that it is fairly 2D, that is the flow lines follow the buttocks on the ship hull. Mod B has a little bit more difference in C_p values from centerline to ship side than Mod A, due to its shorter aft part and larger base slant angle. The measurements did not show any Rn dependence, see fig. 4.10.
The relative area blockage A_s/A, of the small tunnel with the model is 10 %. In fig. 4.9 we have compared the pressure distribution along centerline for Mod B in the small tunnel where most of the measurements are done, and the large tunnel. The difference should be the blockage effects for the small tunnel. In fig. 4.11 the relative blockage effect is plotted. We see that the velocity over the aft shoulder is about 7-8 % larger in the small tunnel compared to the large tunnel. Over the midship section, the velocity is 6 % larger.

The blockage effet will be dealt with further at the end of section 4.1.5.

Measurement errors The static pressure measurements were repeated four times with reynolds numbers of $Rn = 4 * 10^6$ and $Rn = 6 * 10^6$, and all tests were independent of each other. The results are shown in fig. 4.9. Calculations of 95 % confidence interval gives a precision error of 6 % of the aft pressure ports, and an error of only 0.5 % of the midship pressure ports. The pressure ports over the shoulder have even less precision error, 0.2 %. The aft pressure ports have a larger relative error due to smaller measured pressure values. We can conclude that the precision error is 0.5% or below for pressure ports from the aft shoulder and forward.

The bias error of the measurements is a function of error in the calibration of the pressure transducer and error in the A/D convertion. The voltage range was +/- 10 V, and a 12 bit resolution gives an error of about 0.05 % if the measured value is about 10 V. The voltage signal output from the pressure transducer was magified so that it was more than 5 V, and normally around 10 V.

The pressure transducers were calibrated with an inclined manometer. The

calibration points are shown in fig. 4.6. We see that the transducers are linear up to about 9 V. The transducer reach the saturation point at 10 V, and we did not use the transducer for signals over 9 V. The error in calibration is due to resolution for the inclined manometer as the readings were done manually. This resolution in reading the vales are 0.2 mm, and as we could incline the manometer to have almost maximum deflection (100 mm) for each measurement, this gave a relative error of about 0.2 %.

The offset was checked and put to zero before each measurement, in case of drift in the electrical equipment. This potential bias error was then eliminated.

Eq. (4.1) gives the relation between the measured values and the pressure cofficient which is presented. From the arguments above, we conclude that the largest contributing factor to the total error of the pressure cofficient will be the errors in the calibration of the transducers. The pressure coefficient is calculated from eq. (4.1). The relative error in pressure coefficient can then be given by

$$\frac{\sigma_{Cp}}{C_p} \approx \sqrt{\left(\frac{\sigma_{C1}}{C_1}\right)^2 + \left(\frac{\sigma_{C2}}{C_2}\right)^2 + (P_{Cp})^2} \tag{4.2}$$

where σ symbolizes errors for the different variables, see eq. (4.1). Further is P_{Cp} the precision error. The total error for the pressure coefficient is then about 0.6 % for pressure ports from the aft shoulder and forward, and the error is up to 6% for the ports most aft.

4.1.4 Measurements of boundary layer velocity

The boundary layer velocity distribution was measured with a pitot tube traversed normally from the hull surface close to a pressure port. A pitot tube measuring only dynamic pressure was used, it had outer diameter of 1 mm. The static pressure was given by the pressure port at the wall. This procedure introduces an error for curved surfaces. Over the shoulder we therefore measured the BL velocity with a pitot-static tube in addition, due to the fact that the static pressure will change from a near-wall position to the edge of BL on a curved surface. When the surface has a small or no curvature, the static pressure is more or less the same throughout the BL. We therefore can use the pressure port at the wall for the static pressure measurements for surfaces with a small curvature. It was a great advantage using the small pitot tube, because we then could measure the BL velocity closer to the wall. This gives a better estimate of the wall friction.

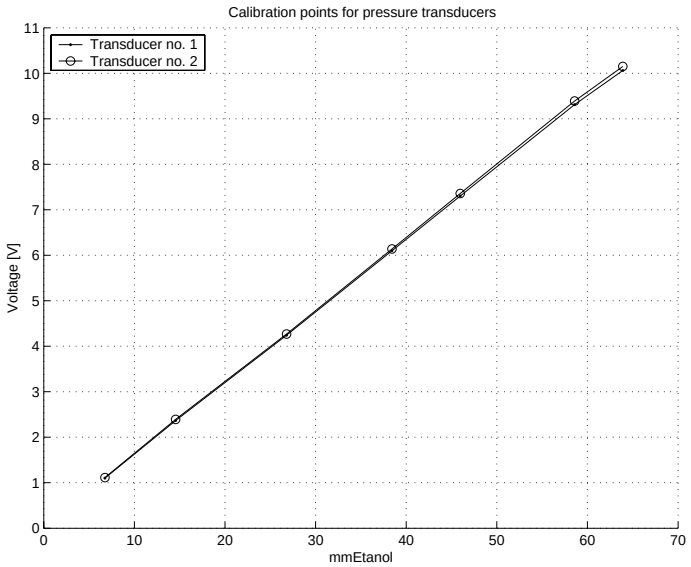

Figure 4.6: *Calibration points for two pressure transducers. The calibration is done with an inclined manometer with etanol.*

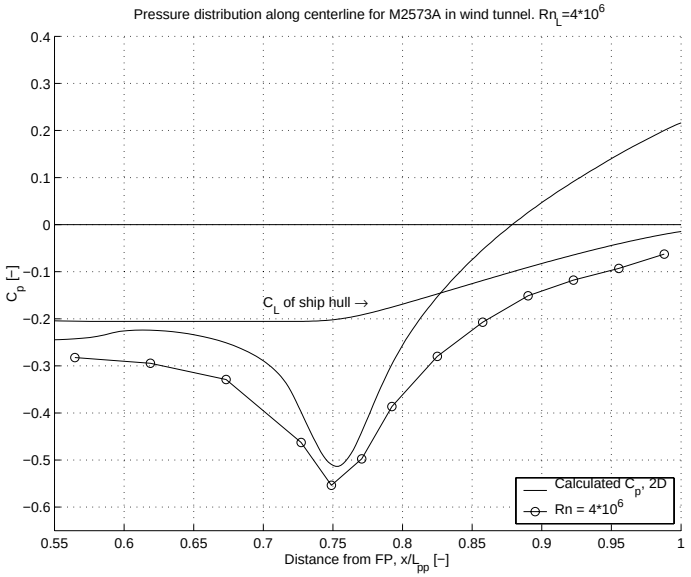

Figure 4.7: *Pressure distribution along centerline for Mod A.*

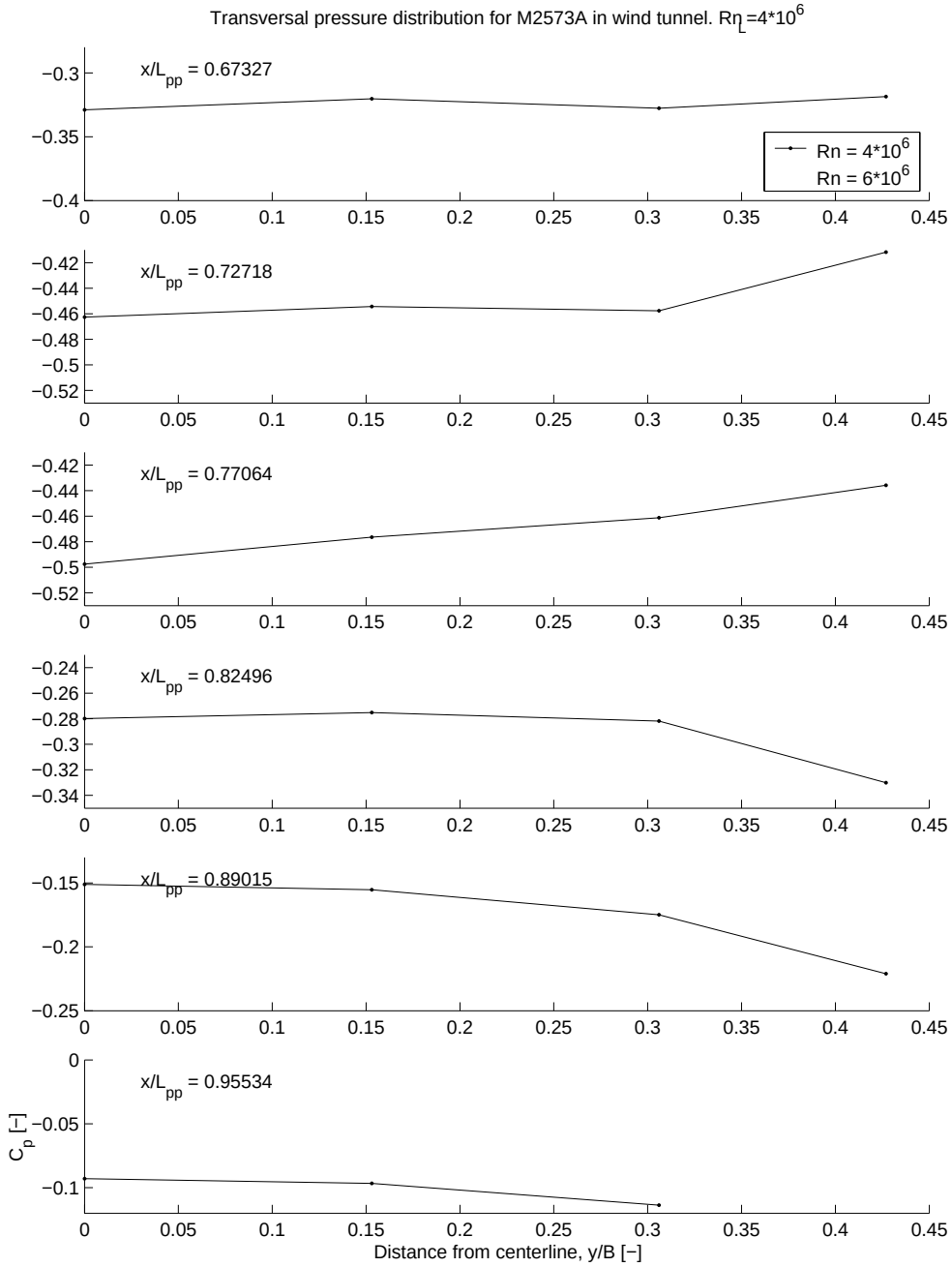

Figure 4.8: *Transversal pressure distribution for Mod A.*

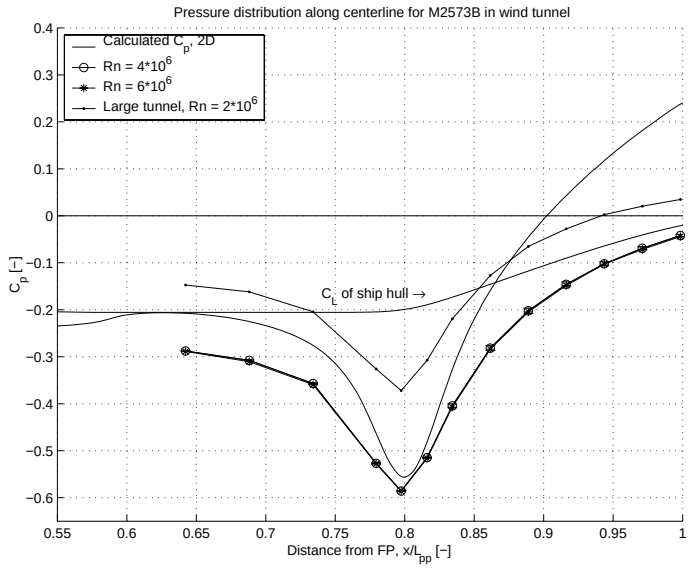

Figure 4.9: *Pressure distribution along centerline for Mod B.*

Mean velocity profiles in the boundary layer are plotted on fig. 4.13 for Mod A and 4.15 for Mod B. The profiles are plotted on four separate plots for more clarity. Plot (a) are the profiles for the flat plate flow on the midship sections upstream of the aft shoulder. Plot (b) shows the profiles over the aft shoulder. Plot (c) are the profiles for the Stratford flow area, and (d) are profiles for the exit area. This applies to both the figs. 4.13 and 4.15. Here U_e is the velocity magnitude at the edge of the boundary layer. The profiles have self similarity on the flat plate flow area (a). On plot (c) in the figures we see that the profiles have a wake component, and even more pronounced in plots (d). As the flow progresses along the profile we appear to achieve self-similarity in the boundary layer flow, see plots (d) in the figures.

Figs. 4.19, 4.20 and 4.21 show streamlines in boundary layer on the plots on top. In the bottom plots we have calculated $\partial u/\partial y$ along the streamlines from the plots on top. In sec. 2.2.2 we were dealing with the derivation of the Stratford velocity distribution. In this derivation from Bernoullis equation we have that $\partial u/\partial y$, see eq. (2.30), along a streamline in the outer layer is constant in a flow with continously zero shear stress at the wall. We have a modified Stratford distribution on both Mod A and Mod B. Mod B has a shorter run, and is therefore closer to the continously zero shear stress run than Mod A. From the bottom plots in figs. 4.19, 4.20 and 4.21 it is very interesting

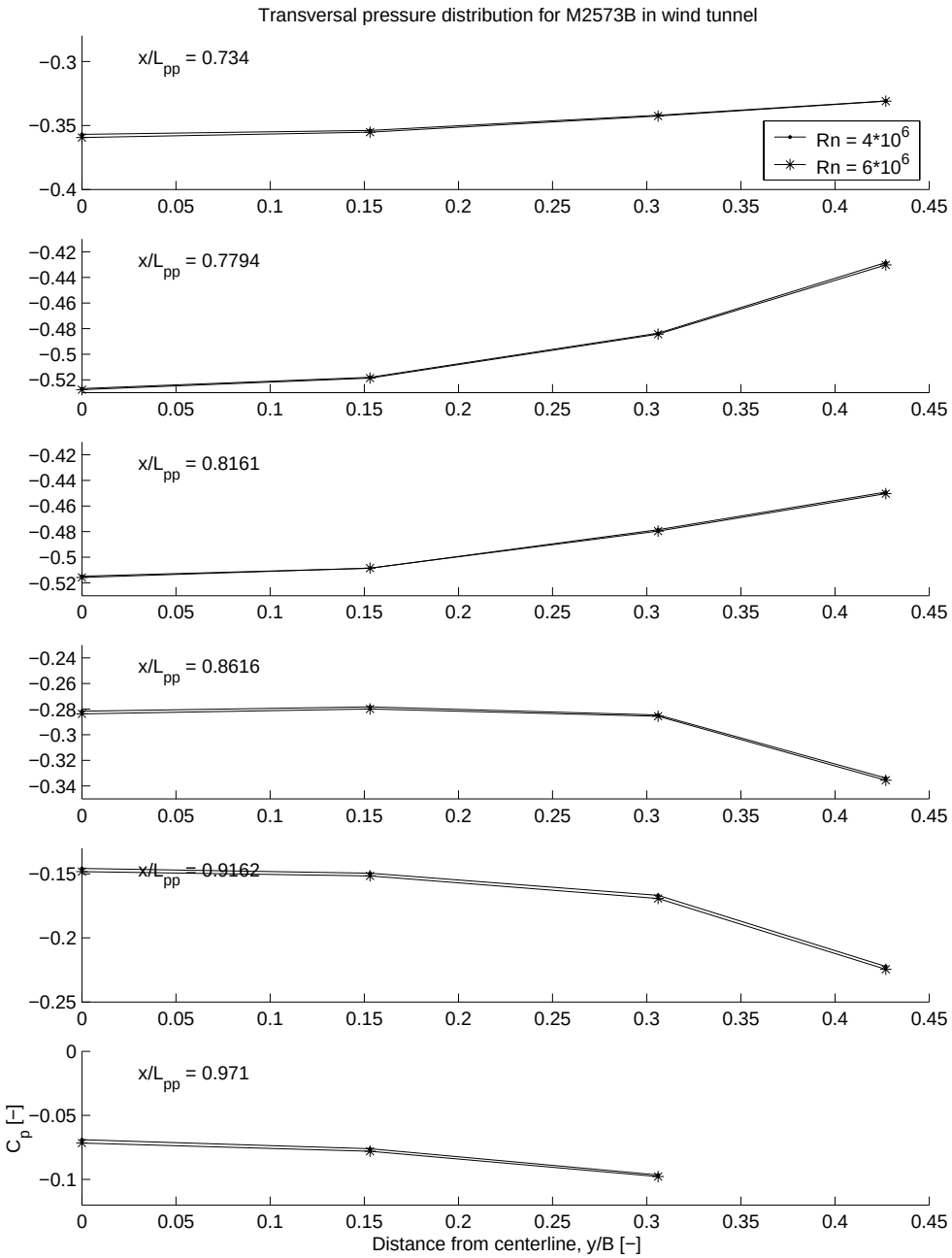

Figure 4.10: *Transversal pressure distribution for Mod B.*

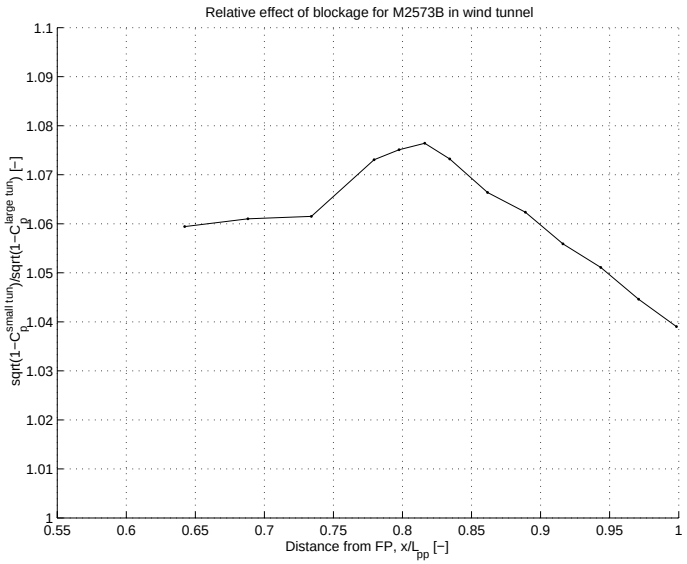

Figure 4.11: *The figure shows the relative blocking effects between the small tunnel and the large tunnel. This is for flow along C_L for Mod B.* $U_{smalltun}/U_{largetun} = \sqrt{1 - C_{p,smalltun}}/\sqrt{1 - C_{p,largetun}}$

to see that $\partial u/\partial y$ is changing less for Mod B than for Mod A aftwards of $x/L_{pp} = 0.8$. This is according to theory, since Mod B has a shorter aft run and has less margin to separation than Mod A. It is also interesting to see the Reynolds number dependency of $\partial u/\partial y$ by comparing figs. 4.20 and 4.21. We see that $\partial u/\partial y$ is changing less for the lower Reynolds number than the higher in the area from the aft shoulder and aftwards. The difference is small, but there is a trend, and this is also according to theory, because for a higher Reynolds number, we have a larger margin to separation.

We were unfortunately not able to measure close enough to the wall to achieve information about the viscous sublayer. With the thinnest pitot tube which was practical to use (Ø 1mm), we achieved $y^+ \approx 2 * 10^3$. To have information about the viscous sublayer, we should have been able to measure as close to the wall as $y^+ < 5$.

Measurement errors The hull is highly curved over the aft shoulder. This means that the static pressure will vary across the boundary layer in the vicinity of the shoulder. The main boundary layer measurements are done with a pitot tube without static tube, and we used the static port at the wall

as static pressure reference. This introduces errors in the measurements of BL velocity in the vicinity of the shoulder. The reason to use the smaller pitot tube instead of a pitot-static tube is that it can measure closer to the wall, and will after all give a better estimate of the BL velocity.

A test was done to measure how the static pressure varied across the BL. The results are shown in fig. 4.23. The figure shows the error between the velocity profile how it was measured with pitot-static tube and a pitot tube will static pressure at the wall as reference. Fig. 4.22 shows log-plots of these velocity profiles at port #90 which has the largest static pressure variation. From fig. 4.22 we see that the ports #70-100 (see fig. 4.1 and tab. 4.2) have the largest error, these are also the ports in the vicinity of the shoulder.

The error in measured velocity profile velocity is about 8% close to the wall, and 1.5% in the vicinity of the outer edge of the boundary layer. For the velocity profiles over the curved shoulder, this source of error is larger than the measurement errors due to pressure transducer etc. which was handled in sec. 4.1.3. For the velocity profiles on flat surfaces, the errors handles in sec. 4.1.3 will be the important source of error.

4.1.5 Calculations of boundary layer characteristics

I figures 4.24 to 4.30 we have calculated local friction coefficient, boundary layer thickness, boundary layer displacement and shape factor for the measurements presented in the former section.

The calculations are done with a fortran program made by P. Å. Krogstad. This program calculates boundary layer thickness, displacement thickness, momentum thickness, friction coefficient with different methods and wake parameters and strength. Boundary layer displacement thickness and boundary layer momentum thickess are calculated like this

$$\delta_1 = \int_0^Y 1 - \frac{u}{U_e}\, dy \tag{4.3}$$

$$\delta_2 = \int_0^Y \frac{u}{U_e}\left(1 - \frac{u}{U_e}\right) dy \tag{4.4}$$

where δ_1 is the displacement thickness, δ_2 is the momentum thickness, u is the velocity in the boundary layer at a distance y normal to the wall, U_e is

Figure 4.12: *The picture on top shows tufts on the surface of Mod A. The bottom picture shows the same for Mod B. Both runs are done at 22 m/s.*

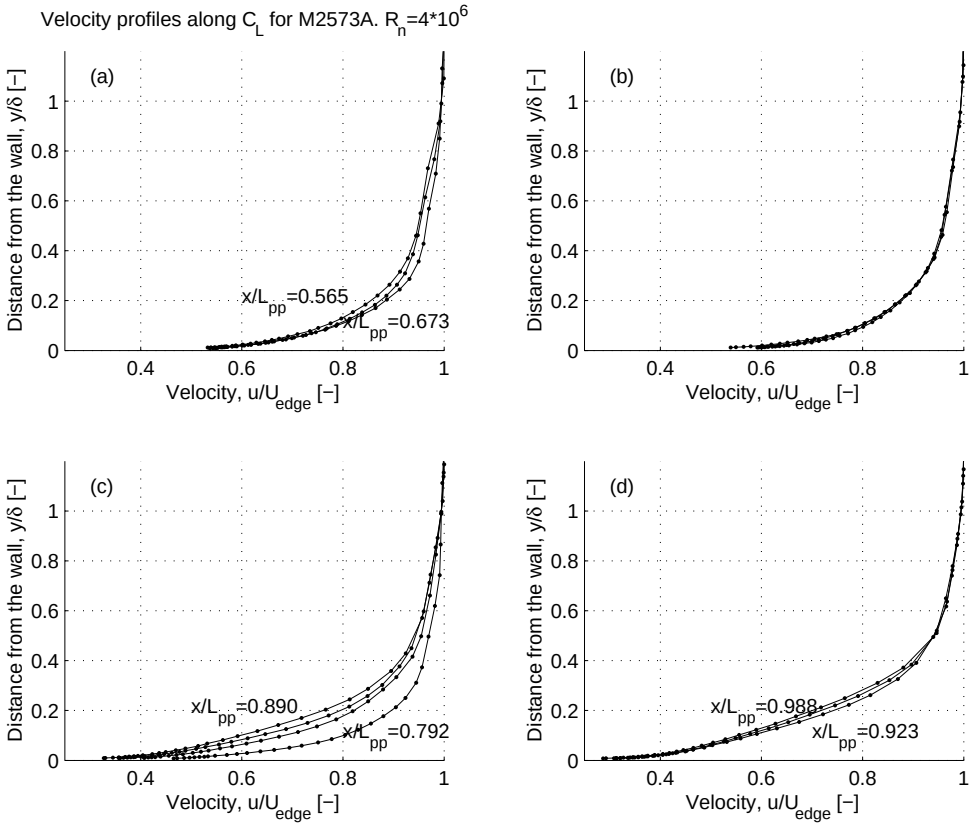

Figure 4.13: *Evolution of the mean velocity profile along* C_L *of Mod A.* $Rn = 4 * 10^6$ *(a)* $x/L_{pp} = 0.565, 0.619, 0.673$*; (b)* $x/L_{pp} = 0.727, 0.749, 0.771$*; (c)* $x/L_{pp} = 0.792, 0.825, 0.858, 0.89$*; (d)* $x/L_{pp} = 0.923, 0.955, 0.988$*. Plot of distance from the wall versus BL velocity.*

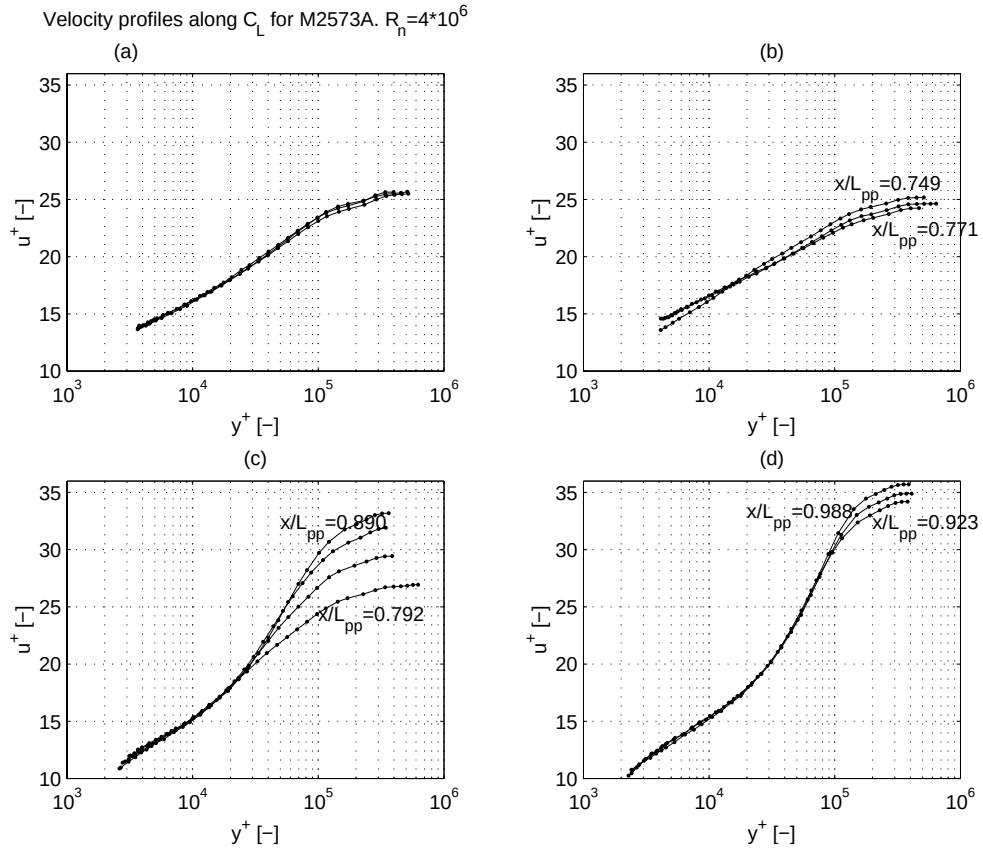

Figure 4.14: *Evolution of the mean velocity profile along C_L of Mod A. $Rn = 4 * 10^6$ (a) $x/L_{pp} = 0.565, 0.619, 0.673$; (b) $x/L_{pp} = 0.727, 0.749, 0.771$; (c) $x/L_{pp} = 0.792, 0.825, 0.858, 0.89$; (d) $x/L_{pp} = 0.923, 0.955, 0.988$. Logarithmic plot with dimensionless variables.*

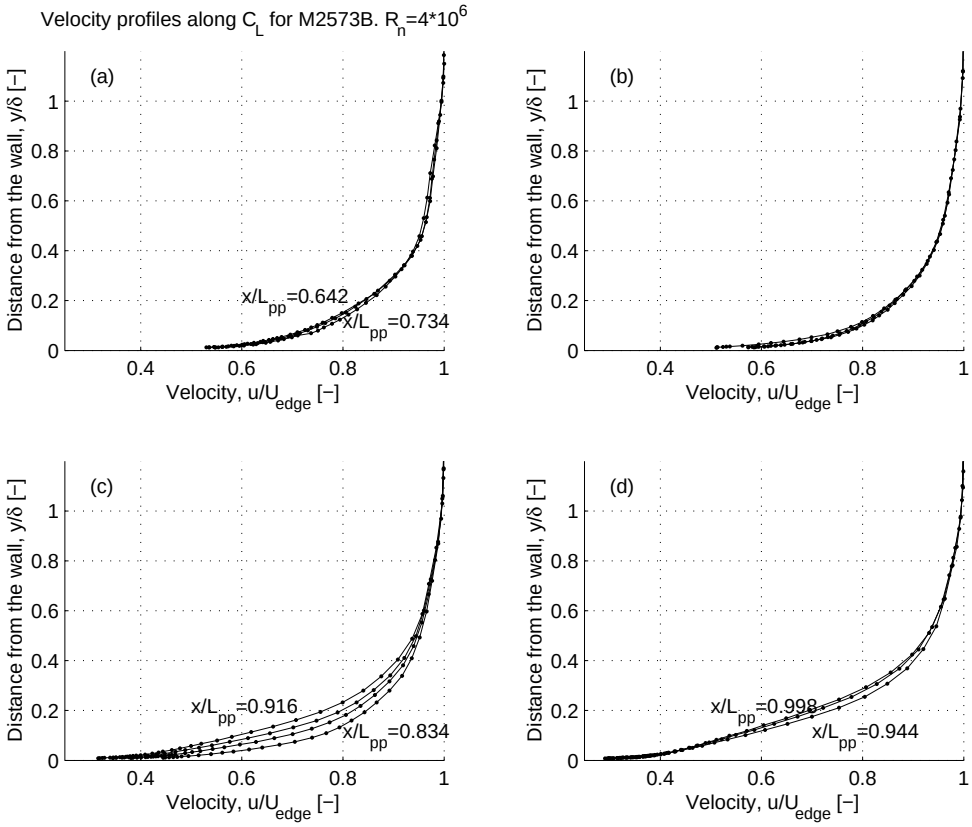

Figure 4.15: *Evolution of the mean velocity profile along* C_L *of Mod B.* $Rn = 4 * 10^6$ (a) $x/L_{pp} = 0.642, 0.688, 0.734$*;* (b) $x/L_{pp} = 0.779, 0.798, 0.816$*;* (c) $x/L_{pp} = 0.834, 0.862, 0.889, 0.916$*;* (d) $x/L_{pp} = 0.944, 0.971, 0.998$*. Plot of distance from the wall versus BL velocity.*

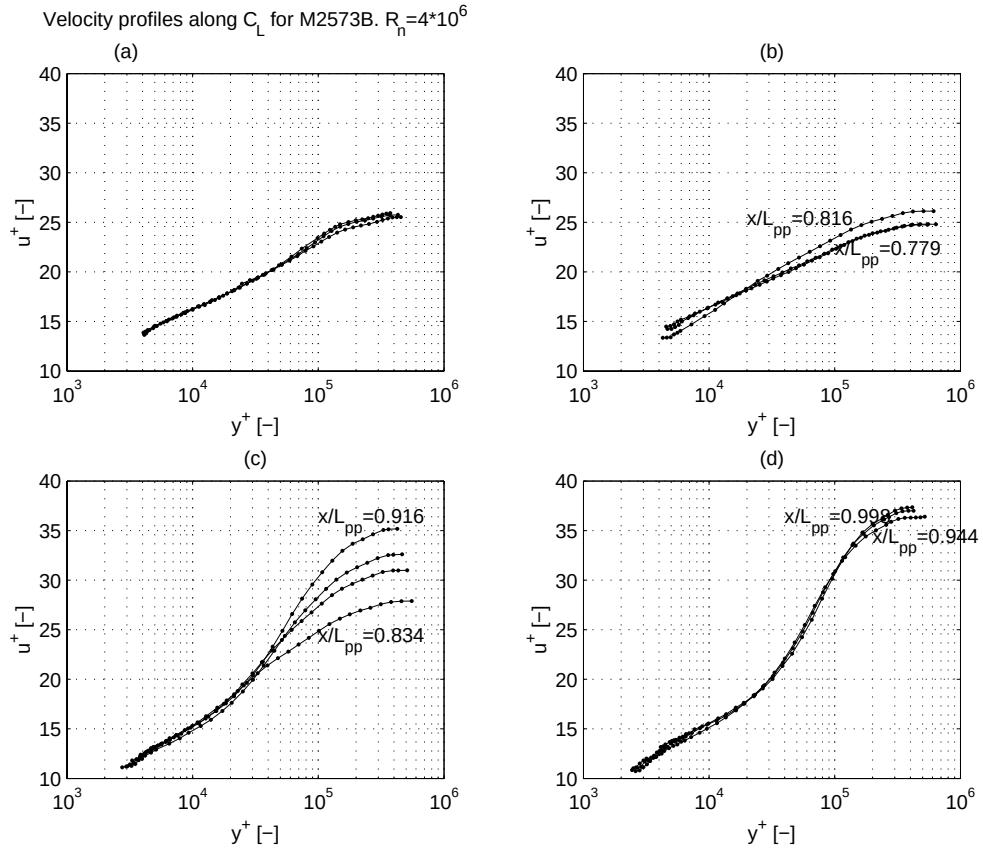

Figure 4.16: *Evolution of the mean velocity profile along C_L of Mod B. $Rn = 4 * 10^6$ (a) $x/L_{pp} = 0.642, 0.688, 0.734$; (b) $x/L_{pp} = 0.779, 0.798, 0.816$; (c) $x/L_{pp} = 0.834, 0.862, 0.889, 0.916$; (d) $x/L_{pp} = 0.944, 0.971, 0.998$. Logarithmic plot with dimensionless variables.*

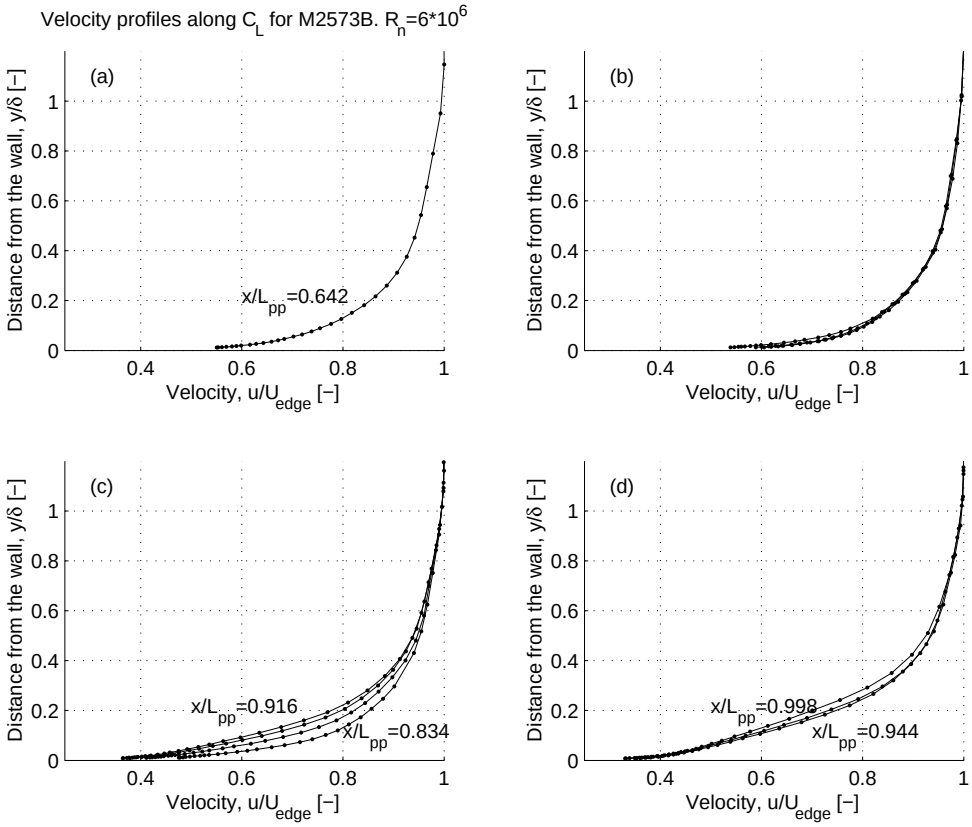

Figure 4.17: *Evolution of the mean velocity profile along C_L of Mod B.* $Rn = 6 * 10^6$ (a) $x/L_{pp} = 0.642, 0.688, 0.734$*;* (b) $x/L_{pp} = 0.779, 0.798, 0.816$*;* (c) $x/L_{pp} = 0.834, 0.862, 0.889, 0.916$*;* (d) $x/L_{pp} = 0.944, 0.971, 0.998$*. Plot of distance from the wall versus BL velocity.*

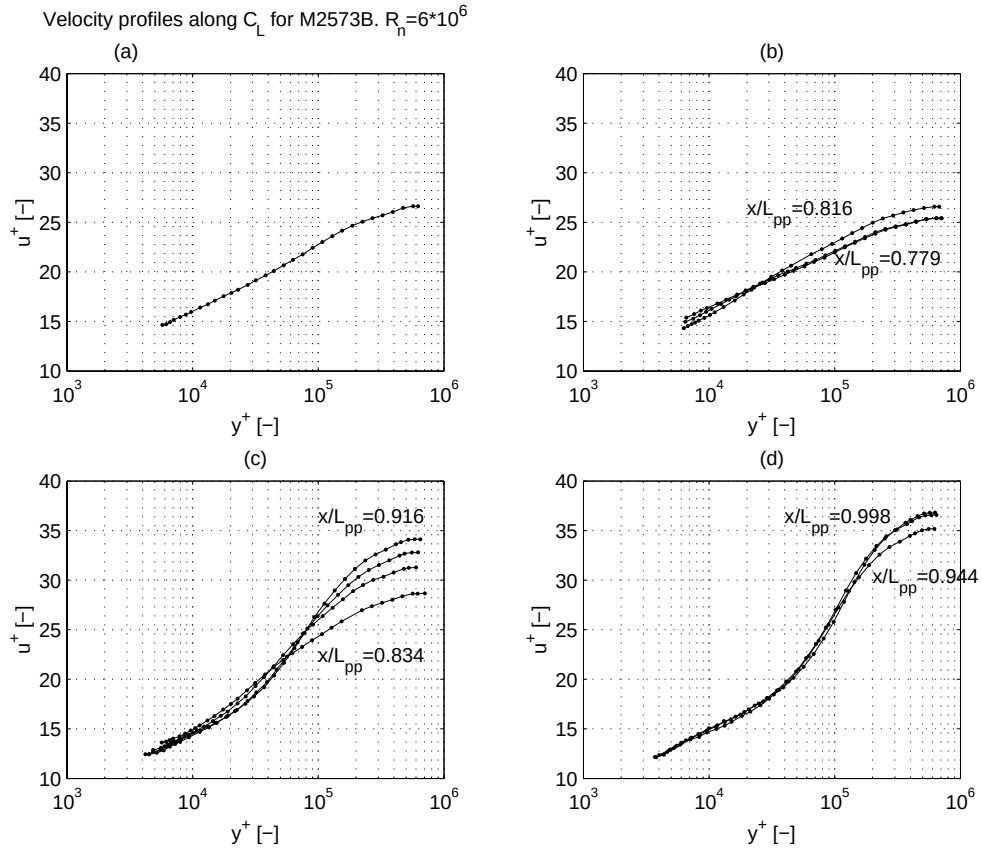

Figure 4.18: *Evolution of the mean velocity profile along C_L of Mod B. $Rn = 6 * 10^6$ (a) $x/L_{pp} = 0.642, 0.688, 0.734$; (b) $x/L_{pp} = 0.779, 0.798, 0.816$; (c) $x/L_{pp} = 0.834, 0.862, 0.889, 0.916$; (d) $x/L_{pp} = 0.944, 0.971, 0.998$. Logarithmic plot with dimensionless variables.*

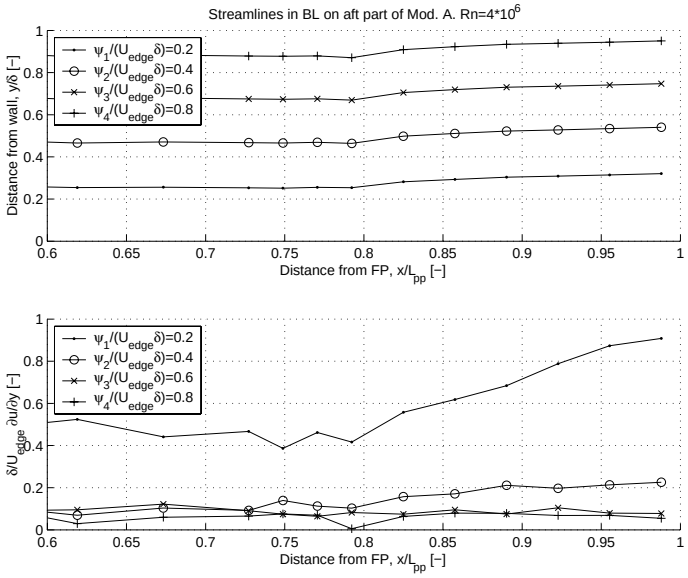

Figure 4.19: *The top figure shows streamlines in BL of Mod. A. The bottom figure is a plot of $\partial u/\partial y$, ref. eq.* (2.30) *along each of the streamlines shown in the plot on top.* $Rn = 4 * 10^6$.

the local free stream velocity on the edge of the boundary layer. The integral is taken from the innermost measurement point to the measurement point in the free stream. The shape factor is the ratio between δ_1 and δ_2

$$H_{12} = \frac{\delta_1}{\delta_2} \tag{4.5}$$

Reynolds number of velocity profiles with respect to momentum thickness is given by

$$Rn_{\delta 2} = \frac{U_e \delta_2}{\nu} \tag{4.6}$$

The friction coefficient is calculated with two methods. In the first method C_f is obtained by matching data to the law of the wall at (y^+, u^+). Where

$$y^+ = \frac{y v^*}{U_e} \qquad u^+ = \frac{U_e}{v^*} \tag{4.7}$$

This method is called Clausers method, and is outlined in [43]. The method is based on equation 4.8.

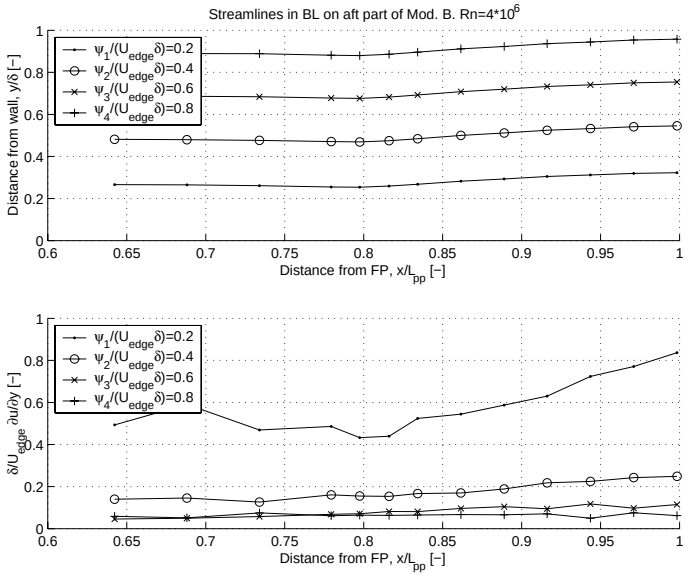

Figure 4.20: *The top figure shows streamlines in BL of Mod. B. The bottom figure is a plot of $\partial u/\partial y$, ref. eq.* (2.30) *along each of the streamlines shown in the plot on top.* $Rn = 4 * 10^6$

$$\frac{u}{U_e} = \frac{v^*}{U_e}\left(\frac{1}{\kappa}\ln\frac{yU_e}{\nu} + \frac{1}{\kappa}\ln\frac{v^*}{U_e} + B\right) \tag{4.8}$$

where v^* is the friction velocity, and ν is kinematic viscosity. κ and B are near-universal constants past smooth impermeable walls. The values of κ and B used in the program is given in eq. (2.13).

The method calculated eqn 4.8 with $v^*/U_e = \sqrt{C_f/2}$ as parameter. The closest match of parameters determines the skin friction coefficient C_f for the actual set of boundary layer velocities u and distance from the wall, y. The skin friction coefficient is defined by

$$C_f = \frac{\tau_w}{1/2\rho U_0^2} \tag{4.9}$$

where τ_w is wall shear stress.

Further the friction coefficient and wake strength are calculated by a least squares fit to the law of the wall. This method is due to van Driest [37]. The

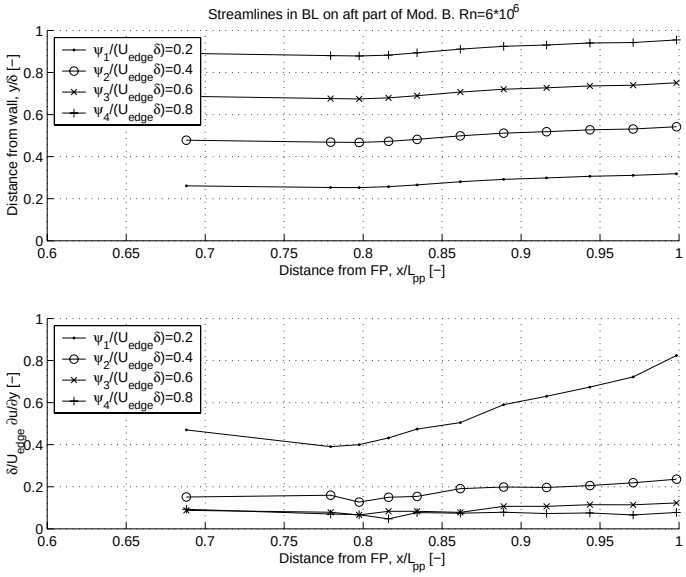

Figure 4.21: *The top figure shows streamlines in BL of Mod. B. The bottom figure is a plot of $\partial u/\partial y$, ref. eq.* (2.30) *along each of the streamlines shown in the plot on top.* $Rn = 6 * 10^6$

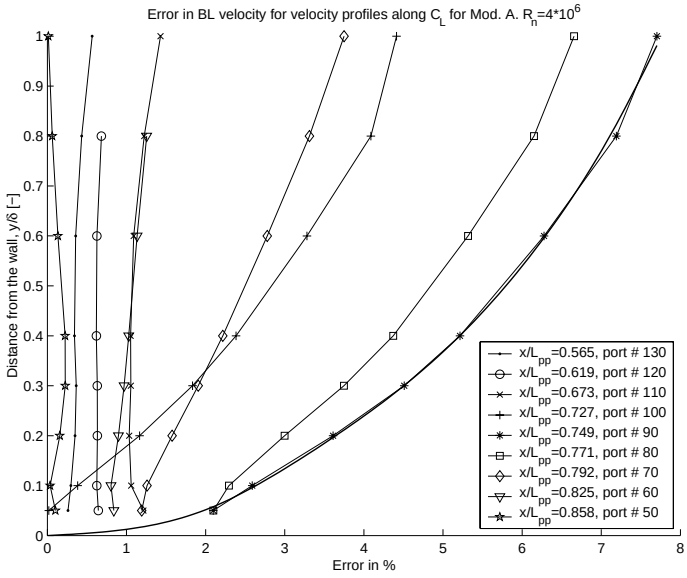

Figure 4.22: *Error in BL velocity using pressure port on wall as static pressure reference instead of static pressure from pitot static tube. Mod A.* $R_n = 4 * 10^6$

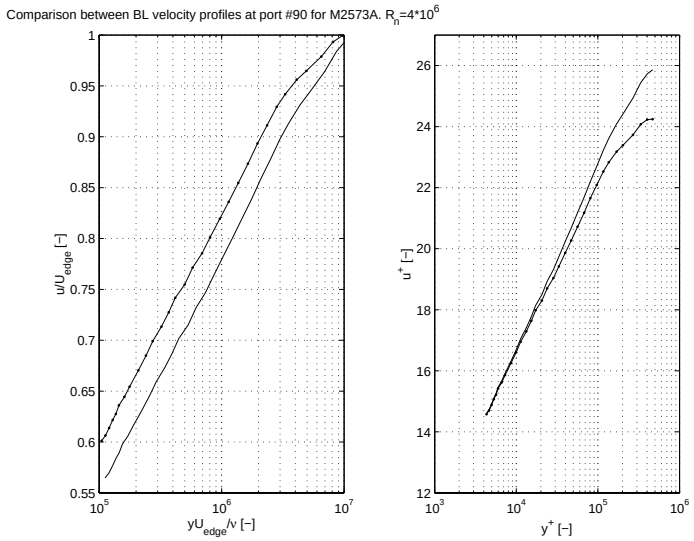

Figure 4.23: *Comparison between BL velocity profiles using pressure port on wall as static pressure reference (line with dots) instead of static pressure from pitot static tube (solid line). Mod A, port #90 ($x/L_{pp} = 0.749$). $R_n = 4 * 10^6$.*

theory gives a continuous velocity and shear distribution for turbulent flow near a smooth wall. The theory is based on Prandtls mixing length theory.

From the calculations of local friction velocity we see that the difference between the results from the two methods is relatively small.

It is astonishing how well the results of skin friction from measurements corresponds with the 2D calculations, see fig 4.24, 4.26 and 4.28. Wee see that in the aft part of the ship the end effects are pronounced. The 2D calculations are based on a momentum integral method, and the method is described in [38]. For the 2D calculations we have put together the ships SAC for the fore part of the ship, and the centerline buttock for the aft part. This is oulined in section 3.5.1.

The Schoenherr skin friction line for local friction coefficient for flat plate flow is also shown in the plots for comparison. This is calculated with the bow point as the start of the plate. This relation holds for incompressible low-speed flow, and is derived in [40]

$$\frac{1}{\sqrt{C_f}} = 4.15 \log(Rn_x C_f) + 1.7 \tag{4.10}$$

where C_f is local skin friction coefficient and Rn_x is local Reynolds number from start of plate. A similar formula which gives the same results is given in [25].

The agreement with both the measurements and the 2D calculations is good in the midship range. This is also what Matheson and Joubert found, [22] and [23]. This indicates that the flow on the bottom is rather 2D in the midship range.

Figs. 4.25, 4.27, 4.29 and 4.30 shows calculated boundary layer characteristics from measurements and 2D momentum integral calculations. Here the results from measurements are a little higher than the calculated results for δ_1 and δ_2. That could be due to the turbulence trigging arrangement. We maybe should have used finer grain of sand and a narrower band for the turbulence stimulation. This could have produced a thinner boundary layer. We see from the figures that the curves have a very similar behaviour for the two hulls. There is good agreement of the results up to $x/L_{pp} = 0.9$, and after that the end effects are pronounced, and gives diverging results. In fig. 4.30 the results for two different Reynolds numbers are given.

In fig. 4.26 we have calculated local friction coefficient and corrected for the blockage effect. That means the measured velocity profiles for each section is multiplied with the inverse of the relative blockage from fig. 4.11. The new reduced velocity profiles is then input to the BL calculation program mentioned at the beginning of this section, and the new results are given as stars in fig. 4.26. By comparing the results with blocking with those corrected for blocking we see that even though the blocking effect has a large impact on the pressure coefficient, it has relatively small impact on the local friction coefficient. At section #80 (aft shoulder) the relative difference is 1.7 %. For the boundary layer displacement and boundary layer momentum thickness the difference was close to zero for all sections. We therefore conclude that the blockage effects due to the ship models acceleration of the flow over the model is not influencing our results severely.

4.1.6 Measurements of wake

In figs. 4.31, 4.32 and 4.33 the axial velocity in the propeller plane is measured. The wake shows a satisfactory 2D structure transversally. Along the center of the ship there is a larger wake. This is due to vortices forming from the bulb. We could see this by moving a stick with woolen tuft into the center area of the ship. The flow was smooth and nice away from the center, but when we

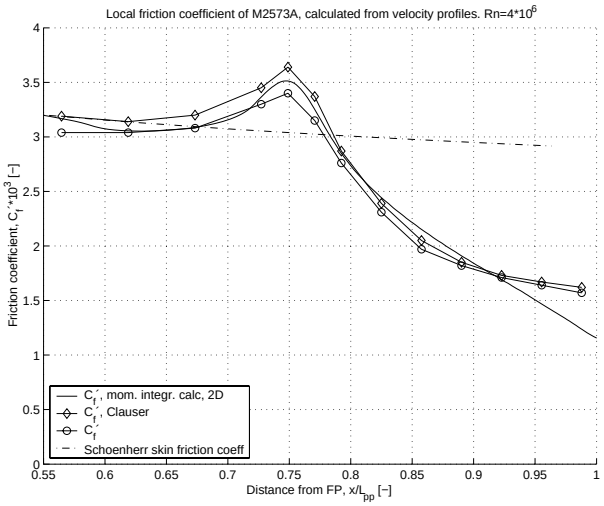

Figure 4.24: *Local friction coefficient calculated from boundary layer measurements on Mod A.*

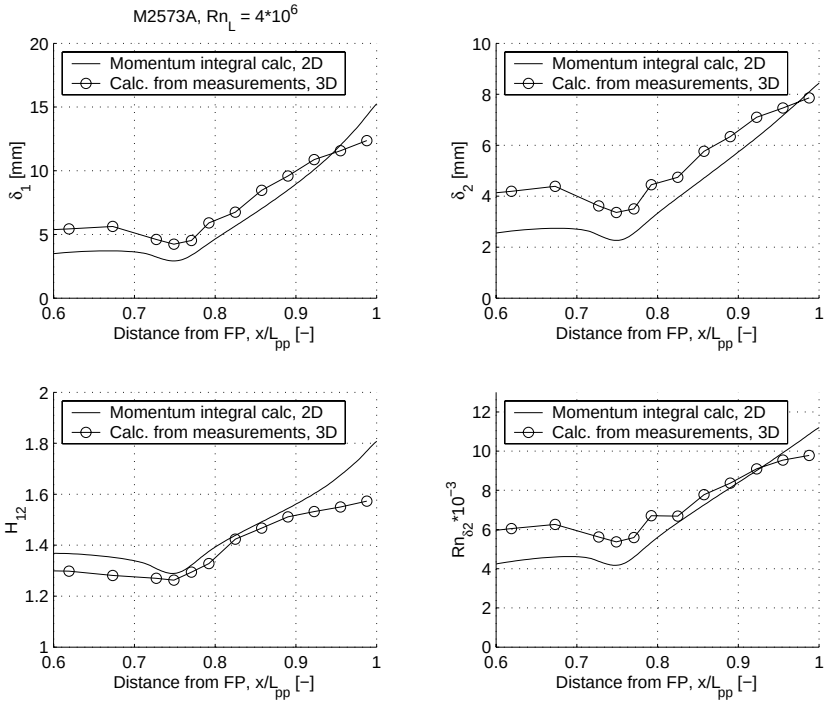

Figure 4.25: *Calculated boundary layer characteristics from measurements on Mod A.*

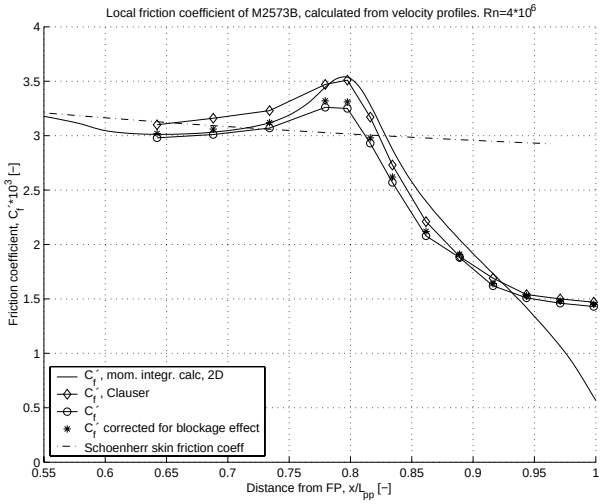

Figure 4.26: *Local friction coefficient calculated from boundary layer measurements on Mod B.*

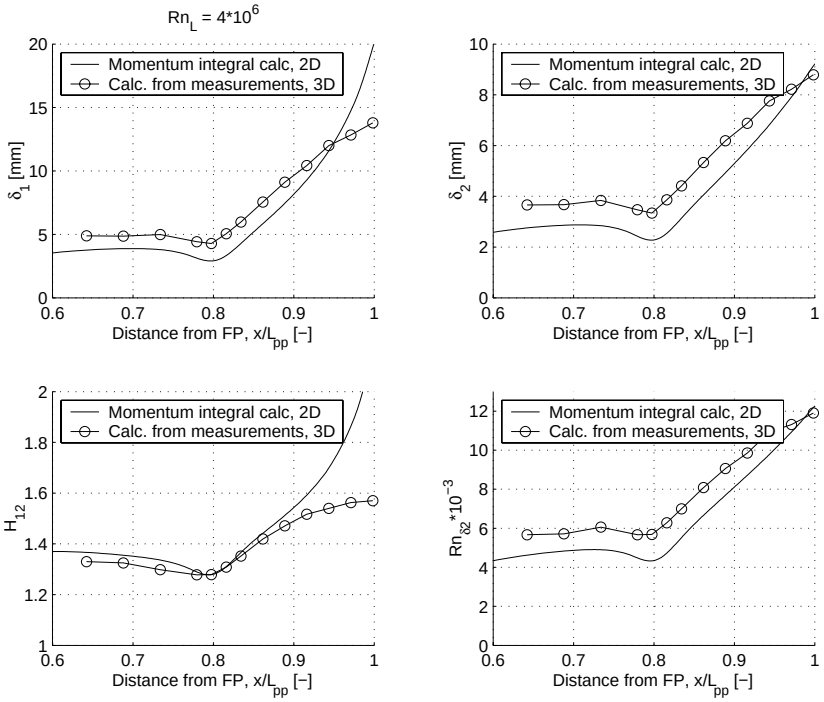

Figure 4.27: *Calculated boundary layer characteristics from measurements for Mod B.*

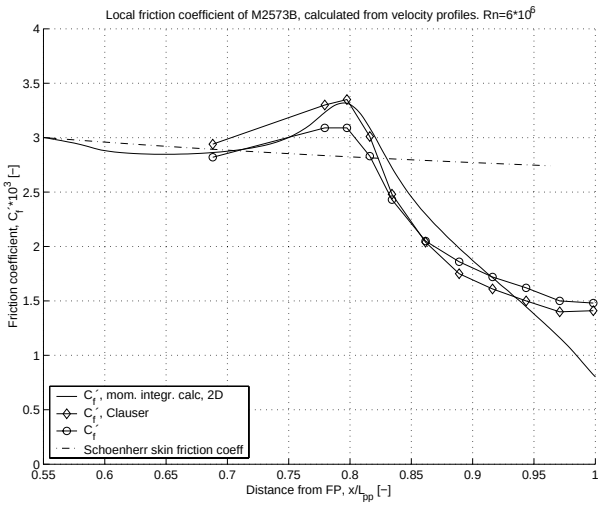

Figure 4.28: *Local friction coefficient calculated from boundary layer measurements on Mod B.*

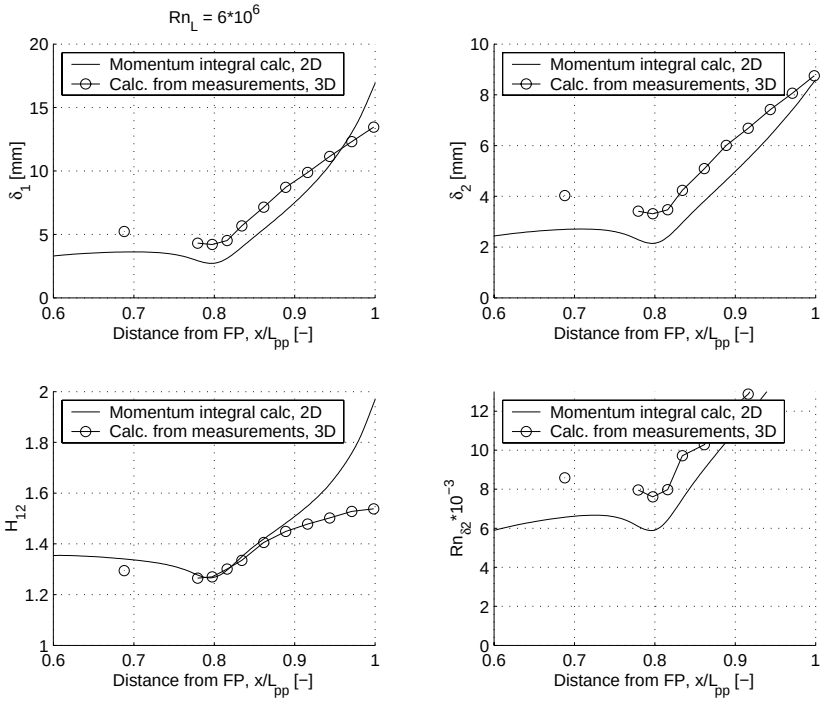

Figure 4.29: *Calculated boundary layer characteristics from measurements on Mod B.*

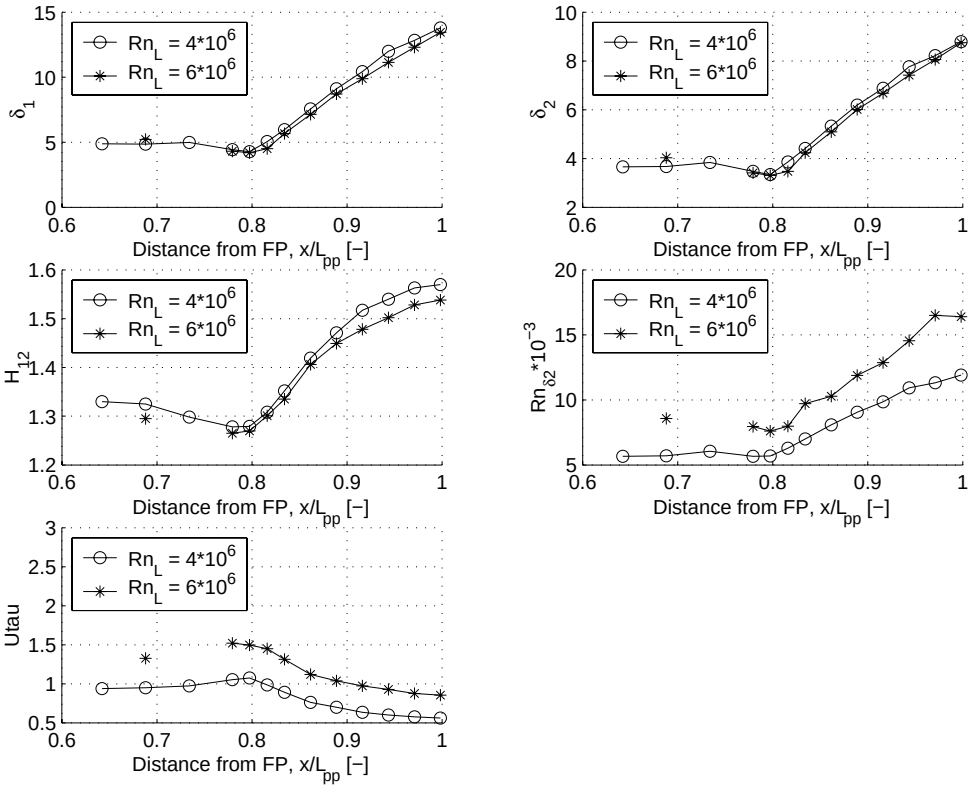

Figure 4.30: *Calculated boundary layer characteristics from measurements on Mod B.* $R_n = 4 * 10^6$ *and* $R_n = 6 * 10^6$

moved it to the center, the tufts started to flutter some. The effect is not very pronounced, but could be observed. In fig. 4.33 we have done the wake measurements with a center skeg. By comparing figs. 4.32 and 4.33 we see that the skeg is influencing the wake in the measured area to a small extent.

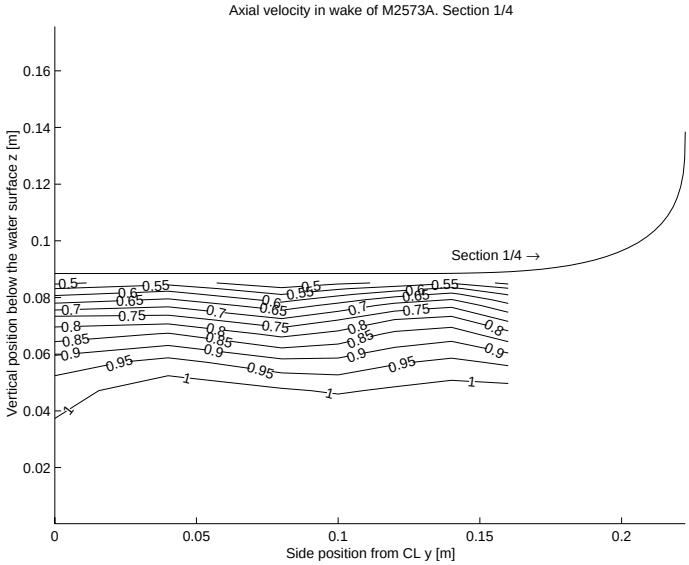

Figure 4.31: *The contour lines show the axial velocity of flow relative to ship velocity in the propeller wake. Mod A without skeg.*

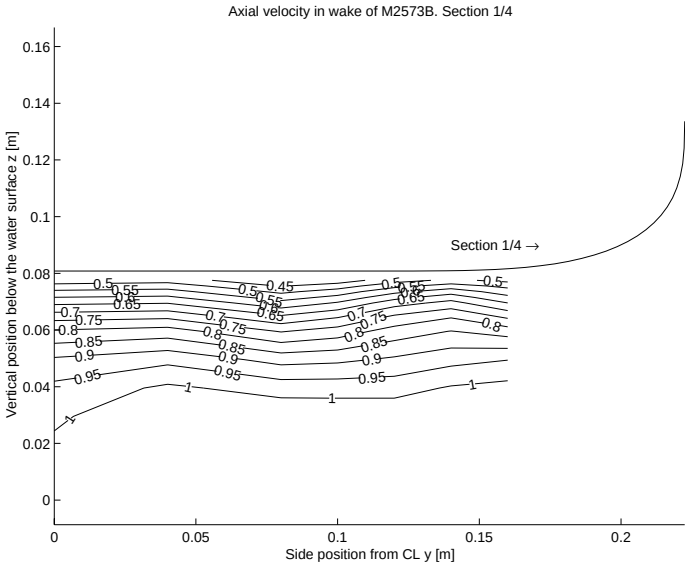

Figure 4.32: *The contour lines show the axial velocity of flow relative to ship velocity in the propeller wake. Mod B without skeg.*

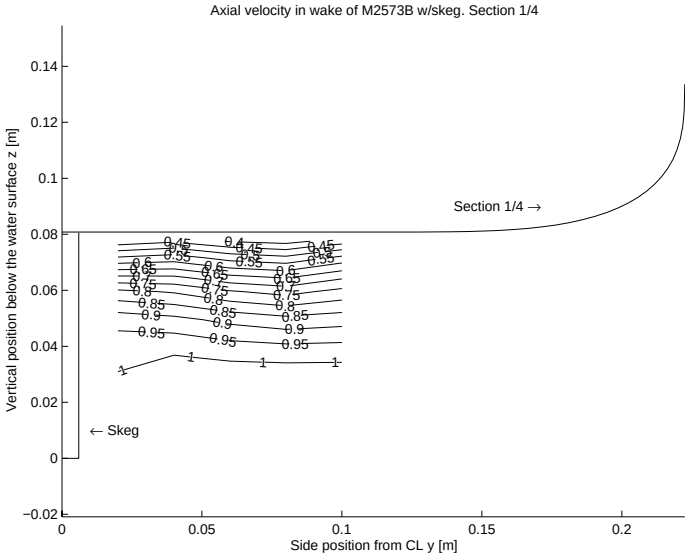

Figure 4.33: *The contour lines show the axial velocity of flow relative to ship velocity in the propeller wake. Mod B with skeg.*

4.2 Results from towing tank

4.2.1 The towing tank facility and measurement techniques

The towing tank is located at NTNU in Trondheim. The tank is 260 m long, 10.5 m wide and 5 m deep for the first 175 m of test length, and 10 m in the rest. The carriage has a maximum test speed of 8.3 m/s, and an acceleration of 1 m/s^2.

The ship model in the towing tank also had ports for static pressure measurements at the same locations as the model in wind tunnel. We are then able to compare the static pressures from towing tank with those from wind tunnel on the same hull.

All static pressure differences were done with port #130 as reference, see table 4.2. That means we only have pressure differences relative to this location, not relative to free stream velocity, as in the wind tunnel measurements. It was assumed that the static pressure at port #130 which is around midship, relative to free-stream static pressure was the same for the wind tunnel model and the towing tank model. This will be commented further.

The tests were done with the ship model free to trim and sink, and tests with the model locked to the carriage. With the model free, towing force, trim, sinkage and static pressures were measured. With the model locked, only static pressures were measured.

In the towing tank only the Mod B was tested, not Mod A. For the towing tank tests this model is named M2574, and this is the same hullform as Mod B.

4.2.2 Measurements of wave resistance, trim and sinkage

With the model free to sink and trim, we measured towing force, trim and sinkage in a speed range of Froude numbers from 0.1 to 0.4. This corresponded to from 7 knots to 29 knots. The model was towed at small velocities so that we could use Prohaskas method to calculate the form factor of the model, see fig. 4.39. The form factor k, was estimated to be 0.15. The measurements below Fn=0.17 are inaccurate. This inaccuracy has several reasons. First of all we may have considerable laminar flow on the hull surface aft of the turbulence trigging sandstrip. Second reason is a wet transom stern, and an aft hull wave which do not separate from the transom, but which is stowing up just at

transom, see picture on top in fig. 4.36. A third reason to the inaccuracy at low velocities is oscillations in towing force for Froude numbers below 0.2. That is because the ship model, force transducer and flow around the model behaves like a mass-spring-damping system with relatively small damping. In the mass-spring-damping system we probably have underdamping, which means the damping of the system is small compared to the mass and spring constant of the force transducer. We maybe could have solved this problem by using a force measuring equipment which had a smaller spring constant. This could have given us an overdamped system, and the oscillations could have been smaller.

Fig. 4.37 shows wave resistance coefficient, C_w with respect to Fn. In the calculation of C_w from measurements we have used a form factor of k=0.15, found from Prohaska/Inuis method.

If we compare the pictures of wave formation for Fn=0.28 to Fn=0.40 in fig. 4.35, which is a zoom of fig. 4.34, it is interesting to notice that the wave formation in the shoulder area is largest for Fn=0.31. The waves along the aft part of hull decreases for higher Fn, and also for the lower Fn compared to Fn=0.31. We also see that for the Fn shown, the aft trough of the wave along the ship does not coincide with the aft shoulder which is situated around station 2, see fig. 3.21. If the aft shoulder were coinciding with the aft trough of wave, we should have redesigned the aft hull to avoid this to happen. The flow acceleration over the aft shoulder will probably contribute significantly to the wave formation from the aft hull, but the effect is largest if a trough from the overall hull wave coincides with the aft shoulder.

The pictures in fig. 4.36 shows stern view of vessel at three diffrerent Froude numbers. For Fn=0.28 the transom stern is still wet. At Fn=0.31 it just separates, and at Fn=0.37 the transom is dry. As we see from fig. 3.21 the centerline buttock at the stern meets the transom stern at the waterline. This means there is no wet transom area at rest, and the transom stern drag will be small.

In fig. 4.37 we have calculated wave resistance coefficient from the resistance measurements. We have used eq. (2.7) to calculate C_W. The air resistance coefficient for the ship model is estimated to be $7.0 * 10^{-5}$, taken from Hoerner [12].

The transom stern drag can be calculated by integrating the hydrostatic force "missing" on the dry transom stern (D'Alemberts paradox). This only applies when the transom is dry, that is for speeds beyond Fn=0.3 for this vessel. The vessel has a sinkage for all speeds at the stern, and the higher the speed,

the larger the sinkage. If we approximate the transom stern to be rectangular with ship breadth and sinkage given, the transom stern drag cofficient is given approximately by

$$C_{BD} = \frac{gB}{S}\left(\frac{H}{U}\right)^2 \tag{4.11}$$

Where H is sinkage at transom stern. At Fn=0.4, the sinkage is 54 mm, and the transom stern drag will be $1.0*10^{-6}$. When we compare both air resistance cofficient and transom stern drag coefficient to wave resistance coefficient in fig. 4.37, we see that these are negligible.

Fig. 4.38 shows the sinkage and trim of the full scale ship, calculated from sinkage at FP and AP in the model tests.

Measurement errors In [10] and [27] Mo-Qin He et al. has a description of uncertainty analysis of towing tests. They divide the error sources into four parts according to measurement systems and conditions:

- Model geometry
- Carriage speed
- Resistance
- Water temperature

Each of these items have individual variables that have bias and precision errors.

The models were manufactured with an error allowances of less than 0.1%. The carriage speed is measured with a higly accurate method. The water temperature were measured every day, and changed very little during the tests.

The resistance is measured with a force transducer, and the bias is a product of bias from transducer, bias from amplifier and from A/D converter. The bias from resistance measurements is less than 1% according to Marinteks specifications.

IITC handles uncertainty analysis for resistance tests in [17]. An Excel spreadsheet is attached to this manual, and this spreadsheet is used to estimate the uncertainty for these towing tests.

Input to the spreadsheet is measurements accuracy of thermometer, model length, breadth and depth accuracy, errors in model speed measurement like AD/DA conversion error. These errors form the error for the total resistance measurement, and further for wave resistance coefficient.

The error in model resistance measurements were about 0.5%, and consists mostly of bias error due to transducer calibration. The total resistance coefficient error is calculated to be 0.6%. This error consists half and half of bias error due to speed and bias error due to resistance measurement.

The error in form factor k is estimated to be 0.02. This gives a relative error of about 7-8%.

The error in wave resistance coefficient is 2.5%, and consists of bias errors due to total resistance coefficient, form factor and frictional resistance coefficient. The two former errors are about equal, and much larger than the latter.

In this error estimation we have not taken into account the problems we faced for low Fn (below 0.18) mention above. The estimation of error below this limit is difficult, because we are dealing with unstable and unpredictable flow phenomenon.

4.2.3 Measurements of static pressure on ship hull

The pressure distribution on centerline of ship model is shown in fig. 4.40. The top figure is for ship free to trim, and the lower figure for ship locked in trim. Pressure port #130 was used as reference pressure for all the other pressure ports. This makes us only able to see the relative pressure between the ports, and not relative to free stream as in the wind tunnel. On second thoughts we should have used a free stream pitot tube to have the absolute pressure on the ports, and not only pressures relative to port #130. We see that in the aft part the measurements from the small wind tunnel diverges from the other measurements. This is due to blockage effect in the small tunnel. The measurements in the large tunnel agrees well with the towing tank results. In the shoulder area it seems that the wave formation for higher Fn gives lower pressure. From pictures of the towing tests we see there is a wave trough just aft of the shoulder area. It is evident that the lower C_p values at Fn=0.28 in the shoulder area is due to the larger wave formation for this velocity compared to Fn=0.37 and 0.15.

Another interesting result is that there is no significant difference in C_p for ship locked in trim compared to ship free to trim. That means change of trim have a negligible effect on the flow in the aft part.

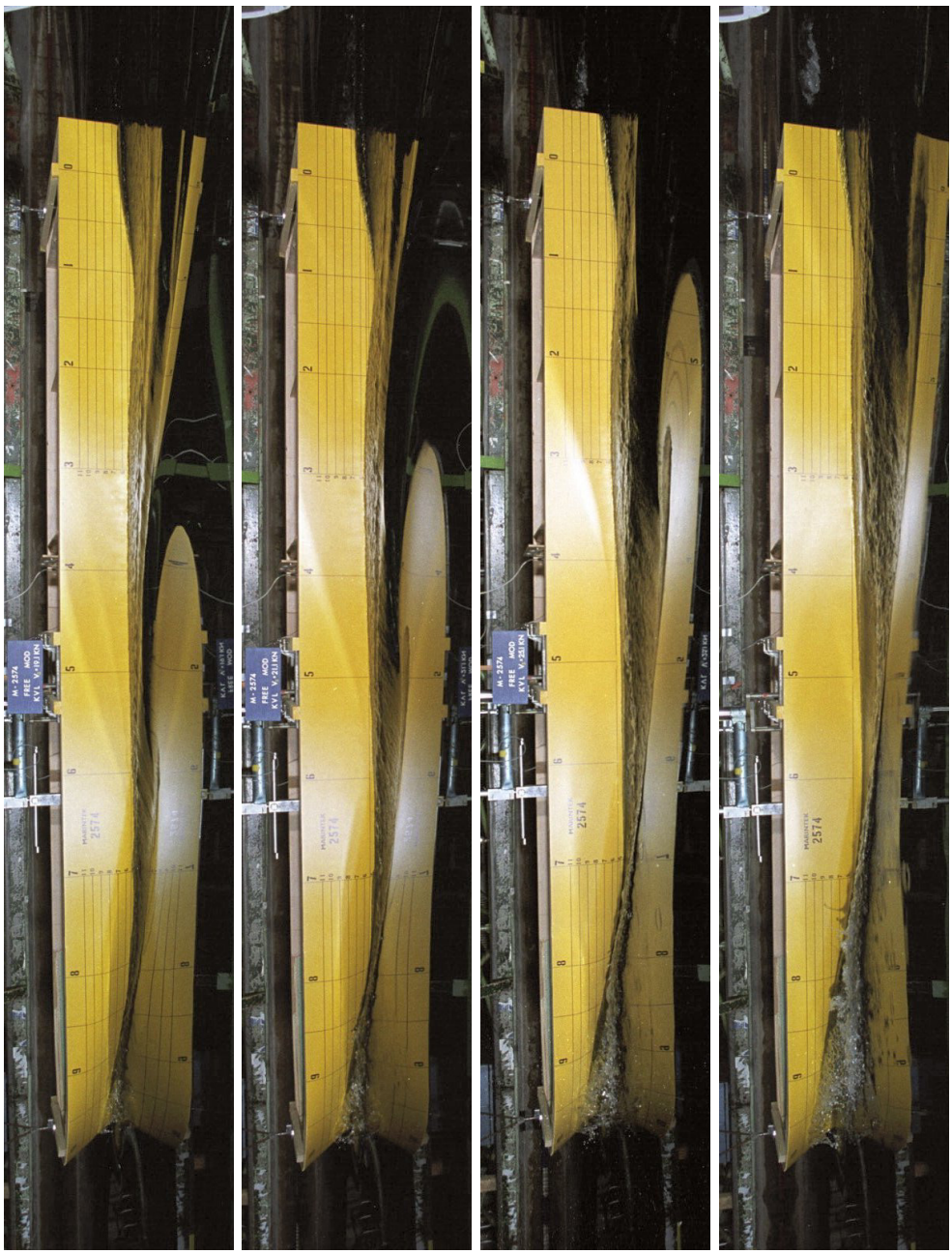

Figure 4.34: *The figures show side view of Mod B. From left to right: 19.1 kn (Fn=0.28), 21.1 kn (Fn=0.31), 25.1 kn (Fn=0.37) and 28.8 kn (Fn=0.40).*

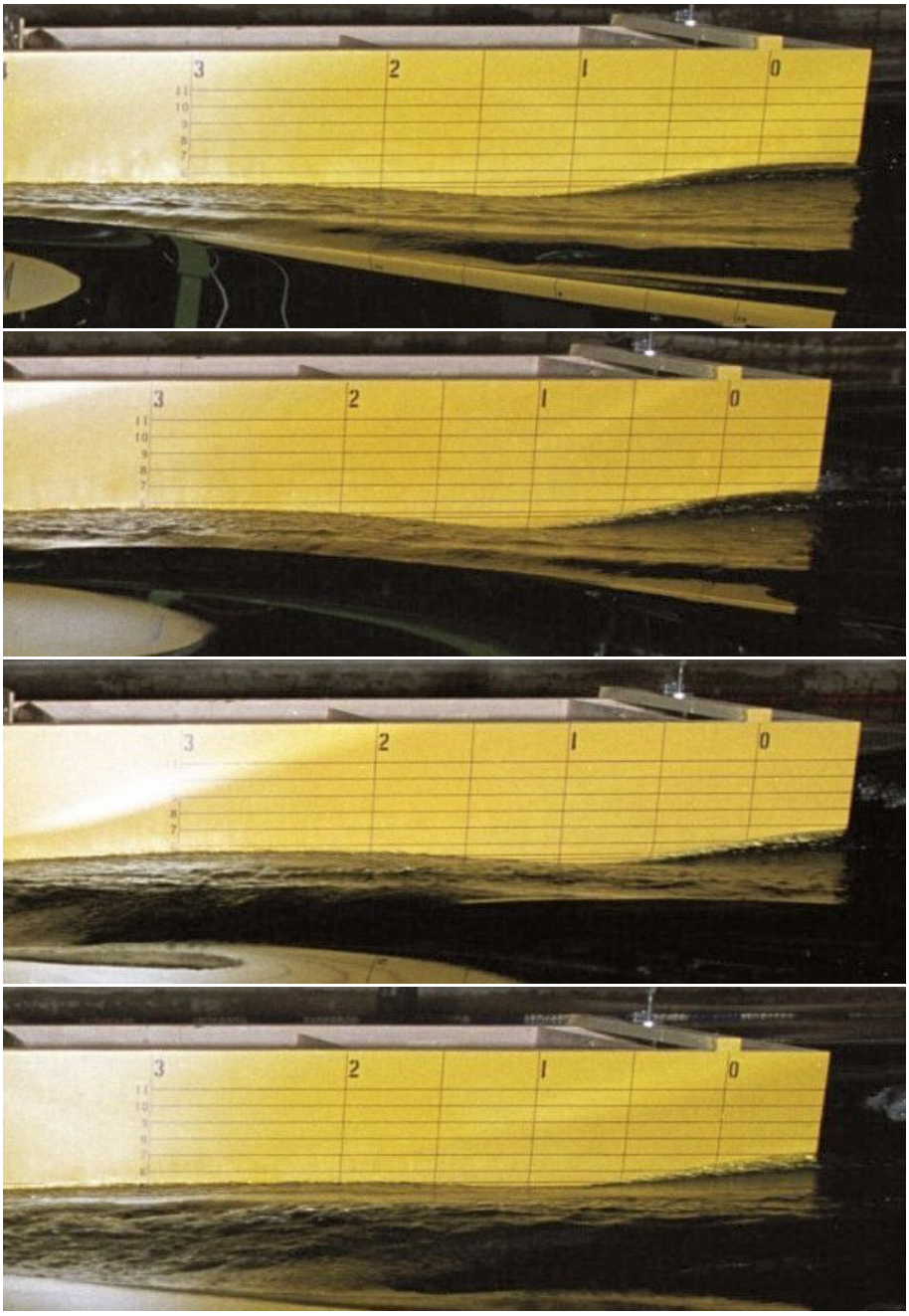

Figure 4.35: *Zoom of side view of Mod B. From top to bottom: 19.1 kn (Fn=0.28), 21.1 kn (Fn=0.31), 25.1 kn (Fn=0.37) and 28.8 kn (Fn=0.40).*

Figure 4.36: *The figures show stern view of Mod B. Top:19.1 kn (Fn=0.28). Middle: 21.1 kn (Fn=0.31). Bottom: 25.1 kn (Fn=0.37)*

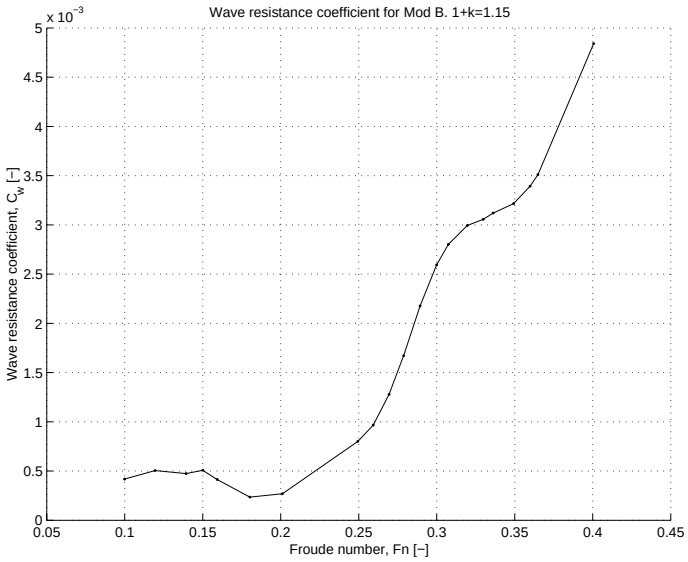

Figure 4.37: *Measurements of wave resistance of Mod B.*

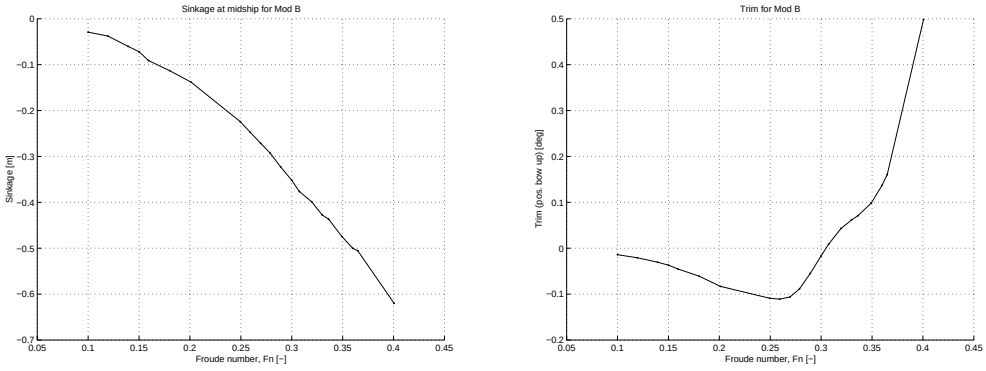

Figure 4.38: *Measurements of sinkage and trim of Mod B.*

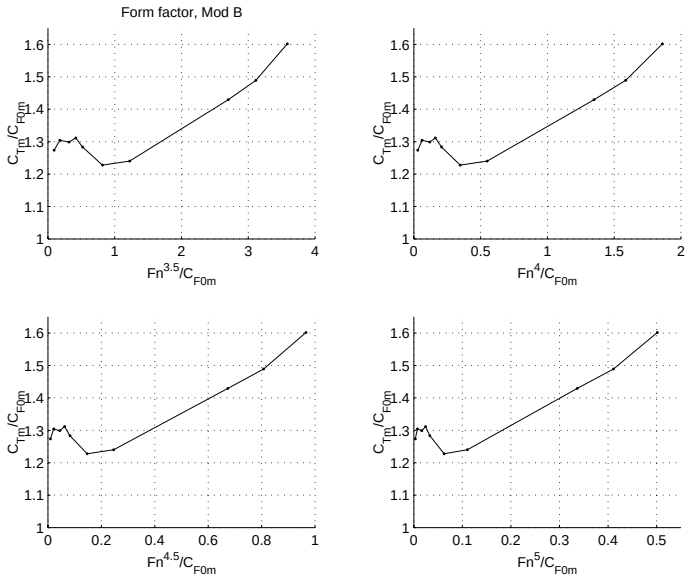

Figure 4.39: *Prohaska/Inuis method to find the value of formfactor (1+k) on measurements of wave resistance of Mod B.*

In figs. 4.41 and 4.42 we have presented the pressure distribution on the ship, both free to trim and locked in trim. Also here we see there is no significant difference in C_p for the two cases. The Fn dependency is a little bit stronger on the ship side than to the center, which is to be expected due to larger wave formation at intermediate Fn.

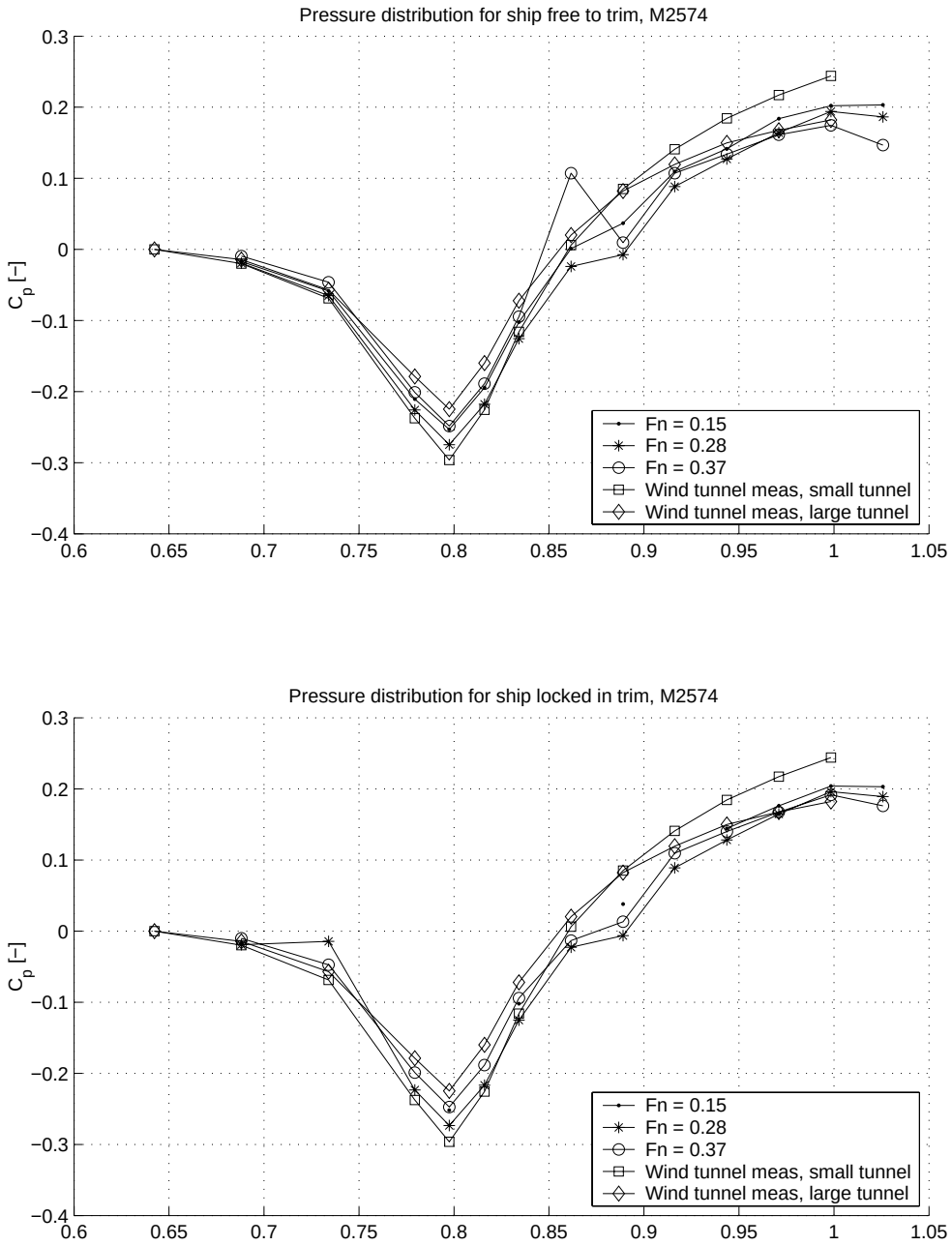

Figure 4.40: *Pressure distribution on centerline of Mod B. Measurements from towing tank and wind tunnel.*

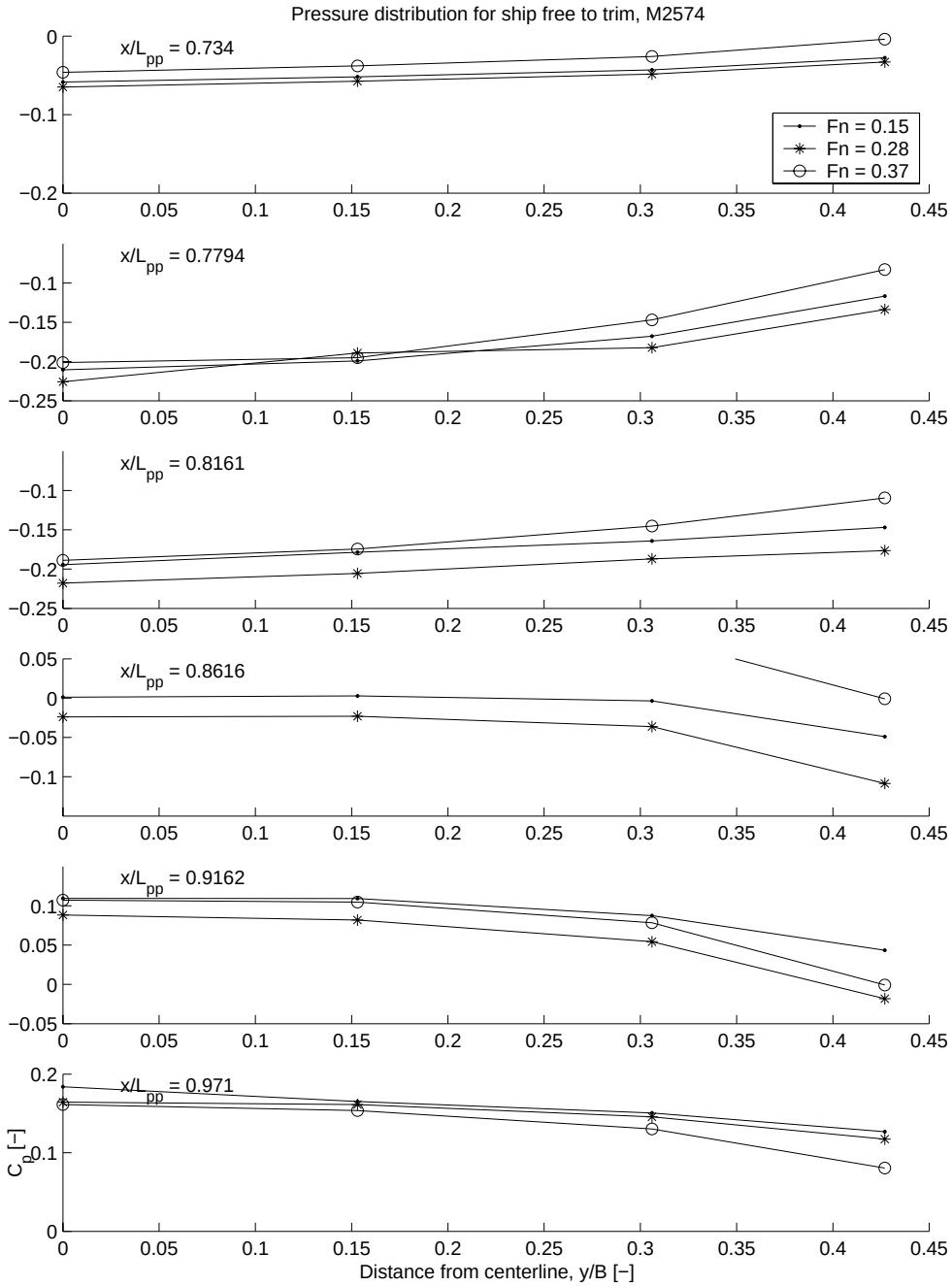

Figure 4.41: *Transversal pressure distribution for Mod B. Ship free to trim and sink.*

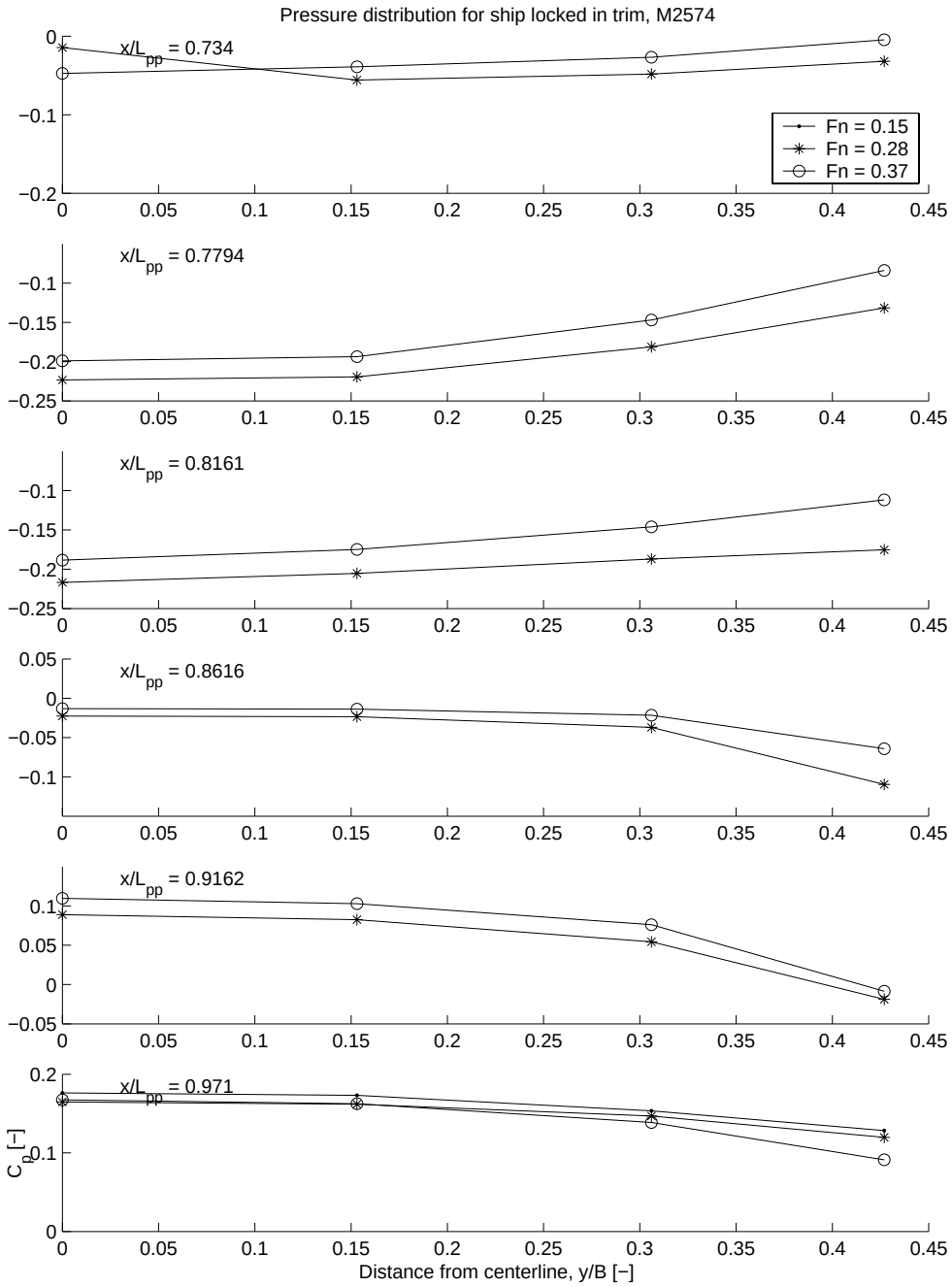

Figure 4.42: *Transversal pressure distribution for Mod B. Ship locked in trim and sinkage.*

Chapter 5

Results from calculations and towing tests of a coastal tanker

This chapter presents a practical application of the developed theory. The author was fortunate to be a part of a commercial ship development project run by a consultancy firm, Rolls Royce Marine, Nord-Vest Consult. There were designed three hull forms, one conventional designed by the consultancy firm, and two hulls where the aftbody of the hulls were designed by the developed optimization technique presented in this thesis.

CFD calculations for all three hulls were done by CFDnorway. This is a small consultancy firm specialized in aerodynamics and hydrodynamics. Both viscous ship flow and free surface non-viscous calculations were done. This is presented in section 5.2.

On the basis of the ship calculations it was decided to build a ship model of hull alt. 3 and test this model in the towing tank at Marintek. These results are presented in section 5.3.

5.1 The hulls of the coastal tankers

In fig. 5.1 hull alt. 1 is the conventional hull. It has straight buttock lines in the aftbody.

Aft part of hull alt. 2 and 3 is designed with the optimization program. Hull alt. 2 has the shortest run from aft bottom shoulder to transom stern. The wetted transom is the same for hull alt. 1 and alt. 2. Hull alt. 3 has larger wetted surface at transom stern due to the larger immersion of the transom stern. From fig. 5.10 we see that the transom is wet for hull alt. 3 with a ship velocity of 13 knots. The same will apply for hull 1 and 2.

All tree hulls have a V-shape at the transom stern of approximately 14°, see fig. 5.2. The optimization theory of this thesis is first of all meant for hulls with flat transom, but introducing V-shaped transom stern only means a smaller angle from the aft knuckle at the bottom to the transom stern at the centerline of the ship. The "Stratford flow profile" is the buttock 5 m from centerline. At this buttock the bilge curvature starts. This means that buttocks closer to the centerline have more conservative run. This design method can of course be questioned. But if we take a look at fig. 5.3, we see that for alt. 3 the wall friction lines on the bottom of the ship are fairly parallell to centerline.

The fore part of the three ships are not identical. They have a slightly different bulb form. This influences the wavemaking resistance to a certain extent.

5.2 CFD calculations

The CFD calculations are performed by CFDnorway, with their in-house software. The method used for the solution of the incompressible Reynolds-averaged Navier-Stokes (RANS) equations is a finite volume method based on central differences in space co-ordinates and an explicit Runge-Kutta method for the integration in time [44]. The method starts from an initial field which is marched in time until a stationary condition is reached. At this stationary condition is the conservation equations for mass and momentum satisfied. The time step is calculated locally in each control volume to increase the rate of convergence. The k-epsilon model was applied for the generation of turbulence.

The flow solver facilitates multi-block grids with a general and flexible specification of boundary conditions. The cell centred finite volume discretisation stems from the integral form of the Navier-Stokes equations which describes conservation of mass and momentum when viscous forces are neglected.

5.2.1 Geometrical modelling and surface mesh of the ship hulls

The hulls are modelled with a surface mesh which has a finer resolution in the bow part and aft part than midship. Around the hull a volume grid of

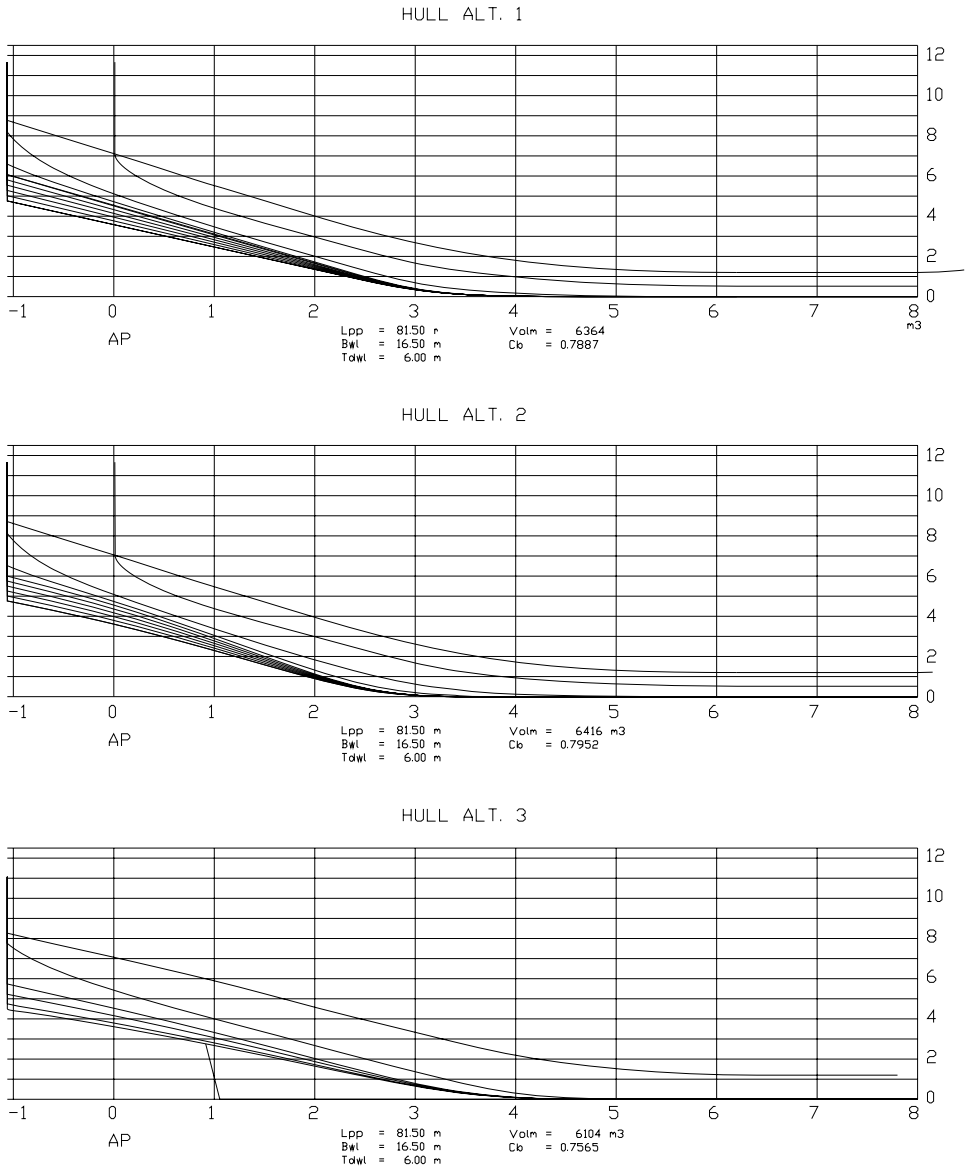

Figure 5.1: *Buttocks of hull alt. 1 (top), 2 and 3 seen from starbord side.*

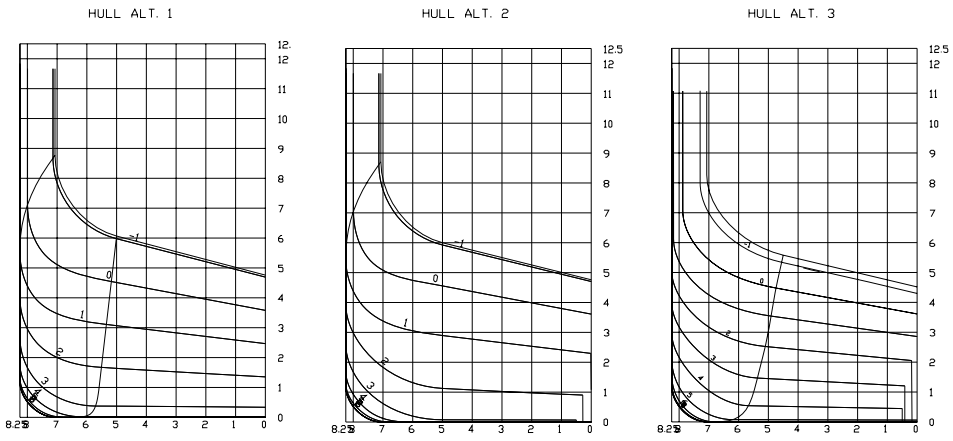

Figure 5.2: *Body plan of hull alt. 1, 2 and 3 seen from aft.*

2 million control-volumes are stretched such that the velocity gradients are resolved sufficiently.

5.2.2 Discussion of results

The above mentioned method was used to calculate the flow field around the ship hulls. Two Azipull thrusters are mounted for propulsion. The Reynolds number based on ship lenght at a ship velocity of 12.5 kn is about $5 * 10^8$.

The calculations are done without propulsion on the thrusters.

Further it was done calculations with free surface which includes wave resistance at velocities 10.5, 11.5, 12.5 and 13.5 kn. These calculations were non-viscous.

Fig. 5.3 shows a calculation of the distribution of pressure coefficient and wall friction lines under the aft part of the three different hulls. We clearly see that hull alt. 2 has a much sharper bottom shoulder from the dark blue color, which means large flow velocities. Hull alt. 3 has the smoothest bottom shoulder, and lower flow velocities over the shoulder which gives less pressure forces trying to trim the vessel. We also see that hull alt. 3 has larger flow velocities in the aft departure. This is supposed to give a lifting effect of the aftbody of the vessel, and also reducing the waves generated by the aftbody

of the vessel. In [8] Yamano shows how the design of the stern form effects the generated waves, and thereby the wave resistance. He concludes that this kind of S-shaped aft run have superior hydrodynamic performances in energy savings, maximum speed and following waves compared with a conventional stern form.

In fig. 5.1 we see that hull alt. 1 has the largest buttock angle close to transom, ca 12.5° with horizontal at the centerline, alt. 2 has ca 10° and alt. 3 has only ca 7.5°. Figs. 5.5, 5.6 and 5.7 shows the wave pattern from the three hulls at three different vessel speeds. We see that hull alt. 3 has significantly lower stern waves than alt. 1 and 2. Alt. 2 also has lower stern waves than alt. 1. Clearly this is due to the buttock angle in the stern, and the "S"-form of the bottom of the aftbody.

From the calculated pressure distribution and wall friction lines in fig. 5.3 we see that the flow is more or less parallell for hull alt. 1 and 3. For hull alt. 2, the flow is more 3D, especially between the pods where the flow is converging towards a separation line. This is due to that hull alt. 2 has the largest stern slope, exceeding what would be recommended for this kind of vessel due to unfavourable 3D flow effects.

Table 5.1 shows calculated viscous pressure resistance coefficient and frictional resistance coefficient. It is interesting to see that both hull alt 2 and 3 have lower viscous pressure resistance than hull alt. 1. The difference in frictional resistance is only marginal. Due to the fact that our design objective was to reduce the frictional resistance and at the same time have a fuller aftbody, we have succeeded. The viscous pressure resistance is significantly lower for the two "optimized" hull, alt. 2 and 3, while the frictional resistance is only marginal lower.

Hull	$C_{Vp} * 10^3$ [-]	Rel. alt.1 in %	$C_F * 10^3$ [-]	Rel. alt.1 in %
Alt. 1	0.57	-	1.50	-
Alt. 2	0.53	-7.0	1.49	-0.7
Alt. 3	0.49	-14.0	1.49	-0.7

Table 5.1: *Calculated viscous pressure- and frictional resistance coefficients.*

Table 5.2 shows calculated wave resistance coefficient for the three hulls at vessel speeds 12.5, 11.5 and 10.5 kn, as well as the total resistance coefficient.

This is calculated by summing the non-viscous wave resistance with the viscous pressure resistance and frictional resistance calculated with the viscous CFD routine. Hull forms 2 and 3 show here a significantly lower wave making resistance. The total resistance is 7.1 % lower for hull alt. 3 than alt. 1 at 12.5 kn.

Hull	V_s	$C_W 10^3$	Rel. alt.1	$C_T 10^3$	Rel. alt.1
	[kn]	[-]	in %	[-]	in %
Alt.1	12.5	1.03	-	2.67	-
Alt.2	12.5	0.892	-13.4	2.55	-4.5
Alt.3	12.5	0.844	-18.1	2.48	-7.1
Alt.1	11.5	0.968	-	2.60	-
Alt.2	11.5	0.869	-10.2	2.52	-3.1
Alt.3	11.5	0.869	-10.2	2.51	-3.5
Alt.1	10.5	0.894	-	2.53	-
Alt.2	10.5	0.855	-4.4	2.51	-0.8

Table 5.2: *Calculated wave resistance and total resistance coefficients for the three hulls forms at different vessel speeds.*

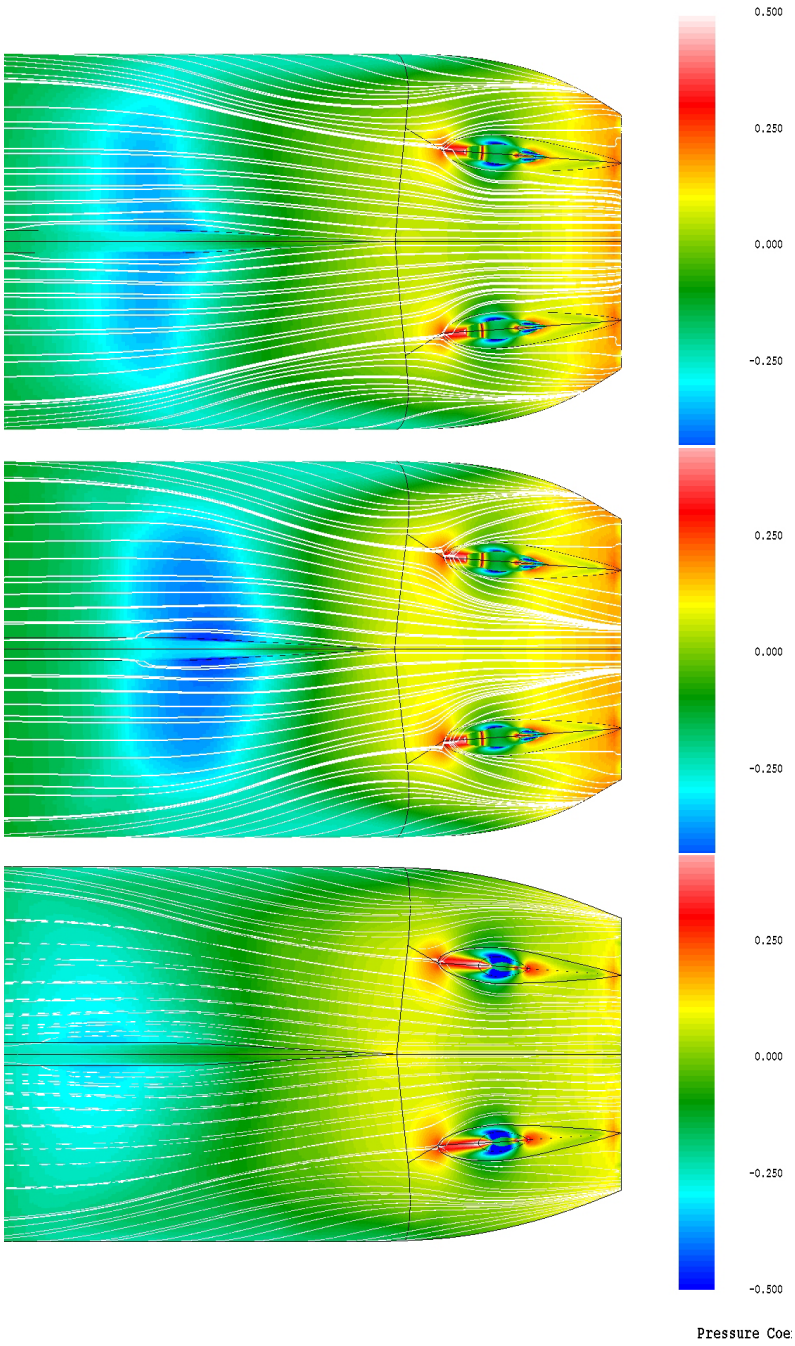

Figure 5.3: *Distribution of pressure coefficient and wall friction lines on ship surface for hull alt. 1 (top), 2 and 3. Without thrust.*

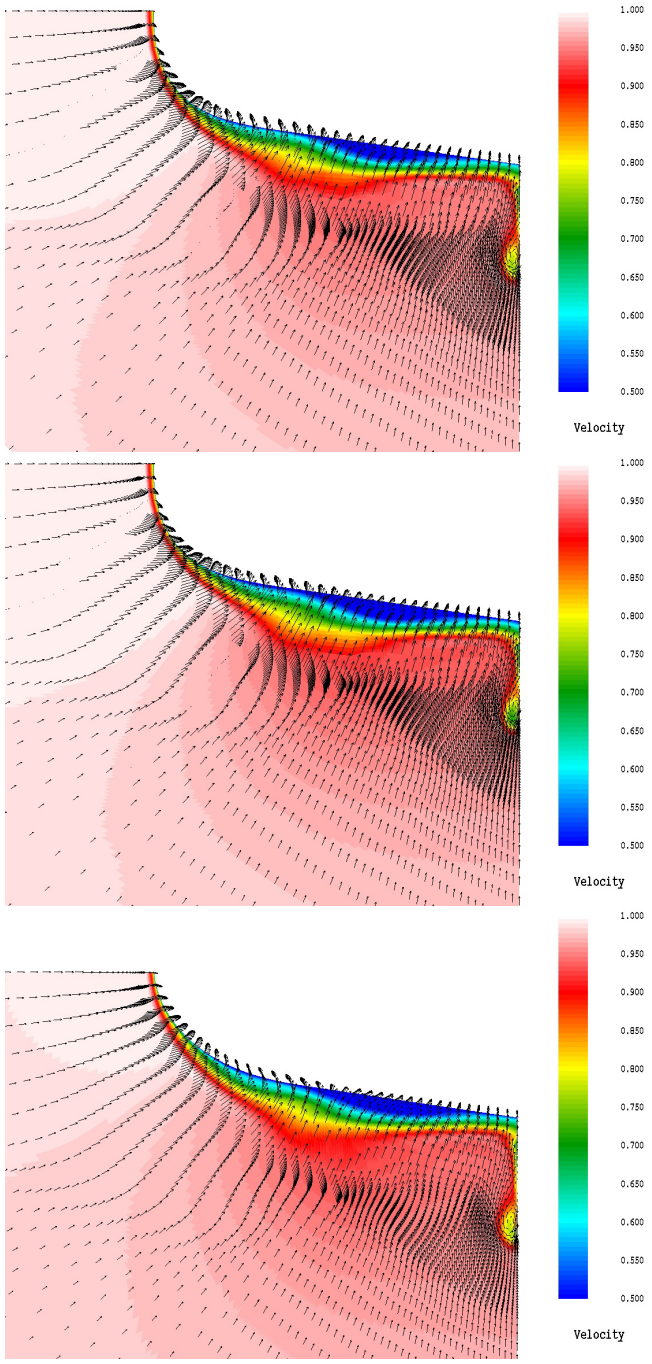

Figure 5.4: *Distribution of axial velocity (colours) and transverse velocity vectors in a cut 3.3 m upstream of AP. Hull alt. 1 (top), 2 and 3. Without thrust.*

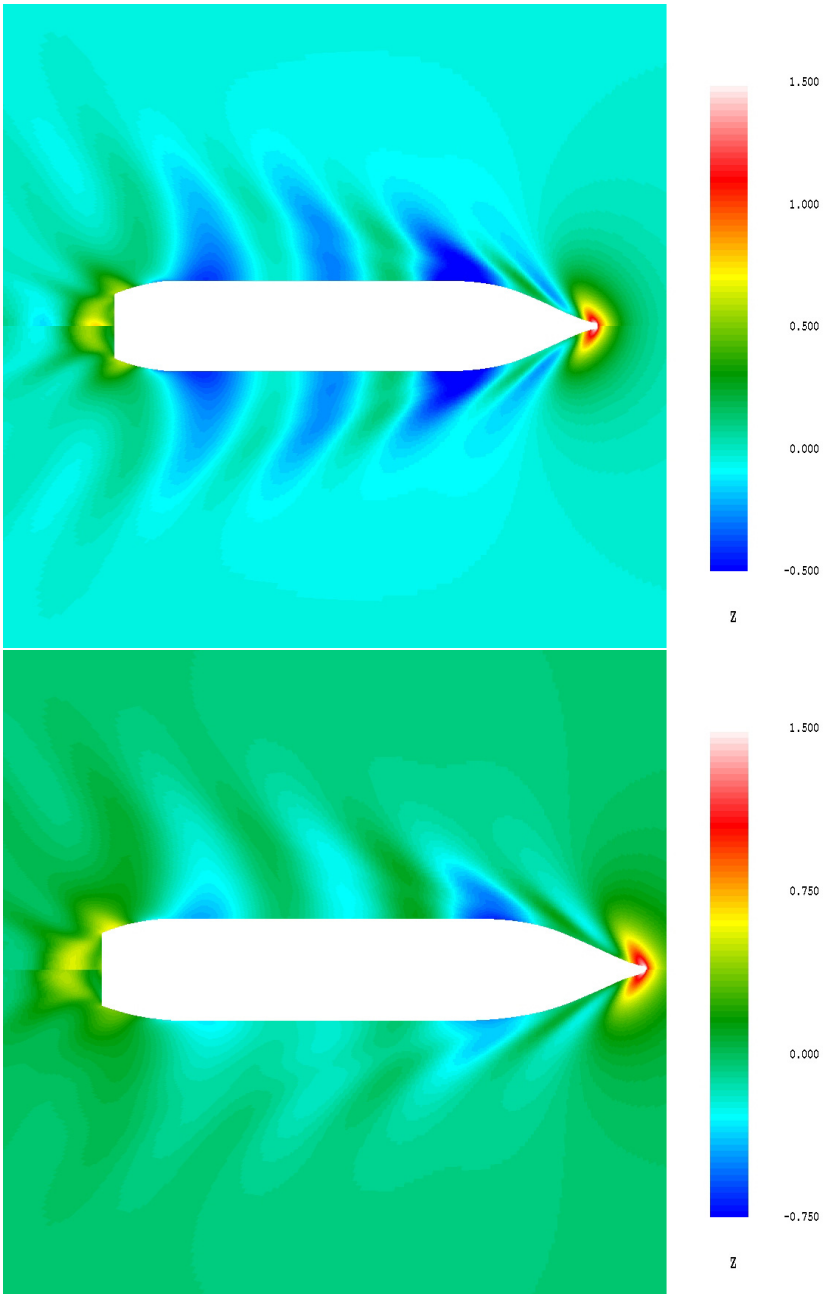

Figure 5.5: *Wave pattern at 11.5 kn. Figure on top shows hull alt. 1 over centerline and hull alt. 2 below centerline. Bottom figure shows hull alt. 2 over centerline and hull alt. 3 below centerline. Note different scaling on the two figures!*

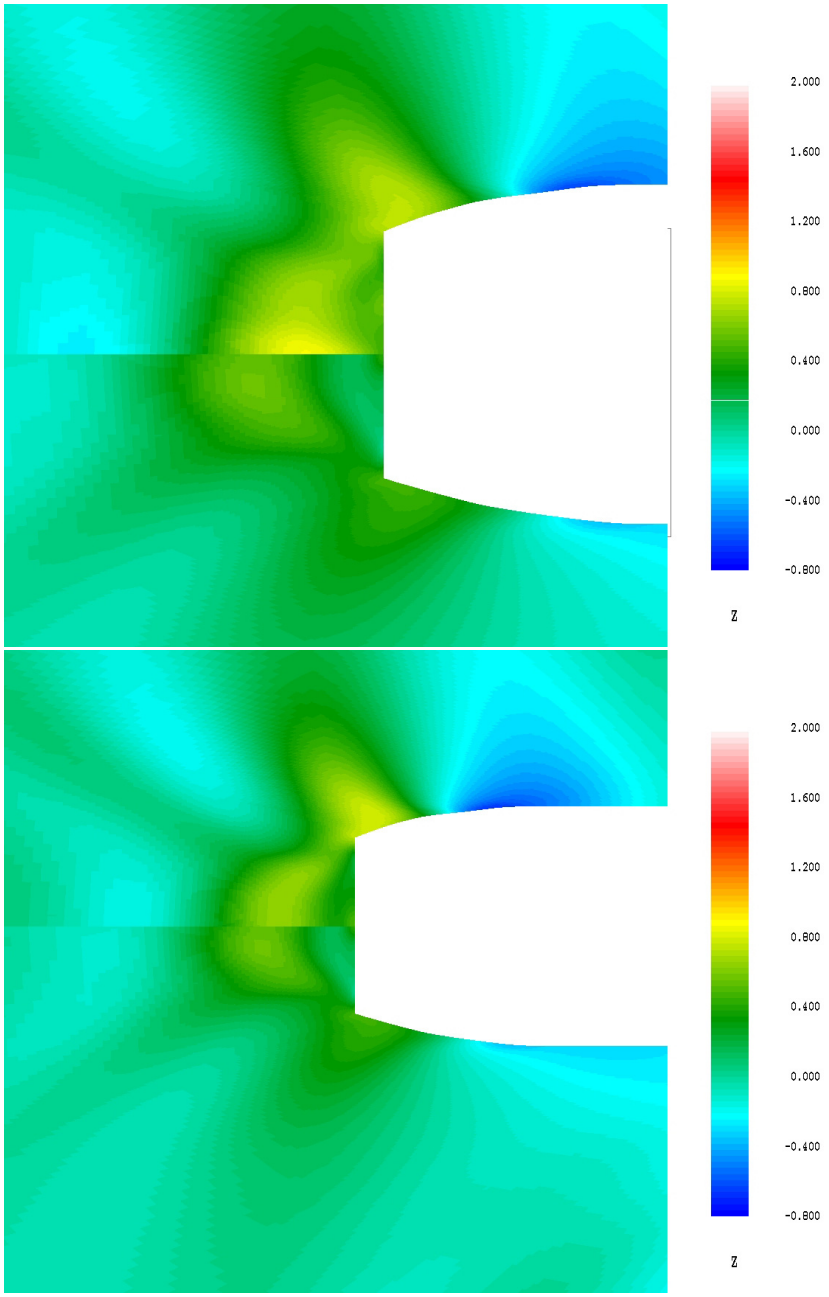

Figure 5.6: *Wave pattern at 12.5 kn. Figure on top shows hull alt. 1 over centerline and hull alt. 3 below centerline. Bottom figure shows hull alt. 2 over centerline and hull alt. 3 below centerline.*

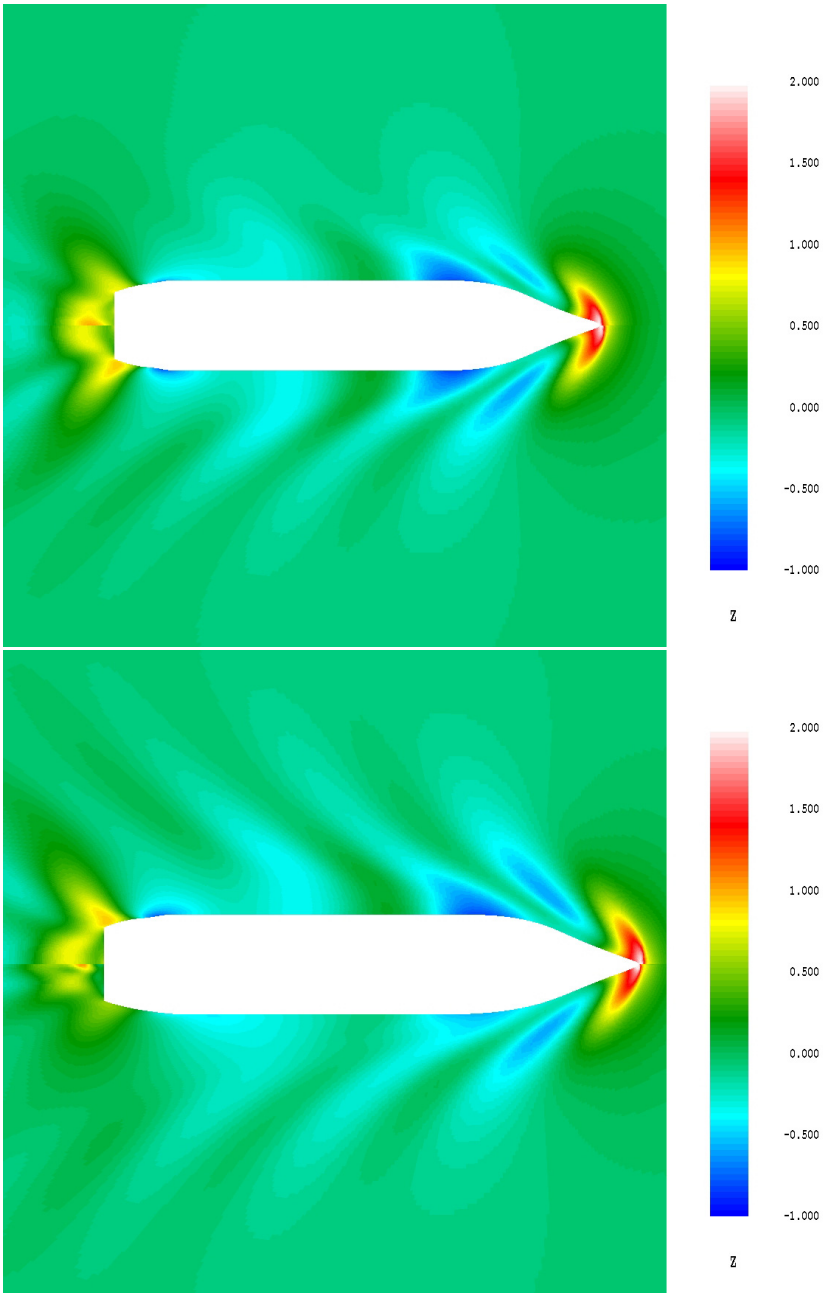

Figure 5.7: *Wave pattern at 13.5 kn. Figure on top shows hull alt. 1 over centerline and hull alt. 2 below centerline. Bottom figure shows hull alt. 2 over centerline and hull alt. 3 below centerline.*

5.3 Towing tank tests

Due to the encouraging results from the CFD calculations it was decided to proceed with towing tank tests with hull alt. 3. This hull has the characteristic S-shaped aft run like alt. 2, but has a longer run from aft shoulder to transom stern. Hull alt. 2 showed the best hydrodynamic performance with respect to viscous resistance and wave making resistance of the three. It must of course be mentioned that the bow part of the three vessels are a little different from each other, but we believe that the trend clearly shows that hull alt. 3 would be a reasonable choice. The towing tank tests were performed at the towing tank facilities at Marintek in Trondheim.

From the resistance plot, fig. 5.8 we see that the Hollenbach empirical formula [13], is in very good agreement with the towing tank tests. It is also a relief to see that the towing tank results gives a little lower resistance than the Hollenbach predictions. This indicates that the our hull lines are better than most other ships with the same main dimensions. The CFD calculations underestimates the resistance, especially for larger velocities.

In fig. 5.8 the resistance is calculated with Waveres, which is an in-house software at Marintek. This is a linear potential flow panel method program with a non-linear correction in the bow region. Waveres slightly overestimates the resistance when compared to towing tank results, and it underestimates sinkage and trim, see fig. 5.9.

Fig. 5.10 shows pictures of the wave formation at the bow part and aft part of the model. As from hull Mod B in the former chapter, we see that the aft hull wave formation is quite small. It is evident that we gain a wave damping effect from the aft hull due to the S-shaped form. The Froude number here is 0.24.

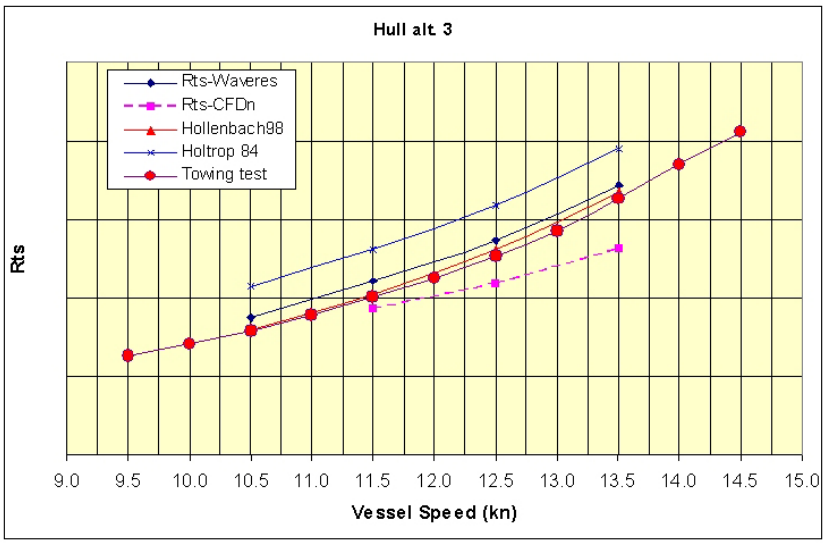

Figure 5.8: *Towing test results togeher with calculations for hull alt. 3.*

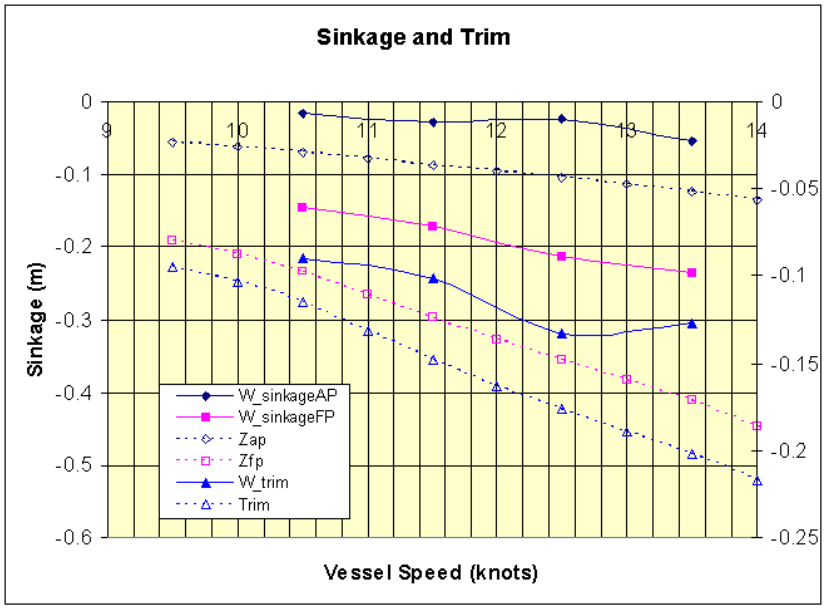

Figure 5.9: *Towing test results togeher with calculations for hull alt. 3. Sinkage and trim. "W" means Waveres calculations, and the other legends are towing tank results.*

Figure 5.10: *Picture of hull alt. 3 from towing test. Fn=0.24.*

Chapter 6

Discussions and recommendations for further work

6.1 The ship hulls designed

In section 3.4 we used the inverse geometry design procedure to find two 2D profiles which are basis for the 3D ship hulls in section 3.5. The two profiles had different lengths of the run from aft shoulder to transom stern. When optimzing the 2D profiles, we changed the parameters β (or Reynolds number), see fig. 2.3, the parameter m in eq. (3.15), start of shoulder and exit angle of keel line at the stern. Fig. 3.9 shows a sketch of the parameters to vary. Mod A and Mod B was designed with the model scale Reynolds number $(4 * 10^6)$. The parameter β was set to 0.66, which means an ordinary Stratford flow, non-conservative for the model scale. The flow will be conservative at full scale, see again fig. 2.3 since the Stratford flow has larger margin before separation at higher Reynolds numbers.

The profiles for hull alt. 2 and alt. 3 in chapter 5 were designed at full scale Reynolds number $(4.6 * 10^8)$, and with $\beta = 0.7$. We then changed the parameters m and the position of start of aft shoulder to achieve a converged optimized profile. The exit angle at the transom was set to 14.5° for alt. 2 and 12° for alt. 3. The parameter m decides the curvature over the aft shoulder.

A small value of m (typically 1.2) gives a large curvature and a large peak velocity U_0 over the aft shoulder. A large value of m (typically 1.4-1.5) gives

a smoother curvature, and a smaller peak velocity. A larger value of m also give acceptence of a larger value of β, due to the smooting of the aft shoulder. At last, we changed the posistion of the aft shoulder to fine-tune the profile to achieve a perfect fit at both ends for the optimization length. The length of optimization was from just forward of the shoulder and aft to 95% of the total length of the profile. We could use the whole length of the profile, but that gave an inappropriate large use of calculation capacity. It was also an advantage to input the exit angle at the transom stern to the optimization process.

We should notice here, that by smoothing the aft shoulder, we could increase β. Increasing β means we are making a more radical Stratford flow, but at the same time smooting out the shoulder decreases the trigging of the separation over the shoulder, which implies that it is acceptable to increase β.

The length of the run from the aft shoulder to the transom stern should not be too short, that means the angle of the slanted surface has a maximum. A large angle can form longitudinal vortices because of the accelerated flow velocities over the aft shoulder and separation of the flow. The larger the slanted angle, the higher the flow velocities will be, see figs. 6.1, 6.2 and 6.3. Extensive wind tunnel testing on cars with fastback, see [1], [2], [3], [14] and [26] shows that for slant angles less than 10° the flow over the aft run is nice and smooth. For slant angles between 10° and 15°, longitudinal vortices are starting to form, and at a slant angle of 25°, these two longitudinal vortices are strong, and gives a strong downwash behind the car. Fig. 6.3 shows an illustration from wind tunnel tests of the surface flow on a car with two different slant angles. These results can not necessairily be used for our ship hull form design, but they give an indication of the limiting slant angles for the aft part of a streamlined body to avoid separation over the side edge. To the authors knowledge there has not been done a study of this aspect on pram-type ships.

For the models in section 3.5.2, Mod A and Mod B, we ended up with a slant angle of approximately 10°, see fig. 3.16 for Mod A, and about $11 - 12^\circ$ for Mod B, see fig. 3.18. This should be inside the recommended slant angles. The tuft tests, see fig. 4.12 did not show any sign of longitudinal vortices forming. The transverse pressure measurements, figs. 4.8 and 4.10 shows that the flow accelerates close to the side edge for the first two sections after the shoulder, thereafter the flow decelerates. This effect is slightly more pronounced on Mod B than Mod A, which is to be expected since this model has a larger slant angle.

As we have seen from the results in chapter 5, a pram-type ship with the

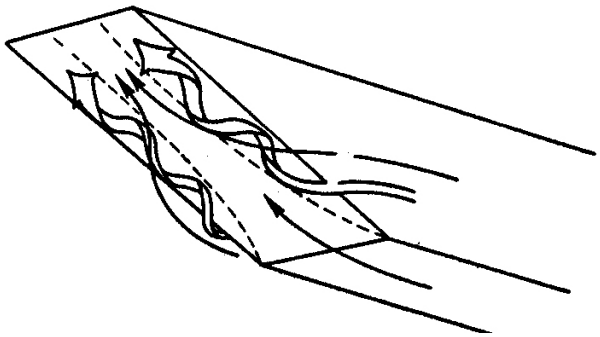

Figure 6.1: *Illustration of three dimensional flow pattern with separation over aft part of hull. From [26].*

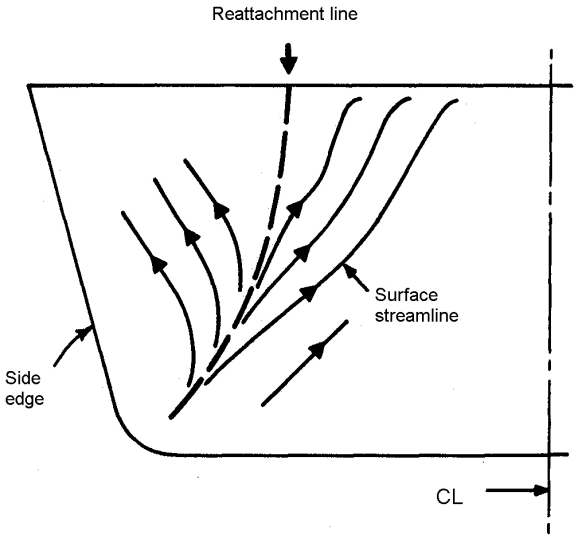

Figure 6.2: *Illustration of surface flow lines over aft part of hull. From [26].*

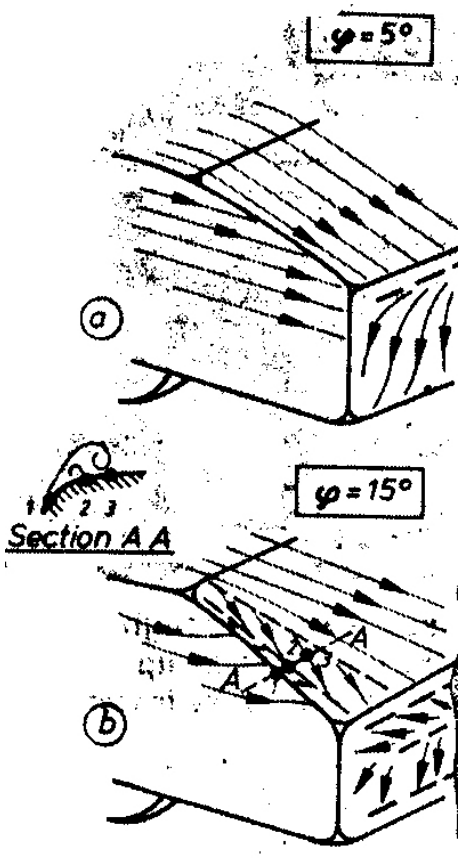

Figure 6.3: *Surface flow over aft part of cars with fastback. The car on top has a slant angle of* 5°*, and the bottom car has* 15° *slant angle. From [2].*

characteristic S-shape seem to have a damping effect on the generated waves from the aft ship. Hämäläinen et al has the same findings in [11].

For a further study it would also be interesting to investigate the wave making resistance with different slant angles of the aft bottom run. It would be quite straightforward to link a wave making calculation code with our optimization routine. We then could calculate hull lines which were optimized with respect to wave making resistance. As a concequence of the findings in chapter 5 it is evident that the potential reduction of wave making resistance is larger than the potential reduction of frictional resistance. On the other hand; the viscous flow point of view is vital for an understanding of the 3D flow over the aft hull.

The hull forms in chapter 5 have V-shaped sections in the aft part. This will of course give a more three dimensional flow picture than a flat shaped pram-type aft ship. For the optimization process we chose the buttock where the transom meets the DWL. That means the buttock which have zero submerged draft at the transom. This buttock were optimized in the 2D optimization process, and the other buttocks for the aft ship were multiplied with a factor to achieve the V-shaped sections. This is of course even less accurate in terms of Stratford flow than for the flat pram-type ship, but still gives the favourable S-shaped buttocks. From fig. 5.3 we see that the streamlines more or less follows the buttocks for hull alt. 3. For alt. 1 and 2, the flow seems to have a slightly more pronounced 3D structure.

From fig. 5.3 we also see the typical flow structure over the ship side edge where a weak longitudinal vortex is forming. This is more pronounced on alt. 1 and 2 which have larger slant angles than alt. 3, respectively 16° and 18° compared to 14° for alt. 3. It seems that the lines layed down by the research on fastback cars are reasonable guide lines for the slanted angle for the aft part of pram-type ship hulls. They recommend not to exceed 15° to achive a relatively smooth flow with no strong longitudinal vortices forming. From our results we see that alt. 1 and alt. 2 have an area with converging streamlines between the pods and the side edges. These converging streamlines could indicate a reattachment line due to a longitudinal vortex forming from the side edge. Alt. 3 seems to have less converging lines in the same area. Fig. 5.4 which shows transverse velocity vectors indicates that a vortex is starting to form for alt. 1 and alt. 2. The cut is 3.3 m upstream of AP. We see that in the vicinity of the bilge, the flow vectors for alt. 1 and alt. 2 are larger than for alt. 3. This makes sense due to the stronger converging lines aft of this cut indicated in fig. 5.3.

Due to these results and results from fastback cars, it would not be advisable to design pram-type ships with slanted angles exceeding 15°.

The method and routine used for the CFD calculations are partly presented in the PhD thesis of I. Øye, see [44]. A. Östman is currently finishing his PhD where he has extended the work of Øye to be applicable to ships. The calculations presented in the former chapter were done with separate viscous flow with the vessel in infinite fluid, and non-viscous flow with free surface. Fig. 5.8 shows the calculated results compared with the towing test results. We see that the CFD calculations give significantly lower results than the towing tests. This is of concern, but the relative difference in resistance between the three ship hulls will probably be more or less correct. The flow picture which is calculated will give a good view of the reality.

6.1.1 Pros and cons of the ship hulls designed

The inverse design method we have examined gives the possibility of designing ships with a larger displacement for the same powering performance.

The block coefficient of Mod B is 0.64, and the parent ship has $C_B = 0.60$, see tab. 3.2. In the book of Watson [39], we can find a relationship between block coefficient and deadweight/displacement ratio, Dwt/Disp. For Mod B we find that Dwt/Disp=0.69, and for the parent ship we get Dwt/Disp=0.64. The deadweight for Mod B is then 5977 tons, and for the parent ship 5182 tons. This means Mod B can carry about 15% more cargo than the parent ship according to this relationship.

The LCB position of our Mod B is 4.9% aft of midship. The designed ships have LCB radically more aft than the "optimum range" presented in [39], which for Mod B would be 1-2.5% aft of midship. He writes that the lines of a twin-screw ship almost entirely can be designed with respect to minimizing resistance of bare hull, and not so much on flow to propeller like for single-screw ships. Since our inverse design method first of all is for twin-screw ships, and we have optimized with respect to resistance, we can accept a more aft LCB than recommended. He also writes that the optimum LCB is further aft for twin-screw ships than for single-screw ships. We are therefore confident that our ships will behave well although they are not in the range of optimum LCB position.

The designed hulls in sec. 3.5 provides about 20% shorter exposed propeller shafts for Mod A, and 30% shorter exposed propeller shafts for Mod B than for the parent ship. By exposed propeller shafts we mean the part of the shaft

which is exposed to the flow underneath the hull. This flow crosses the shaft, and gives appendage resistance. By shortening the flow exposed length of the shaft, we decrease appendage resistance.

The designed aft hull can give a flow to the propell which is relatively smaller than the speed of the ship, see figs 4.31, 4.32, 4.33 and 5.4. When comparing the top and bottom plot in fig. 5.4 we see that the axial velocity for alt. 3 is a little lower than the axial velocity for alt. 1 which is the original ship. Unfortunately we do not have any calculated value of the wake fraction. A lower wake velocity means a higher propeller wake fraction. The increase in the wake fraction gives higher propeller loading which again gives lower propeller efficiency. On the other hand, this decrease of propeller efficiency is compensated for by a higher hull efficiency due to the higher wake fraction. All in all it means the propulsive efficiency is more or less unchanged.

This kind of pram-type ships are exposed to slamming in certain conditions. A series of cruise ferries were built with a flat pram-type aft body. These vessels experienced very uncomfortable slamming induced motions and vibrations in following seas in relatively small seastates. These motions and vibrations mostly occured for zero speed and ship speed below the phase speed of the following waves. The waves would then catch up with the ship, and slam under the flat part of the aft hull. Wedges were built on the flat part, and the result was that aft slamming was more or less eliminated. Our ship designs are first of all meant for trade ships, or Ro-Pax which do not anchor like a cruise ship in unsheltered waters. The normal operating profile of these ships are a given forward speed in a given seastate. The waves will then seldom catch up with the ship, and slamming will not occure in the aft part.

The flat aft part of the ship gives us no longitudinal area at the transom, see figs. 3.20 and 3.21. These ships will be nonlifting bodies with a pointed tail, see [24], and the vessels will allways be directional unstable without a proper skeg. Ships with a deadrise at the aft part of the hull, or cruiser stern ships have a longitudinal area at the transom. This longitudinal area helps increasing the directional stability of the ship, as in the case of an arrow or a wind vane. Our designed pram-type ships therefore depend on a well suited skeg to have satisfactory directional stability. For ships with pods, the fin at which the pod is fitted to, will increase the directional stability. This also applies to a vessel with two rudders (twin screw) or one centerline rudder (single screw). The directional stability of the ship alt. 3 in chapter 5 was measured in the towing tank. The requirements to the directional stability of the vessel was high due to its operating profile in coastal waters. It was therefore decided to make the fins for the pod a little larger. This gave the

ship a satisfying directional stability. The vessel has been decided to be built.

6.2 Experimental results and testing technique

The numerical results required experimental testing for verification. The main experiments would have to be performed in the towing tank to check out the behaviour of the vessel at sea. In the planning of the experiments it was decided that it also was essential to verify the boundary layer flows and boundary layer characteristics like local friction coefficient etc. We decided to do this in a wind tunnel. To do boundary layer measurements in the towing tank would be unnecessairy difficult, and would probably not give us more information.

It then was decided to build Mod A and Mod B for the wind tunnel tests, and only Mod B for the towing tank tests. We thought that if Mod B behaves well, which has the shortest aft run, then also Mod A would behave well in flat waters.

The models in the wind tunnel had an area blockage ration of 10%. The blockage effect seems rather large, see 4.11. On the other side it would be difficult to get good results of the boundary layer velocity if we had a smaller model. The measuring pitot tube would be reltively larger compared with the boundary layer thickness. We would also have lower Reynolds number of the flow. All in all our wind tunnel model size seems to be a reasonable choice. As we see from fig. 4.26 the error due to blockage effect on the local friction coefficient is rather small, from 1.2 to 1.9%.

An interesting results from the wind tunnel tests are the calculations of $\frac{\partial u}{\partial y}$ for different streamlines, refer to eq. (2.30). This is in fact Bernoullis equation for a streamline rewritten. If this term is equal along a streamline for all streamlines in the outer sub-layer of the boundary layer, we might have a Stratford flow. This is a requirement to achieve Stratford flow. We also have to fulfill the requirements for the inner sub-layer as well, see sect. 2.2.2. With our measuring equipment we were not able to measure the boundary layer velocity in the inner sub-layer, we therefore do not have information about those quantities. In figs. 4.19, 4.20 and 4.21 the quatity $\frac{\partial u}{\partial y}$ is plotted. It is very interesting to see the trend of these results when comparing the two models and the two different Reynolds numbers for Mod B. Mod B at $Rn = 4 * 10^6$ is closest to Stratford flow, and also has the most horisontal $\frac{\partial u}{\partial y}$ for each streamline compared to Mod A, and Mod B at $Rn = 6 * 10^6$.

It was decided to do towing tests with the model free to trim, and locked in trim. This was done to investigate if there were any differences in the static pressures on the hull surface for the two modes, because the aft hull is designed with the design water line as the flat water surface. The vessel at speed will trim, and it would be interesting to see to what extent the trim influenced the static pressure. The conclusion was that there were practically no difference in the two modes, see figs 4.41 and 4.42.

It was embarrassing not to use static pitot tube for the static pressure measurements on the ship hull. This could have given us more iformation about the absolute flow velocities over the hull surface in infinite fluid, instead of only static pressures relative to pressure port # 130.

The wave making around the hull gave an effect on the static pressures, see figs 4.41 and 4.42. For Froude numbers around 0.28 we had the largest aft body generated waves. For larger and lower Froude numbers, the generated waves decreased, and so did the influence on the static pressure measurements.

We did not perform seagoing towing tests for neither the Mod B in chapt. 4 nor the models in chapt. 5. Due to the flat underwater bottom in the aft hull, it would be interesting to see the performance of the vessels in realistic seastates. Especially will the aft hull be exposed to wet deck slamming in following seas. This has showed to be a major problem on cruise boats which have this kind of aft hull. On the other hand, a Ro-Ro vessel will allways be heading forward, and not anchor like a cruise ship.

There were done directional stability tests on hull alt. 3 in chapt. 5. The results in the first round of tests were a little discouraging. The vessel had a little less directional stability than wanted. The problem was solved by adding lateral area in the aft part in terms of fins and larger headboxes for the azipods.

6.3 Numerical procedures - lessons learned

The inverse method with the surface vorticity model for the direct flow calculation was probably not the best choice of method for direct flow calculation. On second thoughts it would probably have been better to use a source/sink method. The vortex distribution method was though available and easier to program, and due to lack of time it was used. In this method the flow velocity was calculated in the middle of an element. In the optimization process the body profile is changed vertically in the node points, refer to eq. (3.14), to

achieve the desired velocity profile. We then had to interpolate to find the velocity in the node points. This gave rise to error and the typical wavy profiles, see fig. 3.15. If we increased the number of node points, the waviness more or less disappeared, but this of course required a long calculation time.

Another method for direct flow calculation which was tested but rejected was a finite element method. This method calculates the potential flow in a designed subdomain with given boundary conditions. This method gave very good results for direct flow calculations of different 2D bodies. The force of this method is that it calculates the flow velocity directly in the given node points for the profile. This was a big advatage compared to the vortex method. The disadvantage with the finite element method linked to the inverse geometry optimization code was that it did not converge when the number of body elements exceeded a certain limit. We did not succeed in finding the reason for this, and therefore the method was not used.

The optimization routine which is a part of Matlab, showed to be very effective and powerful. During the work on the thesis this routine was used in different applications with great success and save of time. For instance was it used for zero-finding purposes in implicitly defined equations. It was also used to find parameters in a formula describing the bilge radius of the hulls.

The optimization routine could have been extended to yield 3D ship hull optimization without too much difficulties. In that case we could calculate the 3D potential flow over the ship hull. The flow along the centerline of the ship is input to the inverse routine where the actual velocity is compared with the desired velocity given by the Stratford equation. A new keelline is then found. This process is the same as for the 2D optimization. When the new keelline is found, a new pram-type ship hull is easily found with a given bilge radius. This bilge radius will be a function of the longitudinal position aftwards. This 3D flow calculation could have been done with a Hess & Smith method, but this was unfortunately not available.

The finite element routine mentioned is found in Femlab which is a toolbox in Matlab. This software is now extended to 3D, and this was tested by the author. The software is promising, but unfortuneately there were difficulties due to the very small surfaces on the hull surface which was necessary to have an acceptable resolution of the hull. These small surfaces had in comparison very large neighbouring sufaces; the vertical mirror plane in the centerline, and the horisontal mirror plane which was the free surface. The software gave an error when the area ratio between two neighbouring surfaces were larger than a certain limit. This is obviuosly a weak point, and will hopefully be

corrected in later versions.

Chapter 7

Conclusions

The main contribution of this thesis is on the study of optimization methods in aft hull design. The optimization methods are inverse geometry design methods to find an aft hull with the flow velocities we specify. The analytic foundation for the flow is given by Stratford in [31], and gives a prescribed velocity distribution on the aft body. With the parameter β we have adjusted this flow to have a certain margin to separation all along the pressure recovery region.

The main results presented in this thesis are shortly presented below.

- Inverse geometry optimization methods with prescribed velocity distribution are successfully applied to design of ships with pram-type aft hull.

- We have shown that Stratfords original pressure distribution for pressure recovery region for Reynolds numbers up to 10^7 can be used for ship full scale Reynolds numbers ut to 10^9.

- There is a potential of reducing the total resistance of pram-type ships with up to 7% compared to conventional design. The frictional resistance is about half of the total resistance, and we found it could be reduced by about 1%. The viscous resistance is about 15% of the total resistance, and can be reduced by up to 14%. Finally the wave making resistance can be reduced with as much as 15-18% with the presented type of aft hull, and this resistance component is typically 35% of the total resistance.

- We can increase cargo capacity with the same power consumption compared to conventional aft hull. We can also achieve a more favourable distribution of the displacement in the aft hull.
- For conventional twin-screw the length of the propeller shafts exposed to the flow will be shorter. This is an advantage with respect to appendix resistance for the ship. The propeller shafts will also be shorter, which affects weight and cost.
- The designed aft hull can give a flow to the propell which is relatively smaller than the speed of the ship. This means a higher propeller wake fraction. The increase in the wake fraction gives higher propeller loading which again gives lower propeller efficiency. On the other hand, this decrease of propeller efficiency is compensated for by a higher hull efficiency due to the higher wake fraction. All in all it means the propulsive efficiency is more or less unchanged.
- The designed aft hull is a well suited platform for podded driven propulsion (POD). The hull has a long, relatively flat aft part which gives the POD good space for rotation in all directions.
- The measured local skin friction coefficient for the windtunnel models corresponded very well to the calculated skin friction for the 2D optimized profiles. This shows that the flow over the ship hull surface from midship and aft along centerline has a 2D structure. This is another result which supports the fact that the flat plate friction line is suitable for predicting the frictional resistance of slender ships. This result also supports our design procedure where we extend a 2D centerline buttock transversally to form a 3D hull.
- When optimizing our ship hulls we had to define a certain margin for separation to avoid too large slant angles. Slant angles should not exceed 15° due to danger of separation over the bilge, and longitudinal vortices forming.
- At low speeds and relatively small following waves we can get slamming in the aft part of the hull. Slamming induced vibrations and motions decrease with increasing speed, and will normally disappear when the ship velocity is higher than the velocity of the following waves.
- Pram-type hulls are flat or with a small deadrise at the aft part of the hull. This can give rise to insufficient directional stability, and these hulls therefore need a well suited skeg.

Bibliography

[1] S.R. Ahmed. The structure of wake flow behind road vehicles. In *Aerodynamics of transportation, ASME*, 1979.

[2] S.R. Ahmed. Influence of base slant on the wake structure and drag of road vehicles. *J. Fluids Engineering*, 105, 1983.

[3] P.W. Bearman. Some observations on road vehicle wakes. *SAE pap. 840301*, 1984.

[4] D.R. Bristow. A solution to the inverse problem for incompressible axisymmetric potential flow. In *AIAA 7th fluid and plasma conference*, 1974.

[5] Cheng-Hung Huang et al. An inverse geometry design problem in optimizinghull surfaces. *Journ of ship research*, 42(2):79–85, 1998.

[6] T. Coleman et al. *Optimization toolbox for use with Matlab.* The MathWorks inc.

[7] T. Nagamatsu et al. Study on the minimization of ship viscous resistance. *Naval architect and ocean engineering*, 22, 1984.

[8] T. Yamano et al. Development of a new stern form for ocean going fine ships. *J. Kansai Soc. N. A. Japan*, 1994.

[9] P.S. Granville. The viscous resistance of surface vessels and the skin friction of flat plates. *SNAME*, 64:209–240, 1956.

[10] Mo-Qin He, Hong-Cui Shen, and Shu-Long He. Uncertainty analysis of towing test. In *Practical design of ships and other floating structures*, 2001.

[11] R. Hämäläinen and J. van Heerd. Hydrodynamic development for a large fast monohull passenger ferry. *SNAME Transactions*, 106, 1998.

[12] S.F. Hoerner. *Fluid-dynamic drag.* Published by the author, 1965.

[13] K.U. Hollenbach. Beitrag zur abschützung von widerstand und propulsion von ein- und zweischraubenschiffen im vorentwurf. Institut für Schiffbau der Universität Hamburg, Bericht Nr. 588., 1997.

[14] W.H. Hucho. Aerodynamics of road vehicles. *Annu. Rev. Fluid Mechanics*, 25, 1993.

[15] G. Hughes. Frictional resistance of smooth flat plane surfaces in turbulent flow. *Trans. RINA 94*, 1952.

[16] G. Hughes. Friction and form resistance in turbulent flow, and a proposed formulation for use in model and ship correlation. *Trans. RINA 96*, 1954.

[17] ITTC. Ittc quality manual standard procedure 7.5-02-02-02 rev. 01. 23rd ITTC specialist commitee: Procedures for resistance, propulsion and propeller open water tests.

[18] P.Å. Krogstad, R.A. Antonia, and L.W.B. Browne. Comparison between rough and smooth wall boundary layers. *J. Fluid Mech.*, 245, 1992.

[19] R.I. Lewis. *Vortex element methods for fluid dynamic analysis of engineering systems.* Cambridge University Press, 1991.

[20] R.I. Lewis. An iverse method for the design of bodies of revolution by boundary integral modelling. In *Proc. Instn Mech Engrs, Vol 205*, 1991.

[21] R.H. Liebeck. Design of subsonic airfoils for high lift. *J. Aircraft*, 15(9), 1978.

[22] N. Matheson and P.N. Joubert. Experimental determination of the components of resistance of a small 0.80 c_b tanker model. *Jounal of ship research*, 17(3):163–180, 1973.

[23] N. Matheson and P.N. Joubert. A note on the resistance of bodies of revolution and ship forms. *Jounal of ship research*, 18(3):153–168, 1974.

[24] J.N. Newton. *Marine hydrodynamics.* The MIT press.

[25] H. Schlichting. *Boundary-layer theory.* McGraw-Hill, 1979.

[26] R. Sedney. A flow model for the effect of a slanted base on drag. In *Aerodynamics of transportation, ASME*, 1979.

[27] Hong-Cui Shen, Mo-Qin He, and Zhou Yi. Uncertainty analysis of resistance test. *Journal of ship mechanics*, 3(6), 1999.

[28] A.M.O. Smith, T.R. Stokes Jr., and R.S. Lee. Optimum tail shapes for bodies of revolution. *J. Hydronautics*, 15(1), 1981.

[29] L.R. Sætran. *Experimental investigation and mathematical modelling of momentum, mass and heat transfer in some turbulent flows.* PhD thesis, Norwegian Insitute of Technology, 1984.

[30] B.S. Stratford. An experimental flow with zero pressure friction throughout its region of pressure rise. *J. Fluid Mechanics*, 5(1), 1959.

[31] B.S. Stratford. The prediction of the separtion of the turbulent boundary layer. *J. Fluid Mechanics*, 5(1), 1959.

[32] Y. Tahara, J. Ando, and Y. Himeno. Cfd-based optimization of tanker stern form - minimazation of delivered horsepower using self-propulsion similator. Practical design of ships and floating structures, 2001.

[33] I. Tanaka. Scale effects on wake distribution and viscous pressure resistance. *Naval architect and ocean engineering, SNA Japan*, 17, 1979.

[34] R.L. Townsin and A. Mosaad. The ittc line - its genesis and correlation allowance. *The Naval Architect*, 1985.

[35] R. van den Braembussche. The application of singularity methods to blade to blade calculations. Nato advanced study institute on thermodynamics and fluid mechanics of turbomachinery.

[36] R. van den Braembussche, O. Leonard, and L. Nekmouche. Subsonic and transonic blade design by means of analysis codes. In *AGARD Proc. No. 463.*

[37] E.R. van Driest. On turbulent flow near a wall. *Journ. of the Aeronautical Sciences*, 23, 1956.

[38] A. Walz. *Boundary layers of flow and temperature.* MIT press, 1969.

[39] D.G.M. Watson. *Practical ship design.* Elsevier.

[40] F.M. White. *Viscous fluid flow.* McGraw-Hill, 1991.

[41] K. Wieghardt. Analyse eines grenzschichtprofils. *Jahrb. STG*, 62, 1968.

[42] K. Wieghardt. Subject resistance; power formula for plate flow at high rn. *14. ITTC conf.*, 1975.

[43] K.G. Winter. An outline of the techniques available for the measurement of skin friction in turbulent boundary layers. *Prog. Aerospace Sci.*, 18, 1977.

[44] I.J. Øye. *On the Aerothermodynamic effects on Space Vehicles.* PhD thesis, NTNU, Trondheim, 1996.